Towards Plasma Charging Visualization

Document Version:
Publisher's PDF, also known as Version of Record (includes final page, issue and volume numbers)

Please check the document version of this publication:

• A submitted manuscript is the version of the article upon submission and before peer-review. There can be important differences between the submitted version and the official published version of record. People interested in the research are advised to contact the author for the final version of the publication, or visit the DOI to the publisher's website.
• The final author version and the galley proof are versions of the publication after peer review.
• The final published version features the final layout of the paper including the volume, issue and page numbers.

Link to publication

Download date: 07. nov.. 2023

Towards Plasma Charging Visualization

PROEFSCHRIFT

ter verkrijging van de graad van doctor aan de Technische Universiteit Eindhoven, op gezag van de rector magnificus prof.dr. S.K. Lenaerts, voor een commissie aangewezen door het College voor Promoties, in het openbaar te verdedigen op dinsdag 13 juni 2023 om 11:00 uur

door

Mohammad Hasani

geboren te Teheran, Iran

Dit proefschrift is goedgekeurd door de promotoren en de samenstelling van de promotiecommissie is als volgt:

voorzitter: prof.dr. C. Storm

1e promotor: dr.ir. J. Beckers

2e promotor: prof.dr.ir. G.M.W. Kroesen

externe leden: prof.dr.rer.nat. H. Kersten (Christian-Albrechts-Universität, Kiel)

prof.dr. E. Kovačević (GREMI-CNRS, Université d'Orléans)

overige leden: prof.dr. V.Y. Banine

prof.dr.ir. O.J. Luiten

Het onderzoek of ontwerp dat in dit thesis wordt beschreven is uitgevoerd in overeenstemming met de TU/e Gedragscode Wetenschapsbeoefening.

Towards Plasma Charging Visualization

Mohammad Hasani

Contents

Summary

A plasma is an ionized gas that exhibits collective behavior. Dusty or complex plasmas – also coined Complex Ionized Media (CIM) - are generally defined as plasmas containing additional micro- to nanometer-sized dust particles besides their standard components (i.e. electrons, ions, and neutrals). The presence of dust particles in a plasma phenomenally alters the plasma's characteristics; these alterations include a reduction in electron density, an increase in electron temperature, and a reconfiguration of charged constituents. Either formed internally inside the plasma, in the case of a reactive plasma or injected externally into it, dust particles are known to become electrically charged upon interaction with the plasma. Depending on the size of the particles, their position in the plasma, and the temporal evolution of the plasma itself, these dust particles acquire a (sometimes) positive or (often) negative charge. This particle charge is the key parameter dictating the interactions of the particles with the surrounding plasma and the interactions between plasma-immersed particles mutually. Moreover, it also determines particle dynamics in (post-) plasma environments. Until now, the processes regarding particle charging in plasma environments – especially for particles with sizes in the nanometer regime – remain far from understood at an elementary level.

Besides the importance of understanding particle (de-)charging in (post-) plasma environments for scientific fields such as dusty and complex plasma physics, astrophysics, and aerosol science, there is an increased prevalence of the combination of plasma and particles embedded in it in semiconductor or other high-tech industries. Mainly, due to the ever-shrinking length scales (i.e. into the nanometer regime) of features processed in these advanced industries, the demand is placed on investigating the charging of nanometer-sized particles to explore their dynamics in the plasmas used or inherently formed during the relevant processing steps.

The contents of this thesis revolve around the theme of

"charging and decharging processes of negative ions, nanoparticles, and surfaces in low-pressure radiofrequency plasmas and the afterglows thereof".

This thesis aims at developing diagnostic methods to shed light on the unknown charging and de-charging process of nanoparticles. The experimental research conducted and reported in this thesis constitutes three main results chapters. The first results chapter lays the foundation for the visualization of nanoparticle charging to the end of surface charge monitoring, while the second and third results chapters enhance the technique of Laser-Induced Photodetachment (LIP) to investigate the temporal afterglows of electronegative (here oxygen-based) and reactive (argon-acetylene based) plasmas as these plasmas contain negative ions and a combination of negative ions and nanodust particles respectively. In this thesis, the term "temporal afterglow (plasma)" refers to the phase of decaying (in time) plasma after the plasma power source is terminated.

In the first results chapter of this thesis, surface charge-induced changes in photoluminescence properties of quantum dots (QDs) are used for the visualization of charge on a plasma-exposed surface. To this end, nanometer-sized semiconductors exhibiting special optical properties are deposited on a surface and exposed to a low-pressure radiofrequency (RF) argon plasma. The photoluminescence (PL) emission, i.e., light emitted by these so-called quantum dots upon excitation by laser light, is used to detect the residence and quantify the density of excess charges on the surface delivered to it by the plasma. First, the residence of excess electrons on the surface is detected by monitoring the PL emission peak. It has been observed that this peak is subject to a redshift resulting from electric fields associated with excess electrons residing near the surface of the QDs, i.e., a phenomenon called the quantum-confined Stark effect. This redshift has been measured to be 0.05 nm for QDs with a size of 6.1 nm in diameter. The experimentally observed redshift is cross-checked with a surface charge model that correlates the redshift to the electric fields originating from the random configuration of surface electrons. Second, the surface charge density is quantified by measuring the exact value of the redshift of the PL emission peak when increasing the input power of the plasma. The redshift values are measured to be higher for relatively higher input powers which can be explained by a higher surface charge density for higher plasma input power. These results are confirmed by approximating the electric field in the plasma sheath and cross-checking by a discrete charge model.

In the second results chapter of this thesis, the diagnostic combination of laser-induced photodetachment (LIP) operated at 1064 nm and 532 nm, and microwave cavity resonance spectroscopy (MCRS) is further developed and improved to investigate the temporal afterglow of an electronegative plasma. More specifically, these methods are applied to investigate the temporal evolution of the densities of free electrons and negative ions (e.g., O^-, O_2^-, and O_3^-) with microsecond time resolution during the afterglow of a pulsed capacitively coupled RF oxygen plasma. The temporal afterglow evolution of the electron density significantly depends on the gas pressure, with a mode transition observed when the pressure is increased from 3 Pa to 6 Pa. When operating at 3 Pa, the plasma operates in the so-called γ- mode in which the electron density decays rapidly when the power is terminated. Here, the electron density decay is dominated by plasma diffusion and recombination at the plasma containment walls. At a slightly elevated pressure of 6 Pa, the plasma operation transited to the so-called α- mode in which a rampant release of electrons is caused by autodetachment of electrons from mainly O^- negative ions. The densities of oxygen anions were found to decay on longer timescales compared to the decay time scale of the electrons when the plasma is operated in γ- mode. In this case, during the afterglow phase, a positive-ion-negative-ion plasma appears after the rapid decay of electrons and before the decay of negative ions. In the α- mode, however, the emergence of autodetached electrons extends the total decay time of the electrons. This extended residence of electrons in the afterglow leads to obstruction of negative ion fluxes towards the plasma containment walls, a phenomenon characterized as the self-trapping of negative ions in such afterglow plasmas.

In the third results chapter of this thesis, the temporal afterglow of a reactive plasma was investigated by measuring electron and negatively charged species densities temporally resolved using, again, the combination of LIP (operated at 266 nm) and MCRS. Here, a reactive plasma in a mixture of argon and acetylene gas was formed to initiate the particle growth process by polymerization and to grow small clusters of dust particles internally. To ensure that a majority of negatively charged species were to be converted to electrons and neutrals by photodetachment, the laser light wavelength was set at 266 nm. The electron density was observed to decay rapidly (on ms timescales) when the plasma power was cut. This decay was more rapid for longer plasma-on times prior to the afterglow phase. This indicated an increased total particle surface area towards which electrons could freely diffuse and recombine, leading to a significant additional electron depletion. The negatively charged species density was measured to be higher for longer plasma-on times, indicating that more anions and (larger)

dust particles were formed during extended growth times. Upon switching off the plasma, the negatively charged species, comprised of anions and nanometer-sized dust particles, were found to decay on significantly long timescales of a few seconds in the afterglow phase.

In conclusion, the work reported in this thesis advances the field in two manners. First, the diagnostic approaches of **I)** surface charge visualization by QD photoluminescence and **II)** the combination of laser-induced photodetachment and microwave cavity resonance spectroscopy have been advanced in such a way that they can be applied to investigate charging of surfaces and particles on the nanoscale. Second, the application of these diagnostics has significantly extended the elementary knowledge base regarding the governing mechanisms for particle and surface (de-)charging by plasmas and afterglow plasmas. The research reported in this work, therefore, provides valuable insight into the relevant scientific fields and can be used in the high-tech industry to develop various contamination control strategies as well as nanoparticle synthesis applications.

Chapter 1

Introduction

Plasmas are prevalent in multitudinous environments and applications that play increasingly important roles in our daily lives, from the early constellations where our planet earth began to form to photolithography machines that manufacture the most vital product to our modern civilization: processor microchips. Essentially, a plasma is an ionized gas containing charged species, i.e., electrons and positive ions, along with neutral gas atoms or molecules. The collective behaviour associated with plasmas marks the fundamental distinction between this particular state of matter and the gas state. Ironically, the sheer complexity of plasmas has shrouded these sources of light in mystery and darkness. As human species, the unknown drives our curiosity, and it is the substance from which knowledge can emerge. Therefore, we must utilize our diagnostic tools to shed light on the plasma environment and understand the basic physics that accounts for its fundamental phenomena. Derived from the greek word *phainomenon* meaning *that which shines forth*, a phenomenon can be used to illuminate the unknown and **visualize** the elementary processes in plasma. In this dissertation, we use various phenomena as diagnostic methods to probe plasmas. These diagnostic methods aim at investigating the fundamental processes in (dusty) plasmas formed in laboratory conditions. Moreover, the knowledge obtained from these enhanced diagnostic methods can be used to solve problems in commercial plasma applications.

Upon the emergence of plasmas in laboratory and commercial conditions, in some cases, some forms of particulates coexist with other plasma components. These particulates, called dust particles, are relatively large (nanometer to micrometer) compared to ions and electrons and can be positively or negatively charged depending on their surrounding plasma environment. Dust particles, however small, are in mutual interaction with the surrounding plasma, of which

the dynamics may be affected simultaneously; therefore, their dynamics and effects are crucial to investigate if one wants to understand such systems.

1.1 Dusty plasmas

When plasma was first recognized and studied in the early 20th century by Irving Langmuir, the possible presence of micro- to nanometer-sized particles in it was not characterized. With the advent of the microchip industry and the strive to increase the number density of transistors, tiny dust particles in microelectronic etching and processing reactors found their way into the spotlight of plasma physics [1]. Dust particles were found in plasma reactors, and a new plasma type, a so-called dusty plasma, was then defined as a plasma containing charged particulates besides electrons, ions, and neutrals. When plasma is formed in inert gases, where chemistry is suppressed, and dust particles are discovered, the most likely source of particles is from mechanical movements in the plasma reactor (and frictions between physical components). However, in some cases, the plasma itself has the propensity to chemically form dust particles once ignited and sustained long enough in a reactive gas. To study both cases, one has to either inject dust particles externally into a plasma formed in a noble gas (e.g., argon) or internally form dust particles inside a plasma ignited in a reactive gas (e.g., acetylene).

In either situation, it is essential to study the dynamics of the dust particles both when the plasma is operating (i.e. the steady-state phase) or when it is extinguishing (i.e. the afterglow phase). Several parameters play roles in determining particle dynamics, among which the particle charge is the most important. In the situation where the particle source is internal, one must investigate the chemical processes leading to the formation and growth of dust particles in the plasma.

Consider a plasma formed in a gas in which dust particles are injected (see figure 1.1). The constituents of plasma, in this case, are neutrals, positive ions, electrons, metastables, and dust particles. Any macroscopic object surrounded by (low-pressure) plasma gains a negative charge. This includes electrodes for plasma generation, plasma confining reactor walls - and - dust particles embedded in the plasma. As long as the plasma operates, electrostatic sheaths surround the whole plasma volume. These sheaths are space charge barriers and act as electrostatic repulsive barriers for the negatively charged particles - under most conditions - to leave the plasma. Therefore, the dust particles are usually trapped inside the plasma under normal steady-state plasma operation. However, this situation seizes to exist as the plasma is switched off (afterglow phase), and the sheath barriers no longer hold the dust particles in the plasma volume. Another
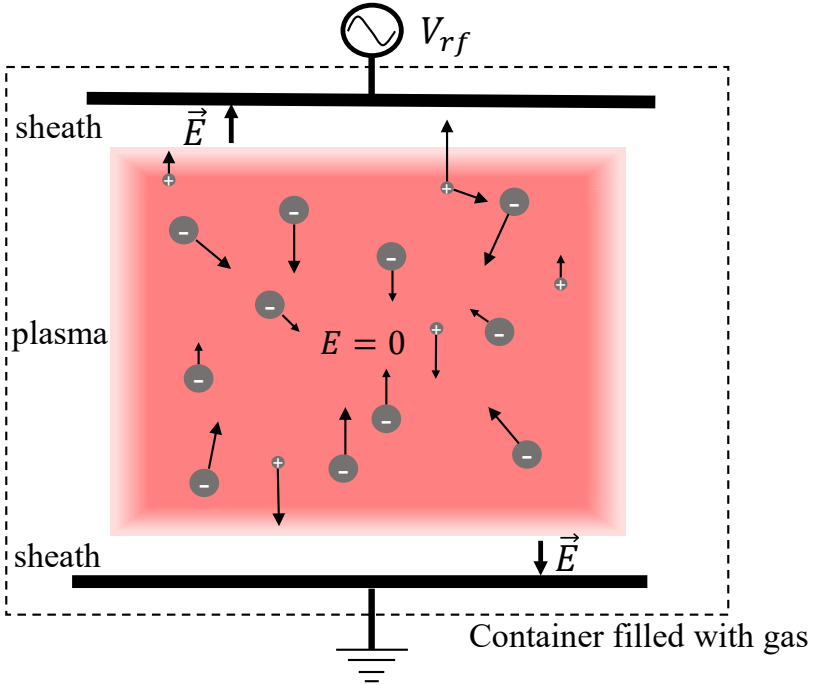
Figure 1.1: Schematic of a dusty plasma: the (relatively) larger particles (grey circles) attain a negative charge from the plasma while the smaller particle may attain a temporary positive charge as well as a negative charge. The negatively charged particles are trapped inside the plasma, whereas the positively charged ones are accelerated toward the plasma-confining walls.

peculiar situation is that the particle may become positively charged due to a significantly smaller size [2]. These small, few nanometer-sized dust particles acquire a charge that fluctuates between the negative and positive, which is opposite to the situation for larger (>20 nm) particles for which the particle charge is negative and permanent. Therefore a population of the small particles may even be accelerated in the sheath region and travel to and land on the surfaces in the reactor.

To understand the trajectory of particles in steady-state or afterglow plasmas, numerous forces on particles must be taken into account. The particle charge is the key parameter for the analysis of the forces on the particles. The particle charge is often determined by a conventional charging theory developed for probes, such as the Orbital Motion Limited (OML) theory which equates the contribution of electrons and positive ion fluxes to determine the eventual charge for a particle immersed in plasma.

However, as the dust particle size becomes smaller the individual contribution of each electron and ion landing on the surface of a dust particle has to be considered due to the discrete nature of the charging process. According to the discrete charge model devised by Cui and Goree [2], the time interval between two subsequent charging events is randomly distributed. This stochastic approach leads to fluctuations of the particle charge ranging from negative to positive charges. Other models factor in, for instance, the contribution of thermionic emission and UV irradiation for small dust particles [3]. Overall, the conventional models for particle charging no longer apply to smaller dust particle sizes of a few nanometers. Therefore, sophisticated experiments and diagnostics, which are developed and presented in this thesis, are required to validate the newly developed models for nanoparticle charging.

1.2   Dust particles: Friend or foe

Dust particles can have an advantageous or a deleterious role based on the application and environment. One would heuristically regard dust particles as an insidious health hazard as we are constantly exposed to them everywhere we wander. Moreover, for instance, in fusion reactors, dust particles in a plasma can also threaten the process for which the plasma is formed. Sometimes even plasma is produced as a by-product, charging (neutral) dust particles in certain media, making it much more difficult to predict their trajectories and end-destination of particles. However, albeit counterintuitive, dust particles are sometimes valuable and intentionally generated for various applications. Conductive polymers and quantum dots are two instances of nanoparticles that are of great value. As a matter of fact, one can even manufacture these nanoparticles in a plasma. This expertise requires a fundamental understanding of the chemistry and physics of particle formation in dusty plasmas.

Nanoparticle contamination poses a perpetual threat to, for instance, the high-tech industry of photolithography. As the demand for processing units, i.e. microchips, with more processing speed and higher efficiency has only increased multifold over the recent years, the length scale of the reactors on these chips has shrunk from several micrometers in the 1970s to only a few nanometers lately. The manufacturing process of new processors and memory chips in photolithography machines includes using extreme ultraviolet photons with a wavelength of 13.5 nm to enable the printing of the fine structure of the designed processor on a wafer. This aggressive emission produces a photon-induced plasma interacting

with colloidal contaminants inside the machine, which is extensively studied and characterized [4, 5]. Moreover, the integrated circuit (IC) pattern on the reticle is also on the nanometer scale, making it susceptible to nanoparticle contamination.

Nanoparticles are sometimes beneficial and internally formed inside a plasma. Advantageous nanostructures such as quantum dots nanocrystallites [6, 7], polyaniline polymers [8], and silicon thin films [9] are synthesized inside reactive plasmas. Tailor-made nanostructured materials can, in principle, be synthesized by controlling plasma parameters (e.g. discharge power or gas composition). This enables, for instance, the size-controlled synthesis of photoluminescent nanocrystals [6], offering the ability to tune the semiconductor bandgaps for specific applications. Moreover, the electrostatic trapping effect can also be leveraged to control the properties of plasma-synthesized particles [10]. A fundamental understanding of nanoparticle formation or polymerization is the essential prerequisite for controlling the generation process. The nanoparticles' charge also plays a key role in the formation process, especially in the nucleation phase when the charge is governed by random processes, is small, and may change sign. As mentioned, these charging processes are far from understood for nanoparticles immersed in plasma, and therefore, there is an urgent need for diagnostics and experimental data to develop and verify theoretical frameworks.

1.3 Particle charge determination

As mentioned, dust particle charge is a key parameter for the applications of either plasma synthesis of beneficial nanostructures or contamination control of detrimental particles in complex ionized media. As for particle formation in a reactive plasma, a balance of forces (e.g. electrostatic and ion drag) during electrostatic particle trapping is a determining factor in the particle growth dynamics [11]. To prevent particle contamination in plasma processing devices, it is often necessary to steer particles' trajectories away from substrates and wafers [12] or induce particle "lofting" effects to remove particles from plasma-exposed surfaces [13]. It is, therefore, essential to understanding the charging mechanisms of dust particles upon formation or injection in the plasma.

Simultaneously with more demand for information about the charge of nanoparticles, a series of studies have been conducted recently. Theoretical studies, as mentioned earlier, focus mainly on predicting the charge of nanoparticles in plasma. As the theories and models often fall short of predicting the charge of nanoparticles, experimental research aiming at investigating the fundamental
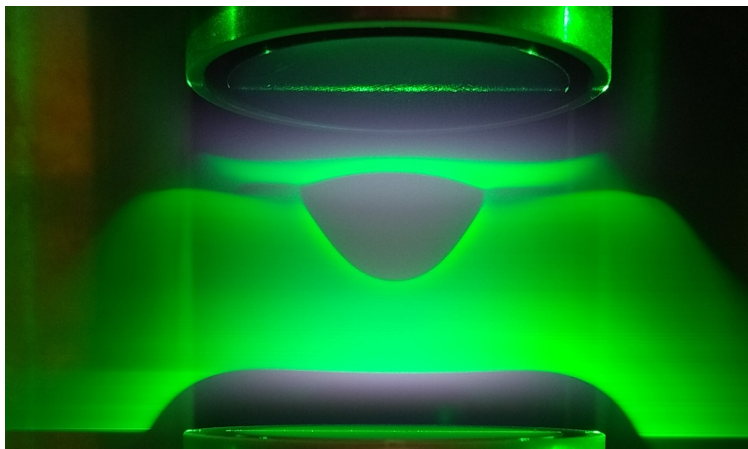
Figure 1.2: Dust cloud in a low-pressure laboratory plasma: a collection of particles (nano- to micrometer range) are formed and electrostatically confined in the plasma. Many interesting fundamental phenomena are observed in such plasmas, like dust density waves, crystal formation, and void formation. © Franco Greiner, Kiel-University.
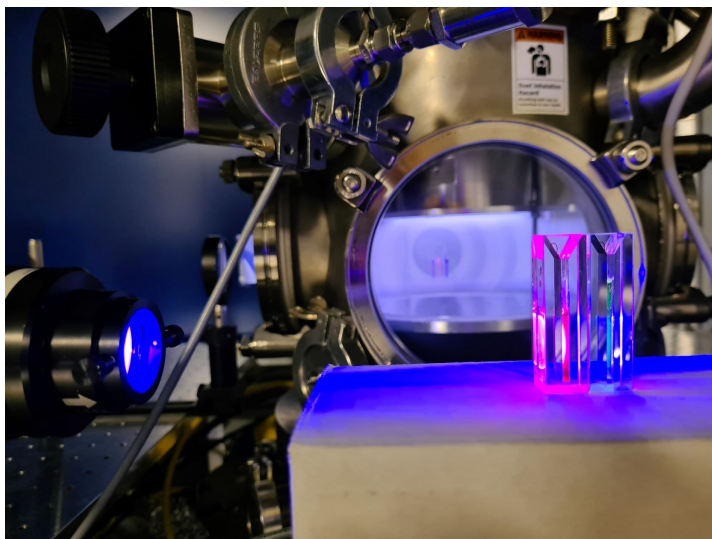
Figure 1.3: An exemplary setup in which plasma is formed. Nanoparticles can be synthesized in the plasma if reactive gases are inserted in the plasma. Nanoparticle charge visualization is achieved using the quantum dots shown in the solution form in the picture.

charging processes of nanoparticles needs to be enhanced. Most well-established diagnostic methods for particle charge measurement fail when applied to nanoparticles. The main reason for this shortcoming is that these methods, e.g. the method based on dust density waves [14] or the particle resonance methods [15, 16], are either directly or indirectly based on light scattering techniques, which faces a substantial loss of resolution because of reduction of signal-to-noise ratio due the sixth-power dependence of the signal intensity I to the particle size ($I \propto r_d^6$). So far, only Krüger *et al.* [17] have measured the charge of 40 nm silica (SiO_2) particles in plasma, using the shift in the absorption line of the transverse optical phonon in the infrared spectral range.

1.4 Charge visualization

Particle or surface charge visualization is an innovative method that uses the intrinsic property of semiconductor quantum dots for diagnostics. Quantum dots (QDs) are crystalline semiconductor nanomaterials that are sufficiently small to exhibit quantum confinement. Photoluminescence (PL) is the intrinsic property of the QDs, which can be potentially used for imaging or visualization of various processes. In recent years, QDs have been used for imaging of neuronal action potential for biomedical applications [18] or visualization of chemical and physical properties such as pH [19] and surface charge [20]. The PL property of the QDs depends on the size of a specific QD type; therefore, by an intricate control over size, as well as shape, shell thickness, and band alignment, one can design QDs as specific diagnostic tools. The interaction of QDs with the immediate local environment can therefore be sensed by monitoring the photoluminescence emission of the QDs. Specifically speaking, the QDs are utilized for local electric field sensing due to their associated quantum-confined Stark effect. It is well-established that the electric-field-induced (Stark) interaction resulting from an asymmetric electric field or single-point charge affects the band gaps of the QDs. The interaction with the external electric field leads to a reduction in recombination energy that is quadratically proportional to the perturbing field [21]. The distinct response of QDs to an external electric field, therefore, presents a promising prospect for nanoparticle charge measurements in dusty plasmas. The idea is schematically illustrated in figure 1.4: measuring the shift of the peak position in the photoluminescence spectrum as the QDs become charged.
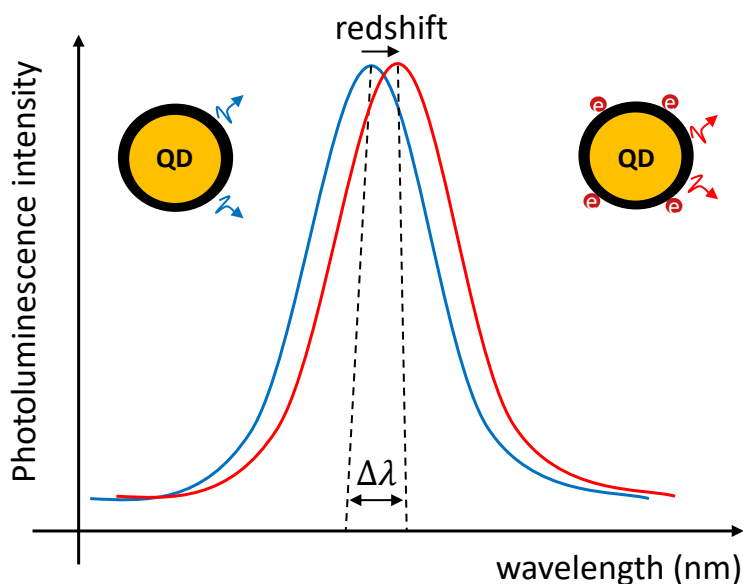
Figure 1.4: Charge visualization using CdSe-ZnS core-shell quantum dots: a redshift in the photoluminescence spectrum is observed upon charging of the quantum dots. The charge is measured by determining the redshift value ($\Delta\lambda$).

1.5 Thesis' focus and outline

This thesis investigates and contributes to the ultimate goal of using QD PL as a charge probe for plasma-levitated (nano)particles. To pave the way towards this novel diagnostic, two directions are explored in parallel in this thesis. First, a proof of principle for using QD PL as a probe to detect charges on a surface on the nanoscale will be generated by the deposition of QDs on a plasma-exposed surface and recording the QDs' PL spectra. Second, a combination of laser-induced photodetachment and microwave cavity resonance spectroscopy (MCRS) will be further developed in order to carefully control and measure the charge of plasma-levitated nanoparticles. A model system for this will be the afterglow of either an electronegative plasma or a nanodusty plasma. As will appear clearly from this thesis, both directions appear successful. This enables us to join them in near-future research efforts, i.e. performing PL measurements on plasma-levitated QDs while their charge is varied in a controlled way by (MCRS) calibrated laser-induced photodetachment.

Overall, the experimental research conducted in this thesis focuses on the following:

developing diagnostic methods for and gaining a fundamental understanding of the charging and decharging processes of negative ions, nanoparticles, and surfaces in low-pressure radiofrequency plasmas and the afterglow thereof.

The first diagnostic method developed in this thesis uses photoluminescent quantum dots to detect and visualize the charging of plasma-exposed surfaces in plasma. Subsequently, two well-established diagnostic methods are further developed to study the decharging of negative ions and dust particles in the afterglow of electronegative and reactive plasmas. The main questions this thesis poses to answer are:

1. Can photoluminescent quantum dots be used to detect and measure the electrical charge on surfaces and nanoparticles in plasma?

2. How do electrons and negatively-charged species behave during the afterglow of electronegative and reactive plasmas?

This thesis draws two research lines to answer these two questions. The first research line (research line I) follows the specific object of developing a novel diagnostic method based on quantum sensing. The second research line (research line II) aims at understanding the behaviour of electrons, negative ions, and negatively-charged nanoparticles in the temporal plasma afterglows.

The structure of the thesis is as follows:

Chapter 2 explains the relevant physics of different plasma types that are experimentally studied in the following chapters. The basics of quantum mechanics of quantum dots are also briefly described to provide a context for interpreting the following experimental results.

Chapter 3 elaborates on the diagnostic methods that are further developed and used for electron and negatively-charged species detection.

Chapter 4 presents an overview of the general experimental setup employed in this research. Detailed descriptions of the two setups are provided. It is also explained how the diagnostic methods are implemented.

Research line I is comprised of one chapter:

Chapter 5 provides a study on the visualization of the surface charge using photoluminescent quantum dots. It is first proven that the quantum dots detect the surface charge when deposited on a substrate surface and exposed to a low-pressure radiofrequency plasma. Subsequently, it is discussed how quantum dots photoluminescence is also sensitive to variations in surface charge density as the plasma conditions are subject to change.

Research line II is comprised of two chapters:

Chapter 6 presents and discusses the experiments in which electrons and negative ion behaviour are studied in an electronegative plasma ignited in oxygen gas. The so-called microwave cavity resonance spectroscopy (MCRS) diagnostic technique measures the density of electrons and, combined with laser-induced photodetachment (LIP), measures oxygen negative ions densities. These densities are measured temporally resolved during the plasma afterglow to study electron and negative ions decay as the plasma conditions are subject to change.

Chapter 7 discusses the decay of negatively-charged species formed in the early stages of particle growth in a reactive plasma ignited in argon-diluted acetylene gas. The previously developed diagnostic techniques of MCRS and LIP are employed to measure electron and negatively-charged species densities temporally resolved during the plasma afterglow.

Chapter 8 draws the general conclusions from the research presented in this thesis.

Chapter 2

Theories

Abstract

In this chapter, the relevant physics of plasmas and quantum dots is discussed. The general theory regarding three types of plasmas (i.e. electropositive, electronegative, and dusty plasmas) is elaborated on. Since quantum dots will be used as probes for charge visualization later on in this thesis, essential aspects of quantum dot solid-state physics that are indispensable to discussions of the results are also included. Since this diagnostic technique is newly designed to investigate charge-related effects of surfaces in complex ionized media. The relevant theories regarding plasma surface charging are also explained.

2.1 Introduction

Multitudinous phenomena stem from the added complexity of dusty plasmas compared to standard dust-free plasmas. The key process of paramount importance is the charging phenomenon, i.e. how surfaces and particles acquire charge from plasmas (the mechanisms) and how much charge can be ascribed to objects immersed in plasma. Therefore, the theoretical framework presented in this chapter lays the foundation for understanding the dynamics and phenomena in plasmas, aiming to investigate particle and/or surface charge.

A diagnostic method is designed and developed to study the charging of surfaces in a low-pressure capacitively coupled plasma. This novel diagnostic technique visualizes the charge gathered by an electrically floating surface immersed in the plasma. Quantum dots and their photoluminescence properties are used for the visualization of this charge. The theories underlying this technique are elaborated on in this chapter.

This chapter is organized as follows: first, theoretical concepts regarding the physics of plasmas are elaborated in section 2.2. Three different plasma types, electropositive plasmas, electronegative plasmas, and dusty plasmas, are defined and discussed together with their key features. Furthermore, dust Particle formation and charging in reactive (argon-acetylene) discharges are discussed in section 2.4. Subsequently, the physics of quantum dots and their photoluminescence property is briefly addressed in section 2.5.

2.2 Plasma

Low-temperature plasma physics is the study of charged particles that are present in sufficient numbers so that the long-range Coulomb force is a factor in determining their statistical properties, yet low enough in density so that the force due to a near-neighbor particle is much less than the long-range Coulomb force exerted by the many distant particles. It is the study of low-density ionized gases.

Three different plasma types are generated to serve the experimental research conducted in this thesis: electropositive, electronegative, and reactive dusty plasmas. In contrast to electropositive plasmas, electronegative plasmas contain negative ions besides positive ions, electrons, and neutrals, while plasmas formed in reactive gases (argon-acetylene, in this case) grow solid nano- to micrometer-sized particles internally. Before discussing the peculiar characteristics of these different types of plasma, we start by defining the basic concepts of plasma in general.

2.2.1 Debye length

Generally, the electrostatic potential (ϕ) around an isolated particle with charge q from a distance (r) is:

$$\phi = \frac{q}{r}.\tag{2.1}$$

Specifically, in a plasma, electrons are attracted to the vicinity of an ion and shield its electrostatic field with respect to the rest of the plasma [22]. Similarly, an electron at rest repels other electrons and attracts ions. This effect alters the above-mentioned potential in the vicinity of a charged particle, i.e. the so-called screening effect. The potential of a charge at rest in a plasma is, therefore, given by:

$$\phi = \frac{q}{r}\, exp(\frac{-r}{\lambda_D}),\tag{2.2}$$

where λ_D is the Debye length originally defined in the Debye-Hückel theory of electrolytes [22]. For an electropositive plasma:

$$\lambda_D = \left(\frac{\kappa_B T}{8\pi n e^2}\right)^{1/2} \approx 4.9 \left(\frac{T}{n}\right)^{1/2},\tag{2.3}$$

where n is the density of electrons (or ions), in m^{-3}, T is the plasma temperature, and κ_B is Boltzmann's constant.

The Debye length is a measure of the sphere of influence of a given test charge in a plasma. In other words, the Debye length determines the range outside which the plasma can shield any applied potential.

The distinct contributions of electrons and ions to the general Debye length (λ_D) can be conceived as:

$$\frac{1}{\lambda_D^2} = \frac{1}{\lambda_{D_e}^2} + \frac{1}{\lambda_{D_i}^2} = \frac{\lambda_{D_e}\lambda_{D_i}}{\sqrt{\lambda_{D_e}^2 + \lambda_{D_i}^2}},\tag{2.4}$$

where λ_{D_e} and λ_{D_i} are electron and ion Debye lengths, respectively. These two Debye lengths are defined as:

$$\lambda_{D_e} = \left(\frac{\kappa_B T_e}{8\pi n_e e^2}\right)^{1/2},\tag{2.5}$$

and

$$\lambda_{D_i} = \left(\frac{\kappa_B T_i}{8\pi n_i e^2}\right)^{1/2}.\tag{2.6}$$

Here n_e and n_i are the density of electrons and ions, and T_e and T_i are the temperature of ions and electrons, respectively.

2.2.2 Plasma sheath

The positively charged transition layers between the quasi-neutral, equal electron and (positive) ion densities ($n_e = n_i$), region of plasmas to walls or floating surfaces in contact with that plasma are called plasma sheaths. To understand how the space charge sheath region is formed, it is supposed that an electrically floating object is inserted in an electropositive plasma. Initially, the object collects electrons and positive ions as these always have thermal volecities [23]. The electron and positive ion currents to the floating object are expressed as:

$$J_e = -e\Gamma_e = -\frac{1}{4}en_e\bar{v}_e = -en_e\sqrt{\frac{\kappa_B T_e}{2\pi m}}, \tag{2.7}$$

$$J_i = -e\Gamma_i = -\frac{1}{4}en_i\bar{v}_i = -en_i\sqrt{\frac{\kappa_B T_i}{2\pi M}}. \tag{2.8}$$

Here $\bar{v}_e$, $\bar{v}_i$, m, M, T_e, and T_i are thermal velocities, masses, and temperatures of electrons and ions, respectively. Since $m \ll M$ and $T_e \geq T_i$, one can conclude that $J_e \gg J_i$, meaning that the object would accumulate a negative charge. Diffusion of electrons towards plasma confining walls or floating surfaces leads to depletion of electrons within regions close to those walls and surfaces, as electrons are more mobile compared to ions. Hence, a positive space charge region is formed near each wall or floating surface, leading to a potential profile $\phi(x)$ (see figure 2.2) that is positive near the plasma bulk and falls exponentially near the walls or surfaces. This potential drop causes electrons initially traveling towards the walls to reflect back towards the plasma while; conversely, the ions are accelerated and bombard the walls and surfaces. The concept of the plasma sheath in a confined plasma is illustrated in Fig 2.1.

2.2.3 Floating potential

When an object is immersed in an electropositive plasma, a positive space charge sheath forms around this object to compensate for the significant mobility difference between positive ions and electrons. A potential difference, therefore, exists between the surface of this object (at the lower potential) and the plasma. If the object is electrically floating, this potential difference adjusts itself so that the ion flux (equation 2.7) is equal to the electron flux (equation 2.8) at the surface,
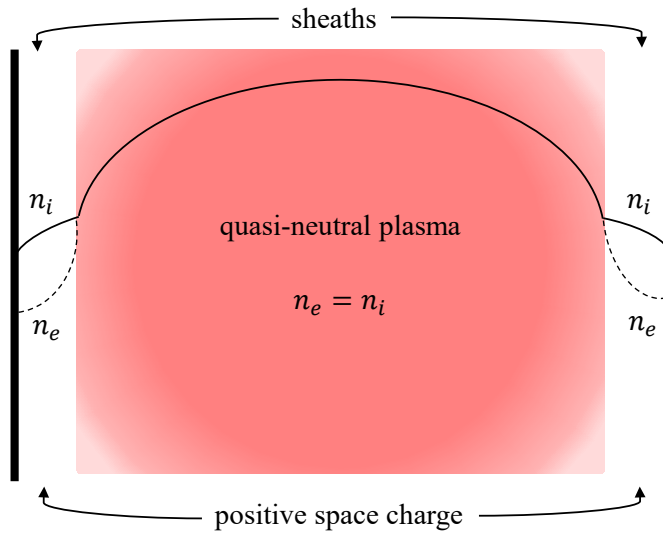
Figure 2.1: Schematic illustration of a confined plasma between two walls. The quasi-neutral plasma region meets the walls through a positive space charge layer, i.e. plasma sheath.
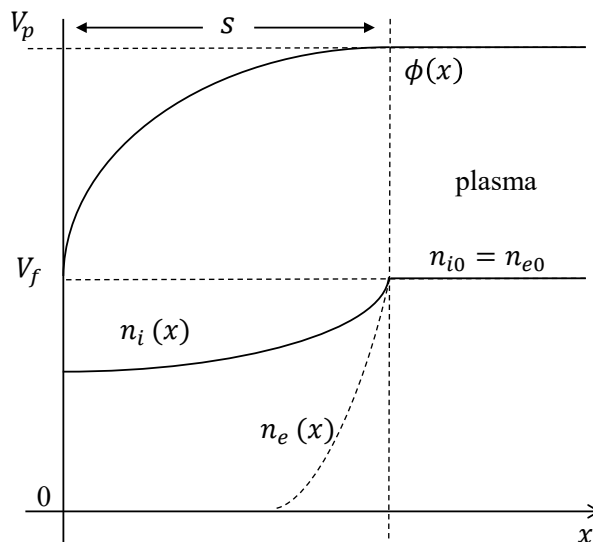
Figure 2.2: Illustration of the significant potential drop across a plasma sheath with the thickness (s) from the plasma potential (V_P) to the floating potential (V_f). The electron density ($n_e(x)$) sharply decays while the positive ion density ($n_i(x)$) declines partially [23].

thereby ensuring that no current is drawn from the plasma. Such a potential is called the DC floating potential, which is necessarily negative with respect to the plasma's potential since $T_e \geq T_i$ and $m \ll M$.

Assuming the electron flux is retarded by a surface so that only electrons with more energy than $e\Delta\phi$ in a Maxwellian distribution of electrons with a temperature of T_e could reach it, this electron flux is given by:

$$\Gamma_e = \frac{n_s \bar{v}_e}{4} exp\left(-\frac{e\Delta\phi}{\kappa_B T_e}\right). \tag{2.9}$$

The positive ion flux towards a floating surface is determined by the Bohm criterion [24] (i.e. necessary initial ion speed for sustaining the plasma sheath.), and yields:

$$\Gamma_i = n_s u_B = n_s \left(\frac{\kappa_B T_e}{M}\right)^{1/2}. \tag{2.10}$$

Satisfying the balance of fluxes at the surface ($\Gamma_e = \Gamma_i$), the floating potential (V_f) of a surface exposed to a region of DC plasma with cold ions and Maxwellian electrons is:

$$V_f = \frac{\kappa_B T_e}{2e} \ln\left(\frac{2\pi m}{M}\right). \tag{2.11}$$

Since the plasmas formed for the research in this thesis are radio frequently driven (RF), it is necessary to briefly discuss the effects of RF excitations (in the MHz range) on the floating potential. During continuous RF modulation, the instantaneous electron flux arriving at the floating surface will be modulated through the dependence of the Boltzmann retardation factor on the instantaneous potential [23], whereas that of the ions will remain unchanged. The conditions must be satisfied that the electron flux averaged over the RF cycle equals the steady ion flux, preventing net currents across the sheath and integrated over one full RF cycle. The RF floating potential includes an additional RF voltage across the sheath, known as RF self-bias. Therefore the total floating potential in RF plasmas is:

$$V_{f_{RF}} = \frac{\kappa_B T_e}{e}\left[\frac{1}{2}\ln\left(\frac{2\pi m}{M}\right) - \ln I_0\left(\frac{eV_1}{\kappa_B T_e}\right)\right], \tag{2.12}$$

where V_1 is the amplitude of the RF voltage across the sheath. Here, I_0 is the zero-order modified Bessel function. The first term on the right-hand side of equation 2.12 is the DC floating potential, while the second term represents the RF self-bias.
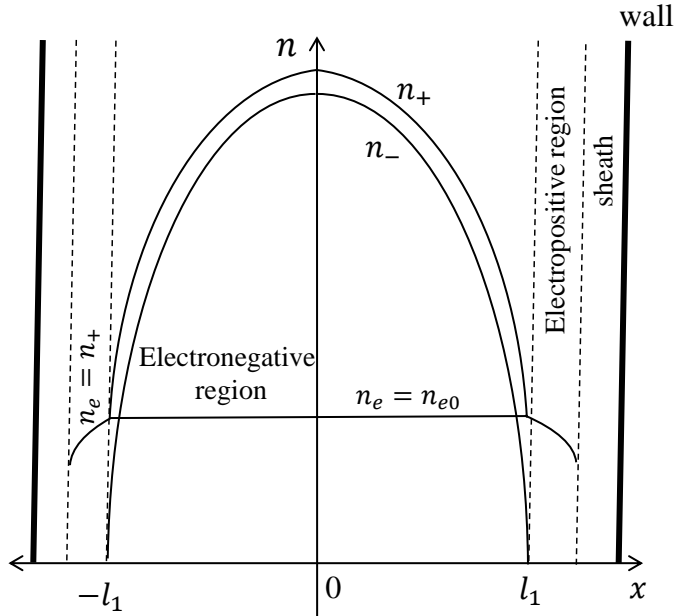
Figure 2.3: Spatial distribution positive ion, negative ion, and electron densities in an electronegative plasma. Electronegative, electropositive, and sheath regions are illustrated.

2.2.4 Sheath thickness

The last plasma parameter indispensable for the conducted research is the floating sheath thickness. It is assumed that the mean free path of the ions in the plasma is larger than the Debye length ($l_{mfp} \gg \lambda_D$), i.e. a collisionless sheath, and that the dimensions of the floating object are larger than the Debye length ($\lambda_D \gg r$), i.e. a thick sheath. According to the Child-Langmuir law [23] and based on these assumptions, the sheath thickness is [25]:

$$s = \frac{2}{3} \left(\frac{e n_i u_B}{\varepsilon_0} \right)^{-1/2} \left(\frac{2eV^3}{M} \right)^{1/4} \approx 0.8 \lambda_{De} \left(\frac{eV}{\kappa_B T_e} \right)^{3/4}. \tag{2.13}$$

Here ε_0 is the vacuum permittivity, V is the potential drop across the sheath, and λ_{De} is the electron Debye length. Later in this thesis, in chapter 5, The sheath thickness is estimated using the Child-Langmuir law and cross-checked with measurements performed by a CCD camera. The sheath thickness is subsequently used for plasma sheath electric field estimations.

2.3 Electronegative plasma

Electronegative plasmas consist of negative ions as well as electrons, positive ions, and neutrals. The negative ions are mainly formed through (dissociative) electron attachment. Adding negative ion species profoundly complicates the equilibrium plasma structure in a discharge. Stratification of plasma into an electronegative core and an electropositive edge is a distinct characteristic associated with electronegative plasmas. The stratification occurs because the ambipolar field required for confining energetic electrons drifts the negative ions into the central region of the plasma. The ambipolar field, located at sheath edges, originates from the local maximum of electron density in the electropositive region of the plasma and the sheath voltage developed between the plasma and the walls [26]. Since negative ions possess less energy compared to electrons, a weaker field is required to confine them in the core. The spatial distribution of species in a stationary plasma between two walls is illustrated in figure 2.3, where the higher temperature electrons, due to their lower mass, form a nearly uniform density in the presence of negative ions. An electropositive region is formed between the electronegative region and the sheath region.

The feedstock gas used for forming the electronegative plasmas in our experiments is oxygen. Oxygen is weakly electronegative with a dissociative attachment rate K_{att} with a threshold energy of 4.7 eV. Since oxygen plasma is prevalent in industries, numerous experimental studies have been conducted to determine the densities of various species. The dominant negative ions are measured to be O^- while the dominant positive ion is O_2^+. From experiments performed by Stoffels *et al.* [27], it was found that O^- is mainly produced by dissociative attachment of O_2 while the positive ion-negative ion recombination is the main loss channel of O^- in low-pressure RF-CCP plasmas. Generally, the reactions in table 2.1 are proposed [28] to occur in a 13.56 MHz asymmetric capacitive discharge at a low pressure of 1-100 Pa.

Here O_2^+ and electrons are created by electron impact ionization of O_2. Due to the trapping of negative ions within the discharge center, their flux towards the chamber walls is obstructed; therefore, the principal loss channel for negative ions is recombination with positive ions in the volume. For sufficiently high pressure, another negative ion loss channel (i.e. detachment due to collision with atomic oxygen O or oxygen molecule metastable $O_2(a^1\Delta_g)$) must be included, accounting for additional electron release during the afterglow phase (i.e. the decaying plasma phase after the plasma power is terminated). Positive ions are either lost to the walls by diffusion or by recombination in the volume with negative ions.

Table 2.1: A simplified set of volume reactions proposed for simulating electronegative oxygen plasma [28].

Reaction	Process
$e + O_2 \rightarrow O_2^+ + 2e$	ionization
$e + O_2 \rightarrow O^- + O$	dissociative attachment
$O_2^+ + O^- \rightarrow O_2 + O$	recombination
$O_2^+ + O_2 \rightarrow O_2^+ + O_2$	elastic scattering
$O_2^+ + O_2 \rightarrow O_2 + O_2^+$	charge transfer
$O^- + O_2 \rightarrow O^- + O_2$	elastic scattering
$O^- + O \rightarrow O_2 + e$	detachment
$O^- + O_2(a^1\Delta_g) \rightarrow O_3 + e$	detachment

2.3.1 The afterglow of electronegative plasma

Additional to the steady-state operation of electronegative plasmas (ignited in oxygen and acetylene gases), the temporal afterglow of the plasma is experimentally investigated in this thesis (in chapter 6 and chapter 7). A Temporal afterglow plasma is a mixture of ions, electrons, excited species, and neutral gas that occurs when the plasma is not actively powered anymore and ionization cannot be sustained. In such an afterglow, the deposited energy in the discharge, ionizing the gas and exciting metastable species, relaxes. Specifically, the electron temperature cools from several electron volts to room temperature (0.025 eV) due to collision and diffusion processes [29]. After switching off the plasma, plasma species are continuously lost by diffusion. While quasi-neutrality holds in the early stages of the afterglow, and the charged species' transport is governed by ambipolar diffusion, in the later stages, quasi-neutrality ceases, and there is an ambipolar to free diffusion transition. Furthermore, the sheath voltage and electrostatic ambipolar fields resulting in the stratification of the electronegative plasma, also collapse.

Electron cooling, diffusion of plasma species, and the collapse of ambipolar fields all lead to a series of interesting phenomena associated only with the temporal afterglow of electronegative plasmas. As the electron temperature relaxes, no more negative ions are produced via dissociative attachment process. This, combined with a diffusive loss of negative ions due to the sheath potential collapse, leads to a diffusive loss of the negative ions towards the walls and surfaces. This diffusion may have consequences for plasma surface processing applications or can be regarded as a way to extract negative ions. The increased flux of negative ions towards plasma-containing walls and surfaces occurs in the so-called recombination-dominated regime, where the negative ions are lost mainly due to recombination. Moreover, in this case, a transition occurs from an electron-dominated plasma to a positive-ion-negative-ion plasma due to the rapid diffusion and subsequent decay of electrons at the early afterglow [30].

In a detachment-dominated electronegative plasma, the pressure is sufficiently high to allow collisions of negative ions with neutrals and metastables and subsequently lead to the loss of negative ions due to autodetachment. For instance, for an oxygen plasma:

$$O^- + O \rightarrow O_2 + e, \tag{2.14}$$

$$O^- + O_2(a^1\Delta_g) \rightarrow O_3 + e, \tag{2.15}$$
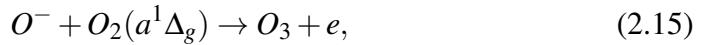
the collision of a negative (oxygen) ion with either a ground state or a metastable atom leads to the neutralization of the negative ions and the release of an electron. Therefore, an electron release is observed shortly after the termination of plasma power [28]. The necessary condition for a detachment-dominated electronegative plasma is defined by Kaganovich *et al.* [31]. This condition sets a minimum pressure for the electronegative plasma to be regarded as detachment-oriented and to exhibit electron release in the early afterglow. Furthermore, negative ions can be trapped long within the afterglow phase due to this electron release [32]. These phenomena and their underlying consequences will be investigated in chapter 6.

2.4 Dusty plasma

A dusty plasma is referred to as a plasma containing, besides its normal components of neutrals, ions, and electrons, nanometer- to micrometer-sized dust particulates, often called dust particles. Depending on the conditions of the experiments, these particles can attain positive or negative electrical charges. The latter is generally the case due to the higher mobility of the electrons and negligible

electron release from dust particles. Generally, dust particles of micrometers in size charge up to thousands of elementary charges. Depending on the particle's radius, r_d, the inter-particle distance a, and the Debye length λ_D two different cases may occur:

- $r_d \ll \lambda_D < a$, dust in a plasma,

- $r_d \ll a < \lambda_D$, dusty plasma.

In the first case, $r_d \ll \lambda_D < a$, the charged dust particles are considered a collection of isolated screened grains as a sheath region (similar to the sheaths around a floating surface as discussed in section 2.2.2) surrounds each particle. In the second case, $r_d \ll a < \lambda_D$, the charged dust particles participate in the collective behavior and consequently are treated as massive sets of connected charged particles. The plasma-particle configuration discussed in chapter 7 falls under the category of dusty plasma. There are a series of differences between dusty plasmas and electron-ion plasma, of which the two instances are briefly discussed here: macroscopic neutrality and Debye shielding. A dusty plasma is macroscopically neutral, meaning that the net resulting electric charge in a dusty plasma is zero, with all external forces absent. Hence, the equilibrium charge neutrality condition stipulates that:

$$\langle Z_i \rangle n_i = \langle Z_d \rangle n_d + n_e, \tag{2.16}$$

where $\langle Z_i \rangle$ is the average charge number of the ions, $\langle Z_d \rangle$ the average charge number of the dust particles, and n_d the dust particle number density.

Debye shielding is a fundamental characteristic of plasmas, enabling the shielding of electric fields of individually charged particles or surfaces immersed in it. The characteristic distance governing this mechanism, i.e. the Debye length, is a measure of distance outside which the electric potential of an imaginary charged entity is screened by charge separation responses in the plasma. The Debye length is explicitly defined for electron-ion plasmas previously in this chapter. However, with the presence of dust particles, one needs to take into account the contribution of both electron and ion Debye lengths (see equations 2.4, 2.5, and 2.6).

For a dusty plasma with negatively charged dust particles, as in the case in chapter 7, the electron density is relatively depleted ($n_e \ll n_i$), and the electron temperature is elevated ($T_e \gg T_i$). Therefore $\lambda_{D_e} \gg \lambda_{D_i}$ and $\lambda_D \simeq \lambda_{D_i}$. This implies that the shielding distance in a dusty plasma is mainly determined by the temperature and number density of the ions. This is in contrast with the situation of a low-temperature plasma without dust particles, in which the shielding

distance or thickness of the sheath is mainly determined by the electron Debye length ($\lambda_D \simeq \lambda_{D_e}$).

2.4.1 Particle formation

Dust particles are either internally formed inside plasma or externally injected into the discharge. For many applications, e.g. synthesis of polymers [33] and nanostructures [34], dust particles are internally formed within a plasma ignited in a reactive gas. The plasma formed in a feedstock monomer gas initiates chemical processes that lead to the formation of negative ions and radicals and, subsequently, via polymerization, nucleation, and coagulation, to micrometer-sized dust grains. Since in our experiments (see chapter 7) acetylene (C_2H_2) is used as a feedstock reactive gas for particle formation, this section is focused on the reactions and processes occurring in acetylene plasmas.

The basic picture of dust particle formation in low-pressure plasmas at low powers is drawn by Bouchoule [35] and is illustrated in figure 2.4. This dust particle formation process is comprised of four stages:

1. **Negative ions formation and polymerization**: This stage pertains to the dissociation of precursor molecules into negative ions and radicals, initiating the polymerization processes. During this stage, negative ions (anions) are trapped within the plasma where monomers can react to a radical to form the first polymer in the polymerization chain reaction [36].

   First, negative ions are formed via the dissociative electron attachment process whereby an electron collides with a monomer molecule to form an anion and a hydrogen radical:

$$C_2H_2 + e \rightarrow C_2H^- + H. \qquad (2.17)$$
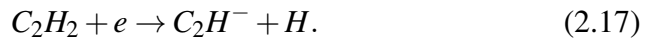
   Primary C_2H^- anions can subsequently trigger a consecutive chain of polymerization reactions that generally evolves as:

$$C_{2n}H^- + C_2H_2 \rightarrow C_{2n+2}H^- + H_2, \qquad (2.18)$$
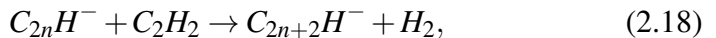
   where the initial polymerization of C_2H^- corresponds to n = 1. This process is commonly referred to as the Winchester mechanism [37]. An alternative initiation reaction scheme was proposed [38] to account for mass spectroscopy measurements of Deschenaux *et al.* [39]. The presence of the vinylidene anion (H_2CC^-), revealed in mass spectroscopy measurements,

suggests another pathway for the polymerization reaction chain. In fact, a majority of the dissociative electron attachment reactions on acetylene monomer molecules lead to the formation of vinylidene anions:

$$C_2H_2 + e \rightarrow H_2CC^-, \tag{2.19}$$

which in turn could participate in the polymerization process:

$$H_2CC^- + C_2H_2 \rightarrow C_2H_2^- + H_2, \tag{2.20}$$
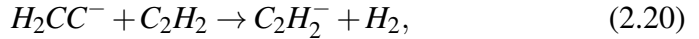
which can resume through the Winchester mechanism (equation 2.18).

2. **Nucleation**: This stage pertains to a brief period during which the polymers and primary clusters reach a critical size of (about 5 nm). The charge of particles in this stage is governed by the random arrival of positive ions and electrons. Therefore it is subject to time-varying fluctuations.

3. **Coagulation**: This stage pertains to the fusing of proto-particles together upon reaching a critical density when insufficient electrostatic repulsion occurs between the particles. This leads to the formation of relatively larger particles of tens of nanometers. The dust particles in this stage acquire a permanent negative charge of several thousand electrons due to an initially higher flux of electrons to the surface of the particles. The initial higher electron flux continues until reaching a charge equilibrium when the electron and positive fluxes are equal. Moreover, this stage is characterized by a sharp decrease in electron density and an abrupt increase in electron temperature since the dust particles act as sinks for electrons and the (constant) deposited discharge power is shared with fewer electrons.

4. **Particle growth**: This stage pertains to steady size-growth of the particles by means of accretion (i.e. surface growth). In this stage, the particles' radii increase roughly linearly with time [40], mostly due to impinging radicals on the surface of the particles. According to Van de Wetering *et al.* [41], the surface growth rate is measured to be 1 to 2 nm/s under typical dusty plasma operation conditions in Ar/C_2H_2 plasma.
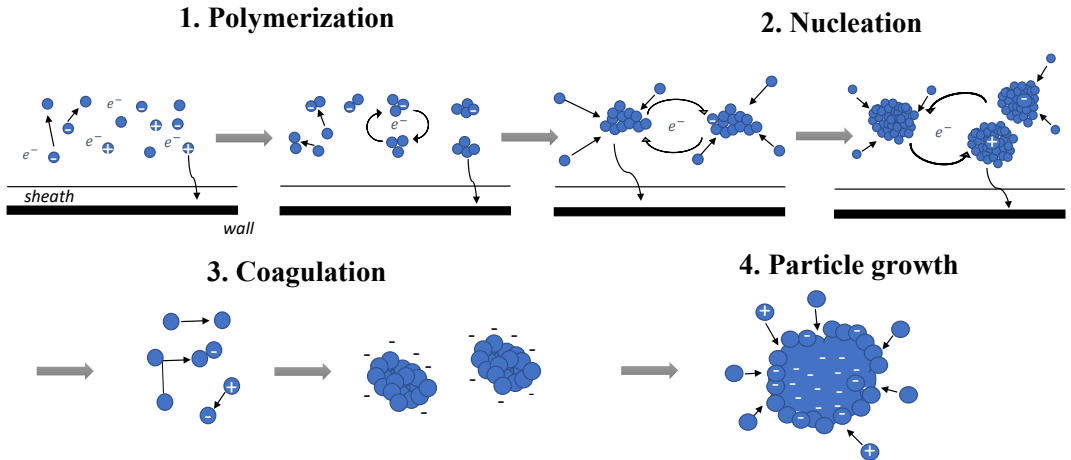
Figure 2.4: Schematic illustration of the four stages of particle formation, inspired by figure 2.1 in [35].

2.4.2 Charging mechanisms

As discussed previously, when the floating potential concept was defined, any macroscopic object acquires a negative charge upon immersion in plasma. The same charging mechanism also applies to small dust particles formed inside the plasma. Charging is, therefore, an inherent phenomenon associated with the plasma environment, which determines the dynamics of dust particles in either the steady-state situation or in a temporal/spatial afterglow plasma. Dust particles are often assumed as negatively charged species with several hundred to thousands of (negative) elementary charges that are confined within the plasma.

Orbital Motion Limited (OML) theory

Orbital motion limited (OML) theory was first developed to describe spherical probes [42] (e.g. Langmuir probes) and was later applied to plasma-levitated dust particles. Consider a generic situation of a dust particle regarded as an isolated probe, the Debye length exceeding the particle's radius ($\lambda_D \gg r_d$) and a low-temperature discharge with $T_e \geq T_i$ and $\lambda_D \simeq \lambda_{D_i}$. In this case, the presence of other particles does not affect the motion of electrons and ions in the vicinity of a single particle. Then, assuming an equilibrium of charge (Q_d) resulting from equal electron and ion currents to a dust particle leads to:

$$\frac{dQ_d}{dt} = I_i - I_e = 0, \tag{2.21}$$

where I_i and I_e, are the ion and electron currents which are defined as:

$$I_i = \sqrt{8}\pi r_d^2 n_i e \bar{v}_i \left(1 - \frac{e\Phi_d}{\kappa_B T_i} \right), \tag{2.22}$$

$$I_e = \sqrt{8}\pi r_d^2 n_e e \bar{v}_e \exp\left(\frac{e\Phi_d}{\kappa_B T_e} \right). \tag{2.23}$$

Based on these equations, the floating potential of the dust particle (Φ_d) can be derived as:

$$\Phi_d \approx -0.36 T_e \ln\left(\frac{m T_i n_i^2}{M T_e n_e^2} \right), \tag{2.24}$$

which depends on the ratio of the electron and ion temperatures, masses, and densities. Typically, $\Phi_d \approx -$ few T_e in eV. The dust particle charge Q_d is then obtained by assuming the particle is a spherical capacitor with a capacity of C_d:

$$Q_d = C_d \Phi_d = 4\pi\varepsilon_0 r_d \Phi_d. \tag{2.25}$$

However, this generic assumption is no longer valid when small, nanometer-sized particles are considered. Besides the collection of electrons and positive ions, several other mechanisms, such as electron attachment, ion capture, and recombination processes at the surface of the particles, have to be taken into account. Hence, initially, neutral nanoparticles might become positively charged as well due to secondary electron emission and photoionization.

2.4.3   Forces on particles

The dynamics of charged particles in plasmas are of fundamental interest, and it is necessary to consider an interplay of various forces on the dust particles to understand various phenomena occurring in dusty plasmas.

There are various forces that govern the dynamics of dust particles in the plasma. The forces acting on a charged dust particle of mass m_d and velocity v_d can be expressed in a basic equation as:

$$m_d \frac{dv_d}{dt} = F_E + F_g + F_i + F_n + F_T + F_P. \tag{2.26}$$

Here, F_E is the electric force associated with the electric fields interacting with the particle's charge, and F_g is the gravitational force. F_i is the ion drag force associated with the momentum transfer of an ion to a dust particle by direct ion impact and/or a Coulomb interaction between a charged particle and ion, causing deflection of the particle's trajectory. F_n is the neutral drag force pertaining to the momentum transfer between neutral gas particles and dust particles stemming from their relative motions. Moreover, F_T is the thermophoretic force associated with momentum transfer due to a temperature gradient in the neutral gas, and F_P is the radiation pressure force.

Consideration of multiple forces and the force balance are crucial in the case of a dusty plasma with micrometer-sized particles. However, the force balance is of only marginal importance when nanometer-sized particles in plasma are the case (as in chapter 7). Therefore, only a brief discussion about forces is included here.

2.5 Quantum dots

Quantum dots (QDs) are nanometer-sized crystalline semiconductors that are inherently characterized as zero-dimensional quantum wells for charge carriers. Depending on the size of the quantum well, i.e. the diameter of the quantum dot, the optical properties are subject to change. The most fundamental and interesting property of quantum dots, which is used as a diagnostic technique in our experiments, is photoluminescence (PL). As a semiconductor comprises a well-defined energy band gap, a quantum dot can be excited upon illumination by a photon with an energy more than its band gap energy. This band gap energy depends on the size of the quantum dots; therefore, the PL emission wavelength of a collection of QDs depends on their size and size distribution. The PL process is comprised of three steps: excitation, relaxation, and emission, which will be discussed later in this section. Semiconductor quantum dots are able to confine charge carriers, e.g. electrons, in all the spatial dimensions. These zero-dimensional nanostructures display discrete energy levels analogous to those of an atom. Therefore, physical phenomena such as perturbation of energy levels in an electric field can be also associated with QDs energy levels. As QDs can be synthesized in different sizes and, therefore, their properties can be tuned for specific purposes and experiments, the term "artificial atoms" is coined to metaphorically describe them. Similar to splitting Rydberg energy levels of argon atoms in plasma sheath electric fields [43] and the diagnostic based on the Stark shift of gaseous argon atom's energy levels in plasma [44], QDs also exhibit similar

shifts in energy levels in external electric fields.

In this section, two of the most important properties of QDs that are used for the diagnostic technique in chapter 5, PL and the quantum-confined Stark effect, are elaborated. Subsequently, the effect of temperature variations on the relevant properties of QDs is briefly discussed to later address the temperature issue encountered in chapter 5.

2.5.1 Finite spherical quantum well model

The quantum dots used in the experiments described in this thesis are core-shell QDs consisting of a CdSe core and a ZnS shell. Essentially, a quantum dot can be modeled as a spherical, three-dimensional quantum well for charge carriers. The behavior of charge carriers trapped inside the quantum well is governed by quantum mechanics for which Schrödigner equation needs to be solved.

The wavefunction ($\Psi(x,t)$) for a particle with mass m and affected by a potential $V(x)$ is obtained by solving the Schrödigner equation [45]:

$$-\frac{\hbar^2}{2m}\frac{\partial^2}{\partial x^2}\Psi(x,t) + V(x)\Psi(x,t) = i\hbar\frac{\partial}{\partial t}\Psi(x,t),\qquad(2.27)$$

where $\hbar$ is the reduced Planck constant and i is the imaginary unit. Assuming that Ψ is time-independent and with some simplifications, the time-independent Schrödigner equation is given by:

$$-\frac{\hbar^2}{2m}\frac{\partial^2}{\partial x^2}\psi(x) + V(x)\psi(x) = E\psi(x),\qquad(2.28)$$

where E represents the energy of the particle.

The expression of equation 2.28 for a three-dimensional spherical quantum well in spherical coordinates of r, θ, and ϕ is:

$$-\frac{\hbar^2}{2m}\left[\frac{1}{r^2}\frac{\partial}{\partial r}(r^2\frac{\partial\psi}{\partial r}) + \frac{1}{r^2\sin\theta}\frac{\partial}{\partial\theta}(\sin\theta\frac{\partial\psi}{\partial\theta}) + \frac{1}{r^2\sin^2\theta}(\frac{\partial^2\psi}{\partial\phi^2})\right] + V(r,\theta,\phi)\psi = E\psi,$$
$$(2.29)$$

where $\psi = \psi(r,\theta,\phi)$.

The variables can be separated using $\psi(r,\theta,\phi) = R(r)Y(\theta,\phi)$. By regarding only the radial part and assuming that the potential $V(x)$ is constant over θ and ϕ, this expression can be further simplified. Rewriting equation 2.29 with the substitution variable $u(r) \equiv rR(r)$ and using $l(l+1)$ as a separation constant, the radial equation can be derived as:

$$-\frac{\hbar^2}{2m}\frac{d^2u(r)}{dr^2} + \left[V(r) + \frac{\hbar^2}{2m}\frac{l(l+1)}{r^2}\right]u(r) = Eu(r). \tag{2.30}$$

This equation is identical in form to the time-independent Schrödinger equation (equation 2.28) with an additional term in the expression for the effective potential:

$$V_{eff}(r) = V(r) + \frac{\hbar^2}{2m}\frac{l(l+1)}{r^2} \tag{2.31}$$

Subsequently, the potential for confining a particle inside the quantum well can be defined as a finite barrier of r_w for the particle. For convenience, the potential outside r_w is assumed to be equal to zero. The potential difference relative to the potential outside r_w is V_0. This results in a potential well with a depth of $-V_0$ and radius r_w. The expression for the potential then reads as follows:

$$V(r) = \begin{cases} -V_0 & r \le r_w \\ 0 & r > r_w \end{cases} \tag{2.32}$$

A schematic depiction of the potential is provided in figure 2.5. Substituting this potential in the radial equation (equation 2.30), the radial wave equations can be expressed for both inside and outside the well as:

$$\begin{cases} -\frac{\hbar^2}{2m}\frac{1}{r^2}\frac{d}{dr}(r^2\frac{dR(r)}{dr}) + [-V_0 - E]R(r) = -\frac{l(l+1)\hbar^2}{2mr^2}R(r) & r \le r_w \\ -\frac{\hbar^2}{2m}\frac{1}{r^2}\frac{d}{dr}(r^2\frac{dR(r)}{dr}) - ER(r) = -\frac{l(l+1)\hbar^2}{2mr^2}R(r) & r > r_W \end{cases} \tag{2.33}$$

Since only the bound states inside this spherical well are relevant, the states where $E < 0$ are taken into account. Furthermore, the equations and the derivatives thereof should result in equal values for $r \le r_w$, $r \ge r_w$, and $r = r_w$. All states where $l \ne 0$ are discarded. With these conditions, an expression for the discrete energy levels within this finite spherical quantum well can be obtained.

$$E_n = \frac{\hbar^2}{2mr_w^2}z_n^2 - V_0. \tag{2.34}$$

Here z_n is the nth solution for z in the transcendental equation $-\cot z = \sqrt{(z_0/z)^2 - 1}$, where $z_0 \equiv \frac{\sqrt{2mV_0}}{\hbar}r_w$. It should also be noted that there are no solutions if $z < z_0$. This is due to the fact that for bound energies $E < V_0$.
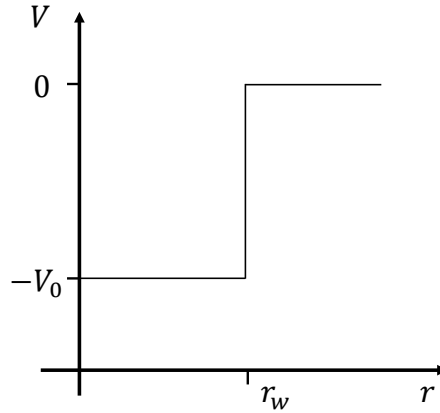
Figure 2.5: A schematic depiction of a potential well with depth $-V_0$ and radius r_w.

2.5.2 Quantum confinement

The behavior of a particle trapped inside a quantum well is modeled, and an expression for the bound energy levels inside the well is given in the previous section. The same model can be used to describe the charge carrier confining properties of the quantum dots. Prerequisite to this description, one needs to grasp the concept of the "de Broglie" wavelength, semiconductor bandgaps, and heterogeneity of the quantum dots first.

As opposed to semiconductor bulk material, small semiconductor crystals (i.e. QDs) subceed the typical de Broglie wavelength for electrons:

$$\lambda_{de\ Broglie} = \frac{h}{\sqrt{2\pi m \kappa_B T}}, \tag{2.35}$$

in size. $\lambda_{de\ Broglie}$ is 4.3 nm for an electron at $T = 300\,\text{K}$ or 0.025 eV. Therefore, the QDs are regarded as quantum structures in which charge carriers are trapped. For these structures, discrete energy levels and wavefunctions must be concerned.

The core-shell structure QDs used in our experiments consists of two semiconductor materials. Semiconductors are defined by having a band gap which, at room temperature, is small enough for photons from the visible region of the spectrum ($400 - 700\,\text{nm}$) to overcome and promote an electron into the conduction band [47]. This condition gives a maximum band gap energy for semiconductors by calculating the energy of a photon with a wavelength of 400 nm using
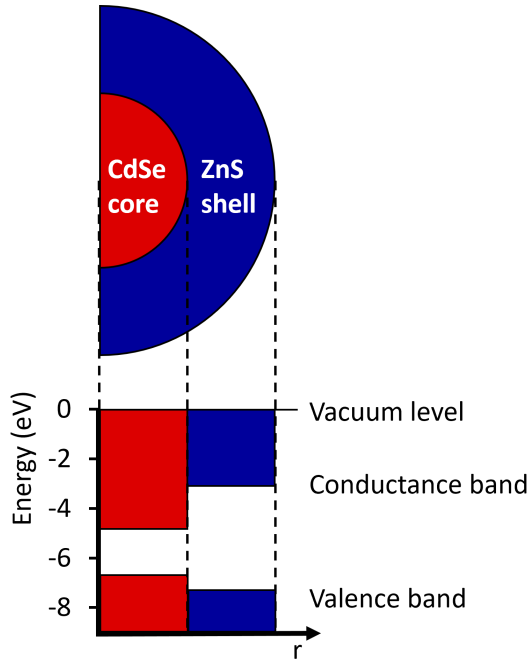
Figure 2.6: The energy landscape of CdSe/ZnS core-shell quantum dots. The illustration is inspired by [46]

$E = \frac{hc}{\lambda}$. From this, it is realized that the band gap of a semiconductor should be no larger than $E_{max} \approx 3.2\,\text{eV}$. Upon excitation of an electron from the valence band into the conduction band, a hole is created in the valence band. A hole is defined as a quasi-particle similar to an electron and possessing a slightly different effective mass and an opposite charge.

Finally, it is informative to explain the heterogeneity of the core-shell quantum dots. The quantum dots used in the experiments described in chapter 5 consist of a CdSe core and a ZnS shell, hence, creating a heterostructure. In heterostructure quantum dots, the charge carrier is trapped by the relative potential landscape of both materials. According to Anderson's rule [48], i.e. the electron affinity rule, the vacuum levels of two semiconductors on either side of the heterojunction are aligned at the same energy. The heterojunction is formed where the CdSe core and the ZnS shell in a CdSe/ZnS core-shell structure meet. A schematic overview of the energy levels of a CdSe/ZnS core-shell quantum dot is given in figure 2.6.

So far, some basic quantum mechanics has been provided to lay the foundation for understanding the photoluminescence property of the QDs. It is this PL

property, discussed in the next section, and its perturbations we use as a diagnostic technique for surface charge measurement later (see chapter 5).

2.5.3 Photoluminescence

Photoluminescence (PL) pertains to the spontaneous emission from quantum dots after the absorption of photons. The absorption of a photon results in the excitation of an electron in the semiconductor quantum dot and, subsequently, the formation of an electron-hole pair (i.e. charge carriers). After relaxation, i.e. non-radiative energy loss of charge carriers towards the band-gap minimum, radiative recombination occurs. This recombination is marked by the emission of a photon with an energy lower than that of an excitation photon, due to the relaxation stage. Generally, the PL process undergoes three stages:

1. **Excitation**: The absorption of a photon with an energy higher than the QD bandgap energy ($E_{ph} > E_{bg}$). In this case, the quantum-well structure is excited with some excess energy, i.e. non-resonant excitation. This is the typical situation used in most PL experiments since their excitation photon can be distinguished from the emission photon using spectrometry. Resulting from the excitation of an electron from the valence band to the conduction band is a permanent dipole moment that can interact with external electric fields.

2. **Relaxation**: The charge carriers descend to their minimum energy levels within the conduction and valence band of the QD after the excitation stage. Therefore, electron-hole pairs separately undergo energy and momentum relaxation towards the band-gap minimum. Typical relaxation mechanisms are Coulomb scattering and interactions with phonons. Characteristic timescales for relaxation are hundreds of picoseconds.

3. **Recombination**: The recombination of the electron-hole pair and emission of a photon. Due to charge carrier relaxation, the emitted photon has a lower energy than that of the excitation photon. Furthermore, the lowest possible energy levels of the charge carriers in the QD determine the PL photon energy (and their wavelength) since the relaxation process occurs before recombination within a much faster timescale.

The PL process with its three stages is schematically presented in figure 2.7.

The energy of the emitted photon is equal to the energy that is released when the electron falls back from its excited state to the equilibrium state, a process
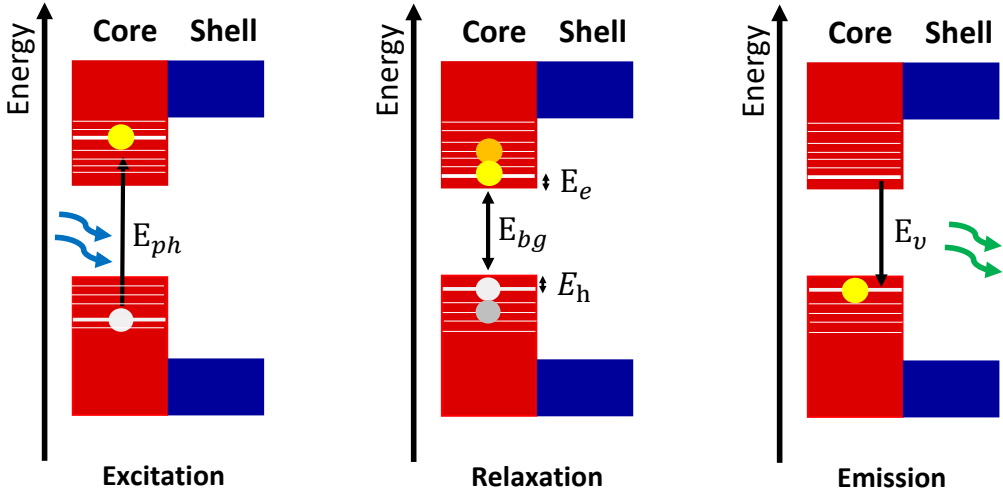
Figure 2.7: Photoluminescence process occurring in three stages from left to right: excitation, relaxation, and emission.

also called radiative recombination. The energy of the emitted photon (E_v) is equal to the sum of the band gap energy (E_{bg}) and the energy levels of the charge carriers($E_{electron}$ and E_{hole}):

$$E_v = E_{bg} + E_{electron} + E_{hole}. \tag{2.36}$$

The distribution function of emitted photons by a single QD is often described by a Lorentzian function. The resulting Lorentzian distribution function is determined by the distribution of electrons in the Fermi state of the conduction band before the radiative recombination process. This contributes to the broadening of the PL peak as observed spectrally resolved by a spectrometer. Another chief source of PL peak broadening is the temperature effect, which will be discussed briefly later. As in our experiments (chapter 5), a collection of QDs are deposited on a substrate and subsequently excited with a laser beam; collective effects such as size distribution of the QDs need to be into account when considering PL peak broadening.
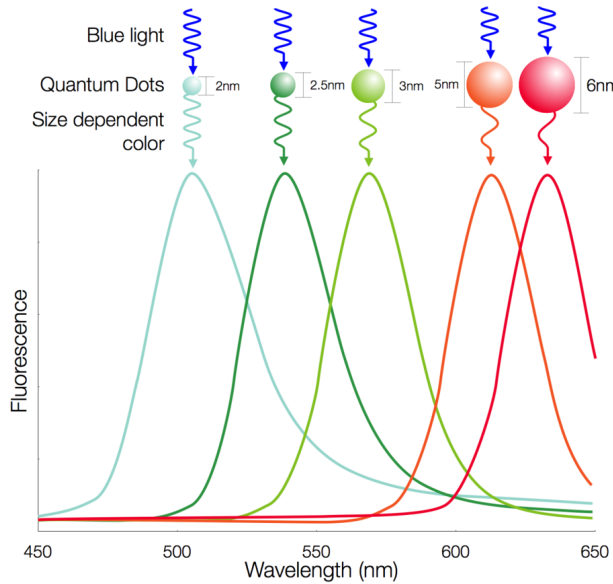
Figure 2.8: Photoluminescence wavelength as a function the QDs' size. The smallest QD represented here, 2 nm in diameter, emits light at 500 nm (green) while a larger, 6 nm in diameter, QD emits light at 630 nm (red). Figure courtesy of [49].

2.5.4 Quantum-confined Stark effect

As discussed earlier, QDs are capable of confining charge carriers, i.e. electrons and holes, within their spatial dimensions. This may lead to the observation of traditional atomic physical phenomena, such as the Stark effect. This Stark effect is observed for QDs exposed to an external electric field and is called the quantum-confined Stark effect (QCSE). This effect results from the shift of the electron and hole wavefunctions within the QD in opposite directions as a result of applying an electric field [18]. The electric field inside the QD pulls the electron and hole to opposite sides of the QD, thus leading to a reduction of the band gap energy and, therefore, to a redshift in the PL wavelength (see figure 2.9). Initially, the external electric field (F) within the QDs interacts with the permanent dipole. This permanent dipole is created by electron-hole wavefunction separation resulting from the excitation of the electrons. This interaction with the QDs' dipole induces a redshift linear with the electric field ($\Delta E_v \propto F$). Second, the electric field polarizes the QD, inducing a redshift that is quadratic with the electric field ($\Delta E_v \propto F^2$). For the CdSe QDs, only the quadratic part of the redshift with the electric field is observed [21, 50], i.e.:

$$\Delta E_{nu}(F) = -\mu F^2, \tag{2.37}$$

where μ is the component of the polarizability in the direction of the electric field. In order to determine the relationship between the redshift of the PL wavelength and the electric field to the QD, one needs to treat the electric field as a time-independent perturbation of the potential (equation 2.31) and solve the Schrödigner (equation 2.29). The perturbation potential is an additional term of $V_{Stark}(r) = -\mu F(r)^2$ when solving the Schrödigner equations for the electron and the hole and deriving the Eigen states with their perturbation energies. With establishing the result of the second-order perturbation of the electric field on the electron and hole as well as the band gap energies, the wavelength shift in the PL is expressed as [51]:

$$\Delta\lambda = 0.03\lambda^2 (hc)^{-1} (m_e{}^* + m_h{}^*) a^4 \left(\frac{2\pi eE}{h} \right)^2, \tag{2.38}$$

where e, h, a, $m_e{}^*$, $m_h{}^*$, and c indicate the elementary charge, Planck's constant, the QD core radius, the electron's effective mass, the hole's effective mass, and the speed of light, respectively.

2.5.5 Temperature effect

The quantum mechanical models explained so far have one common underlying assumption: the temperature of the QDs is zero Kelvin. In our experiments, however, the QDs were at room temperature and, possibly due to interactions with the plasma, even higher while also changing throughout the experiment. Basically, the temperature has two effects on the QDs that can be subsequently tracked by analysing their PL emission: a redshift of the PL wavelength and a reduction in the PL intensity.

The temperature-induced redshift in PL wavelength was already characterized by Varshni *et al.*[52]. The temperature dependence of the bandgap energy of a QD can be expressed as:

$$E_{bg}(T) = E_{bg,0} - \alpha \frac{T^2}{(T+\beta)}, \tag{2.39}$$

where $E_{bg,0}$ is the band gap energy at temperature $T = 0\,\mathrm{K}$, α is the temperature coefficient, and β is the Debye temperature (θ_D) of the material. For the case of CdSe QDs, these two constants are $\alpha = 4.1 \times 10^{-4}\ eV/K$ and $\beta = 181\,\mathrm{K}$ [53].
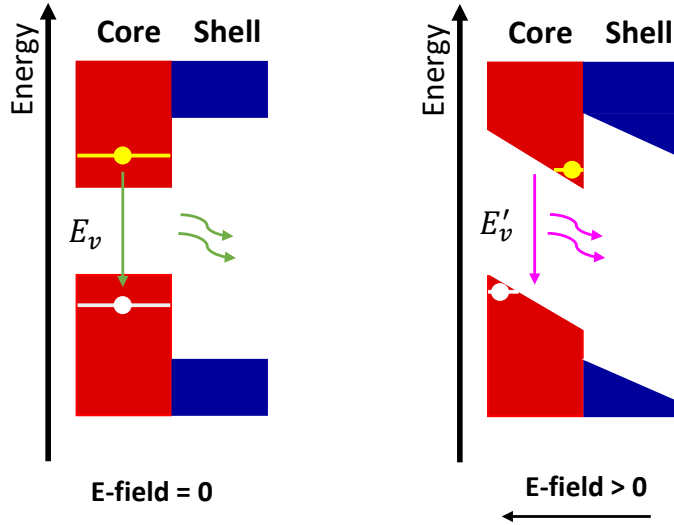
Figure 2.9: Schematic representation of the effect of an external electric field on the electron and hole energy states in the conduction and valence band. On the right, the electron and hole wavefunctions are pulled towards opposites side, resulting in a redshift of the photoluminescence and thus: $(E_v > E_v^{'})$

The reason for the shrinkage of the band gap energy due to the temperature increase of The QD is two-fold: Lattice dilation and carrier-phonon interaction. The former, lattice dilation, pertains to the thermal expansion of the lattice structure of the QD. An expanded and larger QD leads to lower bound state energy and, therefore, a redshift in the PL wavelength. The latter contributing factor to the temperature-induced redshift of the PL wavelength is carrier-phonon interaction. Phonons are quantized units of lattice vibrations, which exist in acoustic and optical forms. The phonon-induced redshift is caused by the scattering of electron-hole pairs with the longitudinal optical phonons in the QD lattice structure [54, 55]. This energy shift scales linearly with the temperature for temperatures higher than the Debye temperature of the QD ($T \gg \theta_D$). In other words, $E_{bg}(T) \propto T$, which is the case for the experiments of chapter 5. Here the debye temperature (θ_D) of the QD pertains to the highest temperature of the QD lattice that can be achieved due to a single normal vibrational (phonon).

Concomitant with a redshift in the PL peak, a reduction in the PL intensity is induced as the temperature of the QDs is increased. The PL intensity decrease is mainly due to the activation of non-radiative processes, e.g. the Augur effect

and non-radiative recombination, in the QD due to phonon interactions with the electron-hole pair. This intensity reduction, as well as the redshift, are discussed thoroughly in chapter 5.

2.6 Surface charge

As explained earlier in this chapter, a negative charge is deposited on an electrically floating object upon immersion in a low-pressure plasma. In the specific case of chapter 5, the surface charge is indirectly detected by the QDs deposited on the surface of that substrate. Therefore, the plasma surface charging phenomenon is essential to the subject of this chapter. In this phenomenon, the electrons reside on the surface due to their higher mobility and temperature compared to the situation for ions. Encapsulating the surface is the plasma sheath that must be characterized for investigating the surface charge. According to Gauss's law, the surface charge density (σ), i.e. the surface density of electrons, in this case, is expressed as:

$$\sigma = E_{sheath}\varepsilon_0. \tag{2.40}$$

Here E_{sheath} is the average normal component of the sheath electric field at the surface. The electric field in the sheath will be estimated by measuring the sheath thickness, and the potential drop across the sheath is determined using equation 2.12. For this purpose, the necessary plasma parameters, such as the electron temperature (T_e) and the amplitude of RF oscillations (V_1), are measured using a commercial Langmuir probe and an oscilloscope, respectively. The sheath thickness is estimated using equation 2.13, and the thickness values are subsequently cross-checked with measurements performed by a CCD camera. Having estimated the potential drop and the sheath thickness, the electric field across the sheath ($E = d\phi/dx$) is expressed as [24]:

$$E_{sheath} = \frac{4}{3}\frac{V_s}{s}\left(\frac{x}{s}\right)^{1/3}. \tag{2.41}$$

Here, x is the distance from the boundary between the sheath and the plasma bulk. Using this equation at the position of the floating surface ($x = s$), the electric field yields:

$$E_{sheath} = \frac{4}{3}\frac{V_s}{s}. \tag{2.42}$$
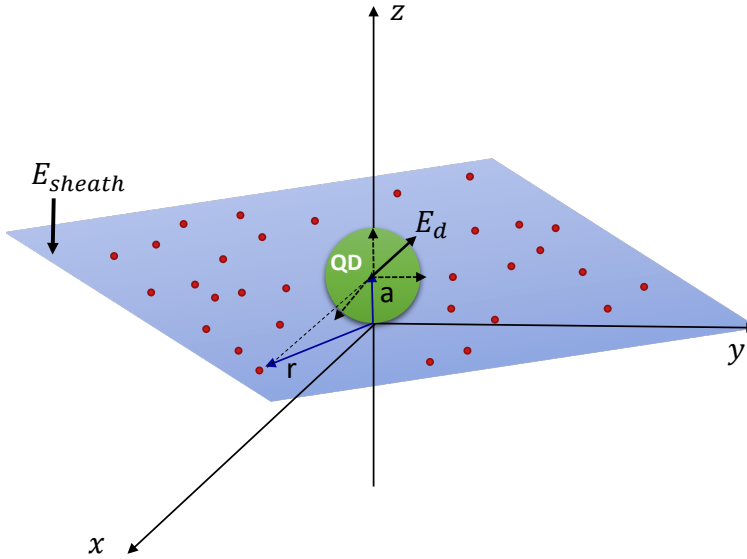
Figure 2.10: Schematic representation of the discrete charge model: here, one random configuration of electrons (red circles) is shown, and the subsequent electric field originating from all the electrons near one QD is calculated (E_d).

As concluded in chapter 5, the redshift observed in the spectral PL peak positions of the surface deposited QDs is associated with the excess electrons residing on the surface. The effect of the electric fields originating from these surface electrons on QDs, therefore, must be investigated. The following surface charge model is devised to investigate the microscopic effect of surface electrons.

2.6.1 Discrete charge model

The electric field-induced redshift in the PL peak position of the surface deposited QDs can, in principle, result from two electric field components. The plasma sheath electric field (E_{sheath}) (the macroscopic electric field) and the electric field originating from the adjacent surface electrons near the QDs (the microscopic electric field). While the former is the result of the plasma sheath formation around the plasma-immersed substrate, the latter is due to the electric field fluctuations by the surface electrons. The connected electric field fluctuations are due to the redistribution of electrons on the surface.

The discrete charge model allows for the calculation of the local electric field at the position of a QD on the surface for a given surface charge density (σ). This surface charge density is calculated by estimating the average normal component

of the electric field (E_{sheath}) using equation 2.40. Subsequently, the statistics of the local electric field resulting from the redistributing surface charge are calculated by taking into account multiple random configurations of electrons on the surface at constant σ and evaluating the electric field at the position of a single point-like QD (see figure 2.10). In these calculations, typically, a few million random electron configurations are evaluated to calculate the statistics of the local electric field - with each configuration consisting of thousands of quasi-static electrons. As the Stark shift scales quadratically with the electric field (equation 2.38), the root-mean-square of all the electric fields associated with the multiple configurations needs to be calculated. This electric field is called the microscopic electric field and is typically one order of magnitude stronger than the macroscopic (sheath) electric field.

Chapter 3

Diagnostics

Abstract

Two main diagnostic methods are further developed and applied to gather precise data on charged particle dynamics in plasma afterglows. The combined diagnostic techniques of microwave cavity resonance spectroscopy and laser-induced photodetachment are used to measure electron and negatively charged species densities. The fundamentals of these two techniques are discussed in this chapter prior to their application later in this thesis.

3.1 Introduction

Two pre-existing diagnostic techniques are further developed and used throughout this thesis for unraveling the dynamics of electrons, anions, and charged dust particles in plasmas and their afterglows. Primarily, microwave cavity resonance spectroscopy is used to detect and measure the temporally resolved density of free electrons in a plasma. In combination with this technique, laser-induced photodetachment enables the measurement of negatively charged species densities temporally resolved. These two techniques are specifically applied to investigate the temporal afterglows of electronegative, reactive, and dusty plasmas in chapter 6 and 7.

This chapter is organized as follows: first, the general theory and formulae required to understand microwave cavity resonance spectroscopy (MCRS) are discussed in section 3.2.1. Furthermore, it is explained how to implement this technique to detect and measure the electron density in plasma in section 3.2.2. Subsequently, the general idea of laser-induced photodetachment and the requirements for its application on electronegative (oxygen) plasmas and reactive (argon-acetylene) plasmas are elaborated on in section 3.3.

3.2 Microwave Cavity Resonance Spectroscopy

The electron density is one of the key parameters required to characterize and understand the dynamics of the different types of plasmas formed and investigated in our research. It is, therefore, essential to measure the electron density during different stages of plasma formation, from initiation to steady-state operation and into the afterglow phase. Time-resolved electron density measurements enable, for instance, the unraveling of dust particle formation dynamics in a reactive plasma. Specifically, our research focuses on the afterglow phase and the governing decay of the electron density. Hence, this state-of-the-art, non-invasive, high-resolution, and fast technique is adopted and used for the detection and measurement of electrons and their density.

Conventional probe-based techniques for electron density measurements are invasive to the plasma under investigation and, therefore, not useful for our situation. Moreover, the contamination associated with dusty plasmas and the interaction of negative ions with the probe's tip creates additional complexity and obstacles in using them. Microwave-based diagnostic methods for electron density measurements, interferometry, and the cavity resonance technique, are therefore devised as alternatives. Microwave cavity resonance spectroscopy (MCRS) has

the advantage of a relatively lower detection limit compared to the interferometry technique. In the second research line of this thesis, MCRS is used for measuring the electron density in the temporal afterglows of electronegative and reactive plasmas.

3.2.1 General formulae

Microwave cavity resonance spectroscopy (MCRS) utilizes standing waves - for this work in the GHz range - that are excited within a metal cavity. Each standing wave is excited at a specific frequency (i.e. the resonance frequency) determined by the geometry and the permittivity of the medium inside the cavity. During the application of MCRS, the resonance frequency of a specific mode is precisely tracked as electrons are introduced to the cavity as the discharge initiates or their density changes due to other events. The emergence of free electrons and, therefore, the change in permittivity of the medium inside the cavity results in a shift of the resonance frequency. This shift is then indirectly related to the density of free electrons.

In a cylindrical cavity, the electric field of a standing mode is expressed as [56]:

$$\vec{E}\left(\vec{r},t\right) = \vec{E_0}(x,y)\exp\left(\pm ikz - i\Omega t\right), \tag{3.1}$$

where the spatial configuration of the electric field $\vec{E_0}(x,y)$ and the wave number k are determined by the geometry of the cavity. Ω is a complex number consisting of a real part ω, that expresses the oscillations, and an imaginary part γ, that expresses the damping of the standing wave. The dispersion relation relates the wave number k and the frequency Ω as:

$$\Omega^2 = k^2\frac{c^2}{n^2} = k^2\frac{c^2}{\mu_r\varepsilon_r}, \tag{3.2}$$

where n, μ_r, and ε_r indicate the refractive index, relative permeability, and relative permittivity of the medium inside the cavity, while c is the speed of light in vacuum. The relative permittivity of a cavity containing a plasma depends on the oscillation frequency ω as:

$$\varepsilon_r = 1 + i\frac{1}{Q_0} + i\frac{\omega_p^2}{\omega(v-i\omega)} = 1 + i\frac{1}{Q_0} - \frac{\omega_p^2}{\omega^2+v^2} + i\frac{\omega_p^2}{\omega^2+v^2}\frac{v}{\omega}. \tag{3.3}$$

In this equation, two loss terms are included: Ohmic losses and loss due to collisions. The former pertains to the non-idealities of the cavity and is included

as the $i\frac{1}{Q_0}$ term. The latter pertains to the dissipation in the plasma due to electron collisions with other particles. The frequency thereof is expressed as v. The (electron) plasma frequency, related to the plasma density n_e, is given by:

$$\omega_p^2 = \frac{n_e e^2}{m\varepsilon_0}.$$
(3.4)

Substituting equation 3.3 in the dispersion relation (equation 3.4) and assuming the deviation of ε_r from the ideal case is small (i.e. $Q_0 \gg 1$, $\frac{\omega_p}{(\omega^2 + v^2)^{1/2}} \ll 1$), the Ω can be linearized as:

$$\Omega = \underbrace{\omega_0 + \frac{\omega_0 \omega_p^2}{2(\omega^2 + v^2)}}_{\omega} - i\underbrace{\frac{\omega_0}{2}\left(\frac{1}{Q_0} + \frac{\omega_p^2 v}{\omega(\omega^2 + v^2)}\right)}_{\gamma}.$$
(3.5)

Here ω_0 and ω are the resonance frequencies without and with plasma, respectively, and γ is the attenuation constant. Therefore, the shift of the resonance frequency $\Delta\omega$ due to the formation of plasma is:

$$\Delta\omega = \omega - \omega_0 = \frac{1}{2}\omega\frac{\omega_p^2}{\omega_p^2 + v^2}.$$
(3.6)

The attenuation constant is written as:

$$\gamma = \frac{\omega_0}{2Q},$$
(3.7)

where Q is called the quality factor and accounts for the average energy dissipation in the cavity:

$$\frac{1}{Q} = \frac{1}{Q_0} + \frac{\omega_p^2}{\omega_p^2 + v^2}\frac{v}{\omega_0}.$$
(3.8)

Assuming a low-pressure plasma, the collision frequency of the dissipation most often is negligible when compared to the resonance frequency, i.e. $\omega^2 \gg v^2$. Hence, the term v^2 can be neglected in equations 3.6 and 3.8 [57]. The quality factor Q is essentially a measure for the response time of the cavity:

$$\tau = \frac{2Q}{\omega_0}.$$
(3.9)

Here, τ is the fundamental time resolution of the measurement. The quality factor of the cavity can be related to the FWHM of the (measured) resonant peak Γ as:
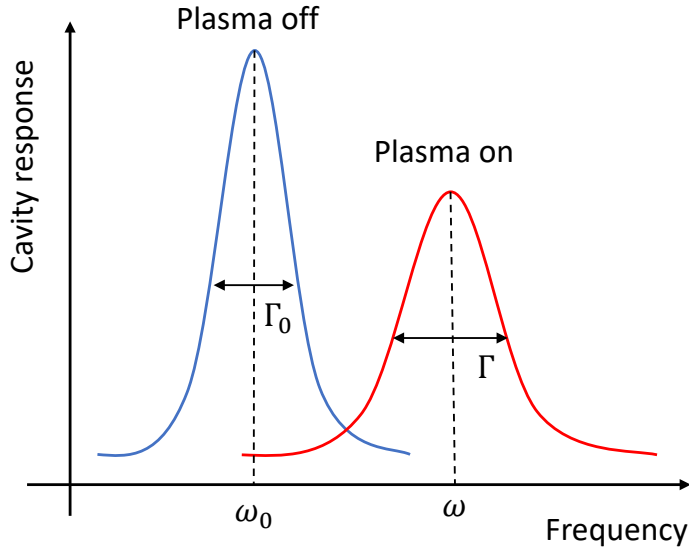
Figure 3.1: Schematic representation of the idea of MCRS: the resonance peak at frequency ω_0 shifts towards ω when plasma is switched on.

$$Q = \frac{\omega}{\Gamma}. \tag{3.10}$$

A schematic representation of the main idea behind the MCRS technique is provided in figure 3.1. As illustrated in the figure, upon initiation of the discharge and introduction of free electrons inside the cavity, the resonance frequency undergoes a shift towards higher frequencies, which can be monitored temporally resolved. Concomitant with a shift in the resonance frequency of a specific mode is the broadening of the peak. This broadening is caused by the dissipation of electromagnetic radiation by free electrons, which leads to a drop in the quality factor of the cavity. From this broadening, extra information, such as information about the electron temperature or the electron collision frequency, can be obtained.

The temporal evolution of the electron density can be related to the temporal evolution of the resonance frequency. This relation can be derived from equations 3.4 and 3.6 and yields:

$$\bar{n}_e(t) = \frac{8\pi^2 m_e \varepsilon_0 f^2(t)}{e^2} \frac{f(t) - f_0}{f_0}, \tag{3.11}$$

noting that $\omega = 2\pi f$. Here f_0 is the initial resonance frequency before any change of the electron density, and $f(t)$ is the resonance frequency during any particular incident resulting in a change in free electron density.

The electron density associated with a change in the resonance frequency of a particular microwave mode ($\bar{n}_e$) is microwave-electric-field-weighted and averaged over the cavity volume. Taking into account both the spatial distribution of the free electrons over the cavity volume $n_e(\vec{x})$ and the local value of the electric-field component $E(\vec{x})$ of the applied microwave resonant mode, the cavity-averaged and microwave-electric-field-weighted electron density at a certain moment in time is then given by:

$$\bar{n}_e = \frac{\int_{cavity} n_e(\vec{x}) E^2(\vec{x}) \, d^3\vec{x}}{\int_{cavity} E^2(\vec{x}) \, d^3\vec{x}}. \tag{3.12}$$

This also means that electrons at different positions in the cavity are probed to different extents. In the research performed in chapter 6 and 7, the fundamental resonant mode, i.e. TM_{010}, of a cylindrical cavity is used. Therefore, the mode structure and spatial distribution of the microwave electric field of this microwave mode are necessary to be known.

For this, an ideal cylindrical cavity is considered with radius R and height h, and with a conductive wall. Furthermore, the cavity is filled with a lossless dielectric medium with permittivity ε and permeability μ. Depending on the boundary condition on the walls, two different solutions of the electromagnetic fields, i.e. two different types of modes, are allowed. The transverse magnetic (TM) mode is the result of the first set of boundary conditions ($H_z = 0$ everywhere and $E_z|_{wall} = 0$ on the walls). The second set of boundary conditions ($E_z = 0$ everywhere and $\frac{\partial H_z}{\partial n}|_{wall} = 0$) results in transverse electric (TE) mode solutions. In these boundary conditions, H_z and E_z represent the magnetic induction and electric field in the z direction. At the same time, $|_{wall}$ and n denote the component parallel to the wall and the unit normal to the wall, respectively. Since in our research only one resonant mode (TM_{010}) is used, only the electric field ($\overrightarrow{E}(r, \theta, z)$) for this particular mode is provided:

$$E_z(r, \theta, z) = E_0 J_0\left(\frac{2.405r}{R}\right) e^{iwt}. \tag{3.13}$$

Here E_0, and J_0 are the electric field's amplitude and the zero-order Bessel function, respectively. Other components of the electric field, namely E_r and E_θ, are zero for this TM_{010} mode.

The COMSOL® platform is used to simulate the mode structure in the measurement cavity. First, the model calculates the excitation frequencies of all the
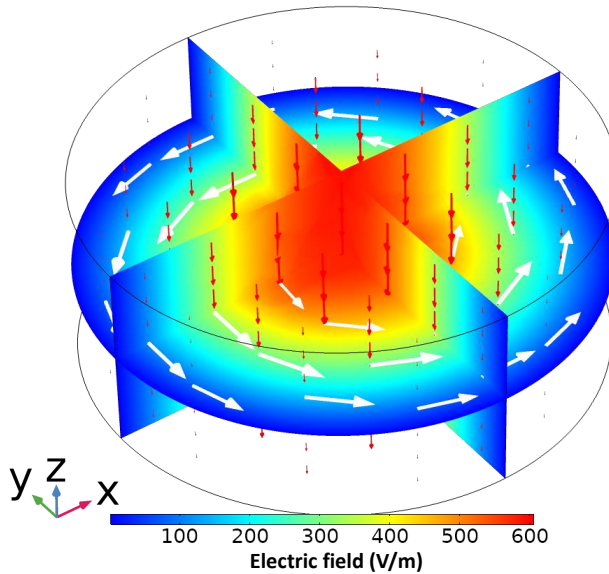
Figure 3.2: Spatial distribution of the resonant microwave field associated with the TM_{010} resonant mode in the cavity: electric and magnetic field directions are represented by red and white arrows, respectively. The simulation is performed using COMSOL®.

resonant modes that can be excited (within the relevant frequency range) inside a cylindrical cavity. The frequency of the fundamental resonant mode TM_{010} is obtained in the experiments and subsequently selected in the model. Afterward, the model simulates the microwave electric field distribution of the selected mode. Figure 3.2 shows the simulated electric field distribution $E(x,y,z)$ of the TM_{010} mode in the measurement cavity. This microwave electric field distribution, which only has an axial component that has a radial dependence, has been used to obtain the electron density for each subsequent experiment. As seen in Figure 3.2, this mode is most sensitive on the axis of the cavity. A detailed description of the measurement cavity and the dimensions thereof is provided in chapter 4.

3.2.2 Implementation

In order to obtain a resonant peak in practice, the microwave signal is applied to one antenna that simultaneously transmits the microwaves into the cavity and scans the reflected response of the cavity over a subsequent series of frequen-
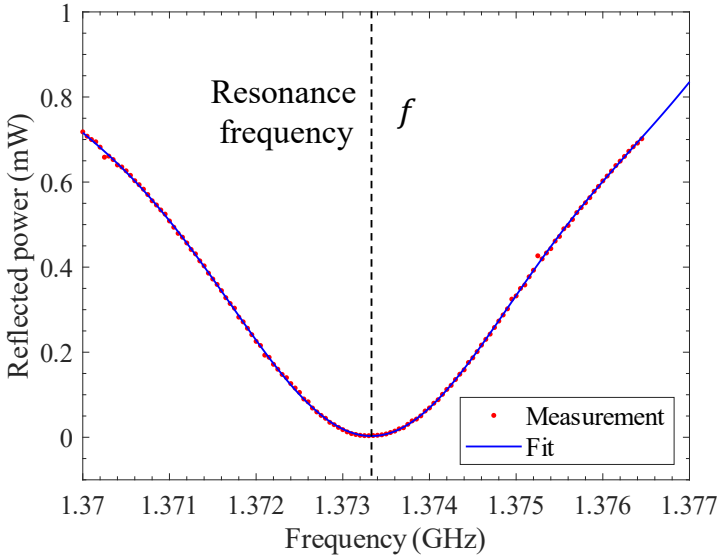
Figure 3.3: Cavity response around TM_{010} resonance (red dots) and the Fourier fit (blue curve) at an arbitrary time. The frequency at which the reflection is minimum indicates the resonance frequency.

cies. The response of the cavity is converted to a proportional DC voltage and collected by software developed in-house. To construct the spectral response of the TM_{010} mode, a series of frequencies around the resonance frequency of this mode is transmitted to the cavity, and the cavity response to each frequency is subsequently recorded. Figure 3.3 shows the constructed TM_{010} peak for the used measurement cavity. The cavity's response (in mW) is stored as a function of microwave frequency, and the exact resonance frequency is obtained by fitting a Fourier function to the peak in the frequency domain. The used Fourier fitting function is formulated as follows:

$$V_{fit}(f) = a_0 + \sum_{n=1}^{4} [a_n \cos(nwf) + b_n \sin(nwf)], \quad (3.14)$$

where a_0, a_n, b_n, and w were fitting parameters. For improving the accuracy of the determination of the resonance frequency as well as for accounting for possible peak asymmetries, four harmonics of the Fourier series are used. As illustrated in Figure 3.3, the frequency at which the fit was minimum indicated the resonance frequency ($f = 1.3733$ GHz). Since electron density measurements require only the resonance frequency from raw data, a Fourier fit function was

deemed suitable for the measurements presented in this contribution. However, a more sophisticated Lorentzian fit capable of delivering temporally resolved values for the quality factor Q (as well as for the resonance frequency) could have been used [57], had the measurements been performed in a collisional plasma regime.

The final step in MCRS measurement is obtaining the electron density temporally resolved. Multiple MCRS measurements have to be performed consecutively in a cycle and in a highly reproducible fashion for experiments requiring a high temporal resolution for electron density determination. Therefore, plasma formation, or any event that causes the change in the electron density (e.g. photodetachment), needs to be performed in a pulsed fashion. To perform a temporally resolved electron density measurement, the microwave source needs to be at a specific frequency and kept at this frequency for the entire duration of a given set of plasma pulses. At the same time, the cavity's response is recorded temporally resolved before and after the plasma ignition or photodetachment event. For each set value of the microwave frequency, the delay pattern is repeated (typically 30 times in this work) for averaging purposes to enhance the signal-to-noise ratio. The microwave source is then set to the next frequency value just before the next series of plasma pulses. These measurements probe a resonant peak at 65 steps of 100 kHz located in the frequency domain closely around the resonant frequency to obtain sufficient accuracy. Figure 3.4 exemplarily shows an MCRS measurement of a pulsed plasma that operates for 11 ms. Before the plasma was switched on, the resonance frequency was $f_0 = 1.3678\,\mathrm{GHz}$. Upon ignition of the plasma at $t = 0$, the resonance frequency increases, which is translated to the displayed electron density via equation 3.11.

The MCRS technique detects and measures any changes in electron density that occurs inside the cavity and within the sensitive region of the excited mode. Therefore, any phenomenon that involves a change in electron density, e.g. laser-induced photodetachment or particle growth, can be investigated by the MCRS technique as well. The detection limit for determination of the electron density in our MCRS measurements, in chapter 6 and 7, was 10^{12} (m^{-3}). The ultimate time resolution of the MCRS measurements strictly depends on the quality factor of the cavity (see equation 3.9 and 3.10), which in turn depends on the physical conditions of the specific cavity used in the experiments. The time resolution was $\tau \approx 50\,\mathrm{ns}$ and $\approx 92\,\mathrm{ns}$ for experiments in chapter 6 and 7, respectively.
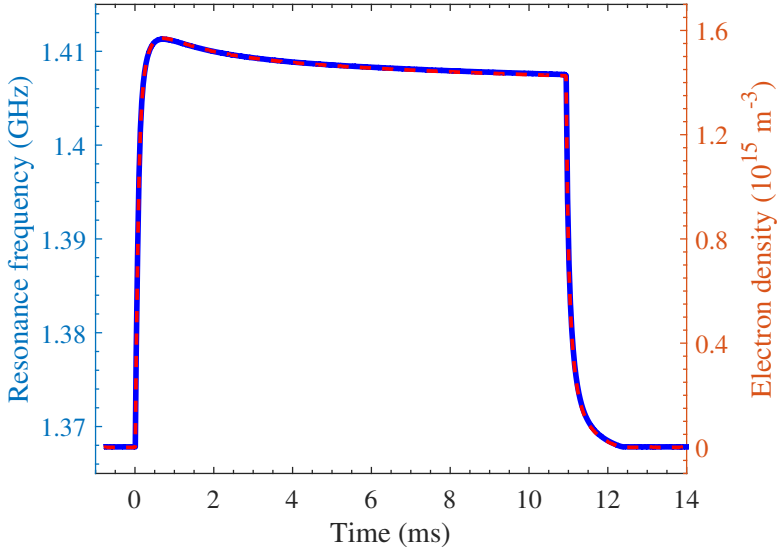
Figure 3.4: Example of a temporally resolved MCRS measurement for a pulsed plasma: at $t = 0$ the plasma is ignited, and at $t = 11$ ms, it is switched off. The resonance frequency (left axis, blue curve) and electron density (right axis, red dashed line) are plotted as a function of time.

3.3 Laser-induced photodetachment

Laser-induced Photodetachment (LIP) is an indirect approach to detect negatively charged species. Focusing for now on negative ions (the situation for negatively charged dust particles is similar), in this technique, the negative ions are converted into electron-neutral pairs upon the absorption of laser photons with sufficient energy:

$$X^- + h\nu \rightarrow X + e^-. \tag{3.15}$$

Here X^-, $h\nu$, and $X + e^-$ signify a negative species, a laser beam photon, and a photodetached neutral-electron pair, respectively. This process occurs provided that the photon energy $h\nu$ exceeds the electron's binding energy, i.e. the electron affinity of X. MCRS can subsequently detect the overall impact of the photodetachment event, i.e. the electron release upon photodetachment of negative ions leads to a sudden local surge of the electron density in the plasma, which in turn is observed directly as a change in resonance frequency. Figure 3.5 represents the exemplary incident of photodetachment upon radial laser irradiation of an (elec-
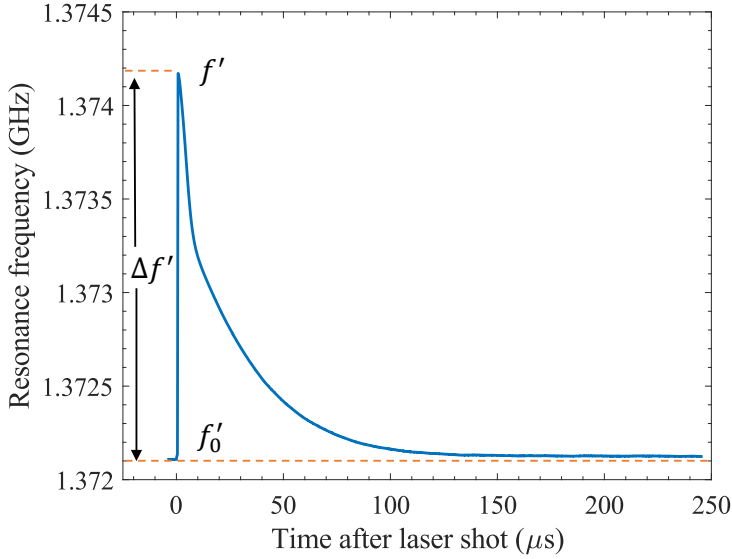
Figure 3.5: Exemplary measurement of photodetachment incident as observed with MCRS: a change in resonance frequency ($\Delta f'$) due to an electron density surge caused by the release of photodetached electrons.

tronegative oxygen) plasma and the resulting shift in resonance frequency during and after this event.

As discussed, equation 3.11 can relate the additional resonance frequency shift due to the sudden appearance of photodetached electrons to a change in electron density (Δn_e^{sat}). Assuming that the laser pulse energy is sufficient to convert all the negative ions in the laser beam path, i.e. operation in the saturation regime, a radially line-averaged negative ion density n_- is obtained by multiplying Δn_e^{sat} with the ratio of the cavity to the laser beam volume, weighted with $E^2(\vec{x})$ of the used microwave mode:

$$n_- = \Delta n_e^{sat} \frac{\int_{cavity} E^2(\vec{x}) \, d^3\vec{x}}{S \int_{-R}^{R} E^2(r) \, dr}. \tag{3.16}$$

Here R is the radius of the cavity ($2R$ is the path taken by the laser beam through the cavity), and S is the geometric cross-section of the laser beam. Since the cavity is cylindrical, the electric field of the TM$_{010}$ has an axial field component given by the Bessel function $J_0(r)$ with only a radial dependence. Furthermore, the integrals in equation 3.12 have been calculated using the electric fields

(see Figure 3.2) associated with the geometrical configuration of the cavity used in the experiments.

Suppose the saturation regime is not achieved, meaning that the laser beam can only partially convert the negative ions into neutral-electron pairs along its path, the photodetached electron density scales exponentially with the laser pulse energy. In this case, the fraction between the photodetached electron density using a specific laser pulse energy (Δn_e) and the photodetached electron density in the saturation regime (Δn_e^{sat}) is then given by:

$$\alpha = \frac{\Delta n_e}{\Delta n_e^{sat}} = 1 - \exp\left(-\frac{\sigma_{det}}{h\nu}\frac{E_{laser}}{S}\right). \qquad (3.17)$$

Here, σ_{det} and E_{laser} indicate the photodetachment cross section of a specific anion and the laser pulse energy, respectively.

In principle, it is possible to distinguish the contribution of each negative ion species to the total negative ion density by carefully choosing the laser wavelength. In the experiments presented in chapter 6, for instance, we used the fundamental and second harmonic mode of an Nd:YAG laser to probe the densities of O^-, O_2^- and O_3^- anions and that of O_2^- alone. In the experiments presented in chapter 7, the total negative species density (consisting of anions and nanoparticles) was measured using the fourth-harmonic ultraviolet mode at 266 nm.

Chapter 4

Experimental setups

Abstract

This chapter provides a detailed description of the experimental setups and methodology used throughout this thesis. A basic vacuum vessel is used to ignite and form radio-frequency capacitively coupled low-pressure (RF-CCP) plasmas for conducting the two research lines. In the first research line, quantum dots are exposed to the plasma formed in argon gas at a fixed pressure. Then, a laser is directed to excite the quantum dots locally, and their photoluminescence spectrum is subsequently observed and analyzed. In the second research line, plasmas are formed in oxygen and argon-acetylene feedstock gases at various pressures. In order to study the afterglow phase of these electronegative, reactive, and dusty plasmas, a plasma on-off scheme is deployed. For the characterization of these plasmas, microwave cavity resonance spectroscopy (MCRS) is performed using a set of equipment, including a microwave generator and a transient recorder. Laser-induced photodetachment (LIP) is performed using a high-power Nd:YAG pulsed laser operating in its fundamental mode and in its second, and fourth harmonics.

4.1   Introduction

Two different setups have been designed and used for the experiments for the two research lines conducted in this thesis:

- **Setup I** was deployed to expose quantum dots to plasma and to investigate the effect of surface charging on their photoluminescence (PL) spectrum (chapter 5).

- **Setup II** was deployed to investigate the afterglow phase of pulsed electronegative (oxygen) and reactive (argon-acetylene) plasmas (chapter 6 and chapter 7, respectively).

Both setups are very similar in terms of using the same vacuum chamber, pumping system, radiofrequency (RF) voltage generator, mass flow controllers for feeding different gases, and pressure control valves. The discharge in both setups is asymmetric, pulsed, and capacitively coupled to the power source with an automatic matchbox. Since all the used plasmas are capacitive discharges in low pressure, the basic principle of capacitively coupled plasma generation is briefly discussed in section 4.2 prior to the description of the setups. As both setups are similar to each other in many terms, we first provide a general description, including the specification of the equipment and devices used in both setups (section 4.3). Next, we elaborate on the optical setup (used in the setup I) that is designed for the excitation of the quantum dots with a laser and collection of the photoluminescence thereof (section 4.4). Finally, we explain the technical aspects of the microwave cavity resonance spectroscopy and laser-induced photodetachment systems used in setup II (section 4.5).

4.2   Capacitively coupled plasma

In the setups used for both research lines in this thesis, the discharge was driven capacitively by a radio-frequency (RF) voltage. Therefore, a brief description of this discharge type and its generation is provided here. The conditions discussed in the previous chapter for electropositive (section 2.2) and electronegative (section 2.3) plasmas also apply to capacitive discharges. In general, a plasma discharge is generated and sustained by electron-impact ionization reactions.

The adverb "capacitively" pertains to the way in which this plasma configuration is similar to a capacitor. A low-pressure capacitively coupled plasma (CCP) typically consists of two parallel electrodes, usually of several tens of centimeters, separated by a distance of a few centimeters, and one of them being

biased by an RF power supply, typically operating at 13.56 MHz. In this case, the plasma is usually formed between the two plates. The RF power is mostly deposited into the kinetic energy of mobile electrons, which respond to the RF electric field oscillations. The power absorbed by the electrons leads to the heating of the electron population. The much heavier ions, however, respond only to time-averaged fields and do not directly gain energy from the RF field; therefore, ion heating by the RF field is negligible (since $\omega_{pi} \ll \omega_{RF}$). As a result, the electron cloud oscillates with the electric field through a background of positive ions. The positive space charge around the electrodes defines the sheath across which the positive ions are accelerated toward the electrodes. During each RF cycle, the sheath appears and collapses at each electrode so that quasi-neutrality within the plasma can be maintained.

From the outside, a symmetrical CCP can be seen to have a specific relationship between the current that flows and the voltage that appears across the plates by means of which it absorbs a measurable quantity of power. Therefore, an electrical circuit model, having equivalent current-voltage characteristics and dissipating the same power, can be devised. As can be seen in figure 4.1, a typical CCP RF discharge can be modeled as a load, with resistance R_D and reactance X_D, equivalent to the impedance of $Z_D = R_D + iX_D$. Here $X_D < 0$, since $X_D = -(\omega C)^{-1}$ in which $C > 0$ is the discharge capacitance and ω is the angular driving frequency. The power source supplies a complex voltage $\tilde{V}_T$ that is dissipated by a load of (usually) $R_T = 50 \, \Omega$. A voltage drop $\tilde{V}_{rf}$ is produced across the discharge as a current $\tilde{I}_{rf}$ is driven through the plasma. This voltage drop occurs in different components of the discharge, including the sheaths and the plasma bulk itself. Each component is modeled as a capacitor and must be included in the detailed model of the CCP plasma [23].

For optimal power coupling, the resistance of the source should be equal to the load resistance, and the reactance of the source and the load should be equal and opposite in sign [58], in other words, $Z_T = Z_L^*$ in which Z_L^* is the complex conjugate of the load impedance. Excluding the matching network in figure 4.1, the power source would be purely resistive, and hence, the power coupling would be far from optimal. A matching network is therefore installed between the source and the plasma. Generally, an L-type matching network consisting of a fixed inductance and a series of variable capacitors is suitable for CCPs. The parallel capacitor (with respect to the transmission line) and the tuning capacitor are variable and are shown as X_1 and X_3 in figure 4.1. The parallel capacitor (referred to as the load capacitor) is supposed to match the plasma resistance to the source resistance, and the tune capacitor tunes out the plasma reactance. For maximum power coupling, it can be shown [59]:
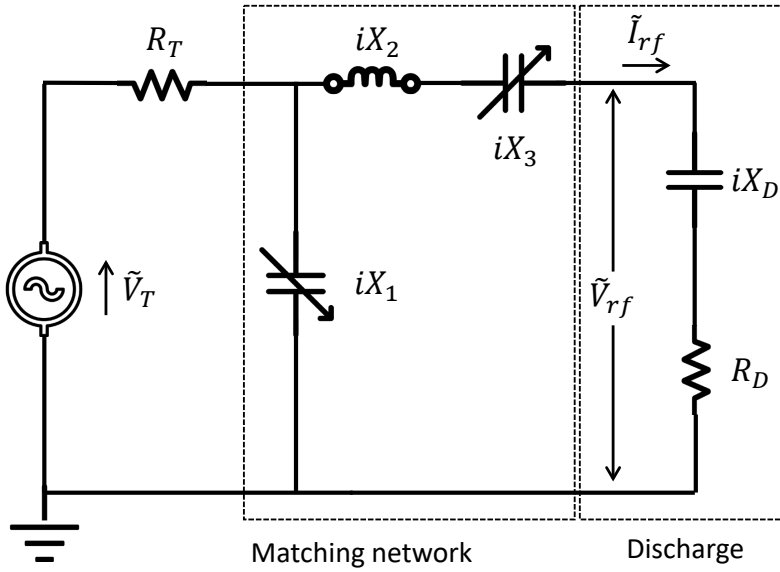
Figure 4.1: Electric circuit model for a capacitively coupled plasma reactor in-cluding the discharge (right) and the matching network (left). The discharge is matched to an AC source with resistance R_T by tuning the two capacitors (iX_1 and iX_3) in the matchbox.

$$X_1 = \pm R_T \sqrt{\frac{R_D}{R_T - R_D}}, \tag{4.1a}$$

$$X_3 = \pm \sqrt{R_D(R_T - R_D)} - (X_D + X_2). \tag{4.1b}$$

Here X_1, X_3, $X_D < 0$ since they represent capacitors whereas $X_2 > 0$ is an inductor. Perfect matching can be achieved by tuning X_1 and X_3 over a range of R_D and X_D. The matching network used in our experiments is an automatic L-type matchbox containing two air rotary condensers whose capacities are adjusted by means of motors. The matchbox provides the perfect matching by forwarding the total power to the discharge and ensuring that virtually no power is reflected in the power supply.

4.3   General setup

Figure 4.2 shows a top-view and a side-view schematic representation of the gen-eral experimental setup used for the conducted research. The experiments were
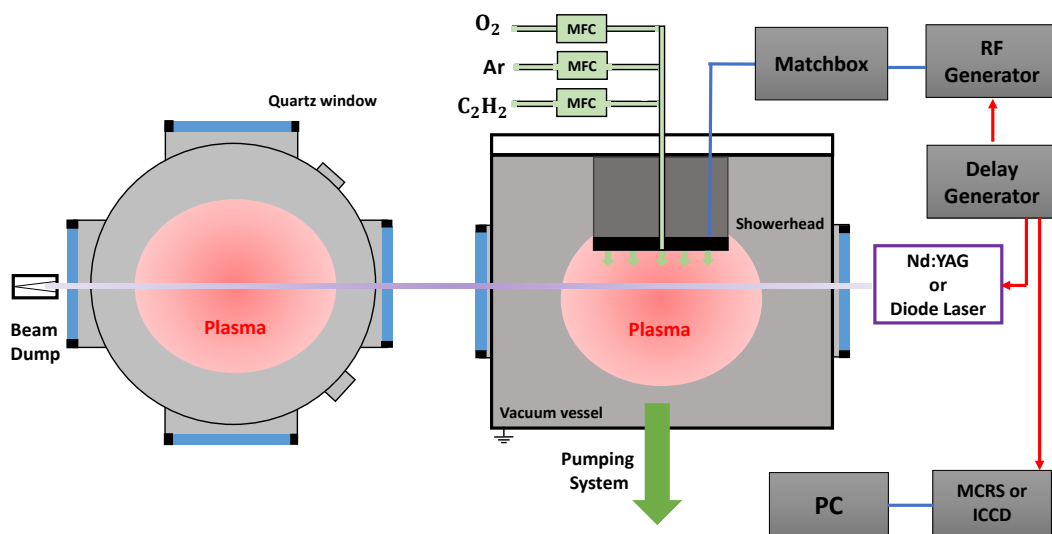
Figure 4.2: Top-view (left) and side-view (right) schematic representations of the general setup, including a vacuum setup inside which the plasma is ignited.

conducted in a cylindrical vacuum vessel that was 30 cm in diameter and 45 cm in height. It contained two pairs of concentric quartz windows, of which one pair allowed illumination with laser light while the other pair enabled the acquisition of photoluminescence emission from quantum dots (setup I) or plasma radiation (Setup II). The vessel lid contained a gas inlet connected to a showerhead-shaped electrode which was 138 mm in diameter. To ensure a homogeneous gas flow into the experiment volume, the electrode contained 331 homogeneously distributed holes (0.5 mm in diameter) through which the gas was injected. This showerhead electrode was insulated electrically with a Teflon ring from the rest of the vessel lid and was powered with an RF voltage signal to enable plasma operation underneath it. The rest of the vessel was electrically grounded, therefore, the CCP plasma operated as asymmetric.

The injected gas left the vacuum vessel at the bottom and was then pumped out by, respectively, a turbo-molecular pump and a rotary roughing pump. The base pressure inside the vessel was 3×10^{-4} Pa. During the experiments, the pressure inside the vacuum vessel and thus inside the measurement volume was controlled within the pressure range of 2-30 Pa by a butterfly valve (VAT 61332-KAAH) operated in a vacuum line - bypassing the turbo-molecular pump - between the vacuum vessel and the rotary roughing pump. The input gas (argon, oxygen, and/or acetylene) flows were kept constant by BROOKS mass flow con-

trollers.

An RF generator (Barthel RFG-13-100-L) synchronized with an automatic matchbox (Barthel MCi-300) delivered a pulsed 13.56 MHz RF signal with a power ranging from 10 to 50 W during plasma-on phases. A digital delay generator (Stanford Research Systems DG645) was used for temporal modulation of the input RF signals as well as for synchronization and triggering of the data-acquisition hardware, lasers, and ICCD camera. All the data were stored on a PC in which in-house developed software analyzed it.

4.4 Setup I: Plasma exposure of quantum dots

A top-view schematic representation of setup I is depicted in figure 4.3. This setup is designed to expose quantum dots (QDs) to the plasma and to investigate the influence of surface charging on the photoluminescence (PL) emission. The experiments were conducted in the general setup described in section 4.3. The plasma, to which the QDs were exposed, was formed in an argon background gas which was kept at a constant pressure of 4 Pa for all the experiments.

The QDs used in the experiments of chapter 5 were CdSe-ZnS core-shell QDs. The CdSe core had conduction and valence band levels of $-4.9\,\text{eV}$ and $-6.7\,\text{eV}$, respectively, with respect to the vacuum level. The resulting band gap for the core was $E_{bg,\,CdSe} = 1.8\,\text{eV}$. The ZnS shell had the energy levels of the conduction and valence band at $-3.4\,\text{eV}$ and $-7.4\,\text{eV}$, respectively [53]. As a result, the electrons (confined in the conduction band) are trapped in a well with a depth of $V_{0,\,electrons} = 1.4\,\text{eV}$, while the depth of holes (confined in the valence band) is $V_{0,\,holes} = 0.6\,\text{eV}$. Table 4.1 provides the specification of the QDs used in the experiments of chapter 5.

First, the QDs were drop-cast and deposited on a silicon substrate. This QD-deposited silicon substrate was clamped to a stainless-steel substrate holder, which was electrically insulated from the grounded walls of the vacuum vessel. Illumination laser light was introduced into the chamber through a quartz window. PL emission from the QDs was observed at 90° with respect to the illumination direction through another quartz window. Hence it was technically floating. The plasma-exposed QDs on the sample were excited using a temperature-controlled pulsed laser system consisting of a laser diode (Thorlabs L405G1) with a wavelength of 405 nm, together with a laser diode driver (Thorlabs ITC4005) enabling pulse-width modulation and pulsing of the laser diode corresponding to square pulses delivered by the signal generator (Keysight 33509B). The laser beam was collimated and directed to the spot on which the QDs were deposited on the sili-

con substrate using a mirror and a collimator lens.

PL emission from the QDs was collected using a pair of confocal lenses (with identical focal lengths of $f_1 = f_2 = 200$ mm (see figure 4.3) and focused onto the 250 μm wide entrance slit of the monochromator (Acton Research SpectraPro275), where it was spectrally resolved. Afterward, the spectrum was recorded by an ICCD camera (Andor iStar 334T) mounted directly behind the monochromator. The camera recorded a time series of spectra synchronized with the laser pulses. The laser was pulsed in order to allow the recording of both the background emission and the PL signals from the excited QDs for consecutive pulses. A band pass filter (central wavelength = 540 nm, FWHM = 50 nm) ensured the collection of mostly PL emission light measurement by attenuating most of the plasma emission, which could otherwise induce additional noise.

As the photoluminescence spectra of the QDs are sensitive to temperature-induced effects (elaborated on in previous section 2.5.5) resulting from, in our case, heat fluxes from the plasma, the measurement and recording of the temperature of the QD sample is essential. Therefore, a temperature sensor (PT-1000) was installed in the substrate holder to record temperature trends during the measurements. The data were stored in a PC and analyzed with in-house developed scripts.

Plasma parameters such as the electron temperature (T_e), the floating potential (V_f), and the plasma potential (V_p) were measured using a Langmuir probe (Impedance P2516i). The software delivered by the supplier interpreted the I-V characteristic curves of the probe and calculated the above-mentioned plasma parameters. The Langmuir probe and the floating substrate were simultaneously inside the chamber, where the probe was positioned a few centimeters apart from the sample with the QDs. This configuration enabled the measurement of the local values of the bulk plasma parameters in the vicinity of the floating substrate. The aforementioned plasma parameters were used to approximate the electric fields in the plasma sheath formed around the floating substrate (discussed in chapter 5).
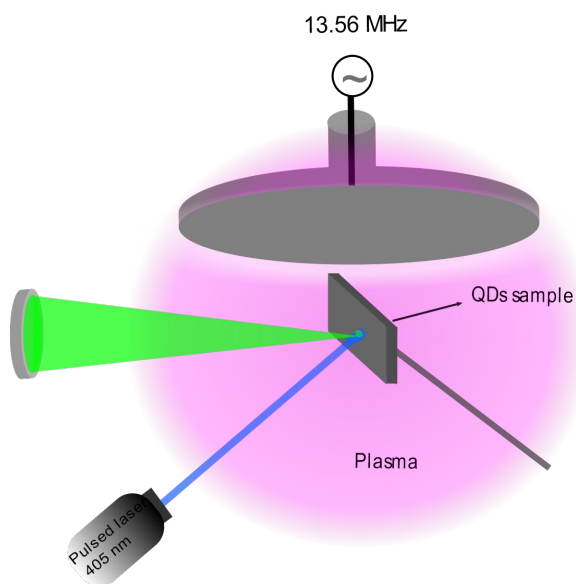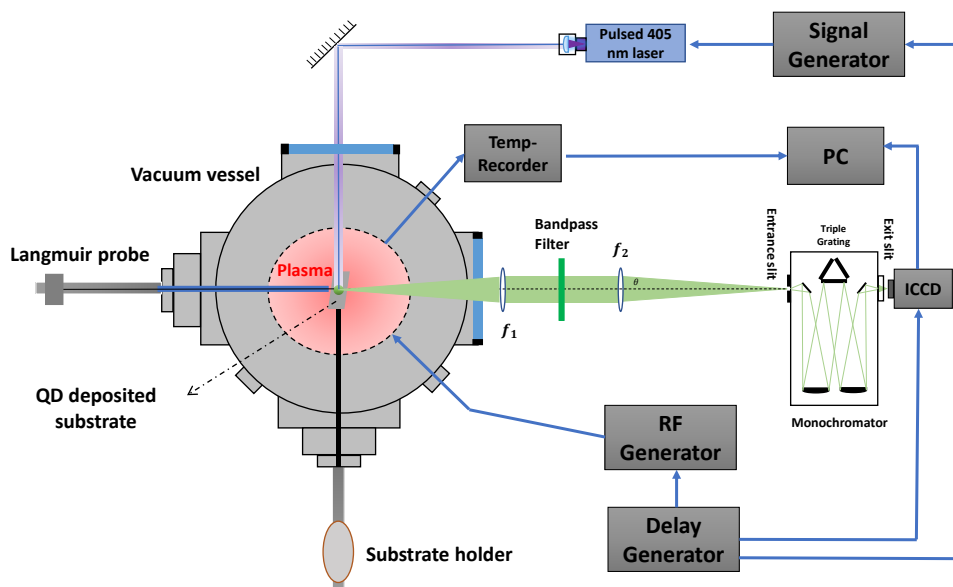
Figure 4.3: Schematic representation of setup I: The electrically floating substrate on which the QDs are deposited and optically excited by a laser and exposed to a low-pressure argon plasma. The PL emission is collected, directed into a monochromator, and detected using an ICCD camera.

Table 4.1: Specifications of the CdSe/ZnS core-shell quantum dots used in the experiments of chapter 5

Parameter	Value
Quantum dot core material	CdSe
Quantum dot shell material	ZnS
Core radius a_{core}	2.2 nm
Shell thickness	0.9 nm
Total (core + shell) radius a_{total}	3.1 nm
Electron rest mass m_e	9.1×10^{-31} kg
Effective electron mass in core $m^*_{e,core}$	0.13 m_0
Effective electron mass in shell $m^*_{e,shell}$	0.42 m_0
Effective hole mass in core $m^*_{h,core}$	0.30 m_0
Effective hole mass in shell $m^*_{h,shell}$	0.61 m_0
Conduction band well depth $V_{0,e}$	1.4 eV
Valence band well depth $V_{0,h}$	0.6 eV
Band gap energy E_{bg}	1.8 eV

4.5   Setup II: MCRS and LIP

Setup II is designed to measure the density of electrons, anions, and small clusters of dust particles in electronegative and reactive plasmas. To this end, the microwave cavity resonance spectroscopy (MCRS) technique explained in chapter 3 is implemented, enabling the measurement of the electron density temporally resolved. Subsequently, the laser-induced photodetachment (LIP) technique is implemented by applying pulses of laser light at different wavelengths to distinguishably measure the density of negative species.

4.5.1   Microwave cavity resonance spectroscopy setup

The top image in figure 4.4 shows a schematic representation of the experimental setup for MCRS measurements. The vacuum vessel contained instruments for the ignition of the plasma in pure oxygen (in chapter 6) or argon-acetylene mixture (in chapter 7) gases. The cavity inside which the discharge was operated consisted of the showerhead used as the driving electrode while the rest of the cavity electrically served as ground. Therefore, the plasma was operated in an asymmetric fashion.

The designed cavity, illustrated in figure 4.4 (bottom), is a grounded aluminum hollow cylindrical resonant pill-box cavity with an internal diameter of 170 mm and an internal height of 67 mm and was mounted below the showerhead electrode in an electrically insulated manner. The bottom of this cavity contained 105 holes (0.5 millimeters in diameter) evenly distributed over the full surface to allow the injected gas to leave the cavity without friction and hence to ensure a stable gas pressure inside the measurement volume. The reason for the usage of the cavity was twofold. First, it served to confine the generated plasma inside a well-defined volume below the RF-powered showerhead top electrode (cavity and confined plasma are illustrated in figure 4.4). This well-defined volume is important for the calculation of the absolute negatively charged species density values from the experimental data. Second, this cavity was used as a microwave resonant cavity to temporally resolve the plasma electron density and negatively charged species densities. The plasma had a typical Debye length of $\lambda_D \approx 1$ mm (assuming $T_e = 2.5$ eV and an electron density of a few times 10^{14} m^{-3}) while the typical sheath thickness is known to be s $\approx 5 - 10\lambda_D$. Therefore, the holes in the showerhead and bottom plate, which were designed as small as possible, did not have any major effect on plasma properties.

A single metal antenna, that simultaneously served as both transmitter and receiver for low-power microwave (0.3-8 GHz) signals, was a straight fixed piece

of copper wire. This transmitter-receiver antenna was connected to the data-acquisition system, as will be discussed in the next section. Two 12-mm-diameter circular holes, aligned opposite to each other in the cavity's circumferential wall and perpendicular to the antenna's plane, enabled the laser beam to pass through the cavity without hitting the wall and generating secondary electrons (see figure 4.4 (bottom)). The diameter of these holes was smaller than the wavelength of the exciting microwaves, preventing significant leakage of microwaves from the cavity volume.

Data-acquition hardware

The used data-acquisition hardware has been already extensively elaborated in the previous articles published by the CIMlabs group [5, 60]. However, a brief description, including recent upgrades, will be provided below. As can be seen in figure 4.4 (top), a microwave generator (Stanford Research Systems SG386) produced a sinusoidal microwave signal at 16 dBm power at a frequency externally set. This output was connected to the input port of a directional coupler (Mini-Circuits ZHDC-10-63-S+) and passed unhindered to its output port, which was connected to the antenna inside the cavity. Henceforth, by applying the correct frequency from the microwave generator, resonant modes could be excited in the cavity. If the cavity is off-resonance, power coupling to it is very inefficient and most of the power reaching the antenna reflects back to the microwave generator, where it is dissipated. If the cavity is at its resonance, hardly any signal reflects back since most of the energy is dissipated by building up the resonant electromagnetic field inside the cavity. This translates into a sharp minimum in the reflected power spectrum at - and closely around - the resonance frequency of the excited mode. Note that the total microwave power used (several mW) is negligible with respect to the RF power ($\sim$10 -15 W) used to drive the plasma.

In our setup, however, part of the reflected signal ($\sim$10 %), was rerouted by the directional coupler to the measurement leg of the detection system, where it was first converted to a DC signal by a logarithmic power detector (Hittite 602LP4E with 10 ns rise and fall times) and subsequently fed to a high-frequency (up to 250 MHz) transient recorder (Spectrum M4i.4420-x8) inside the measurement PC. The transient recorder continuously sampled its input port and stored the data in its internal memory. Only upon an external trigger, for which the trigger signal was provided by the used delay generator, data was made available to the user for subsequent analysis. This arrangement offered the possibility of obtaining the MCRS response even before the actual trigger had occurred.
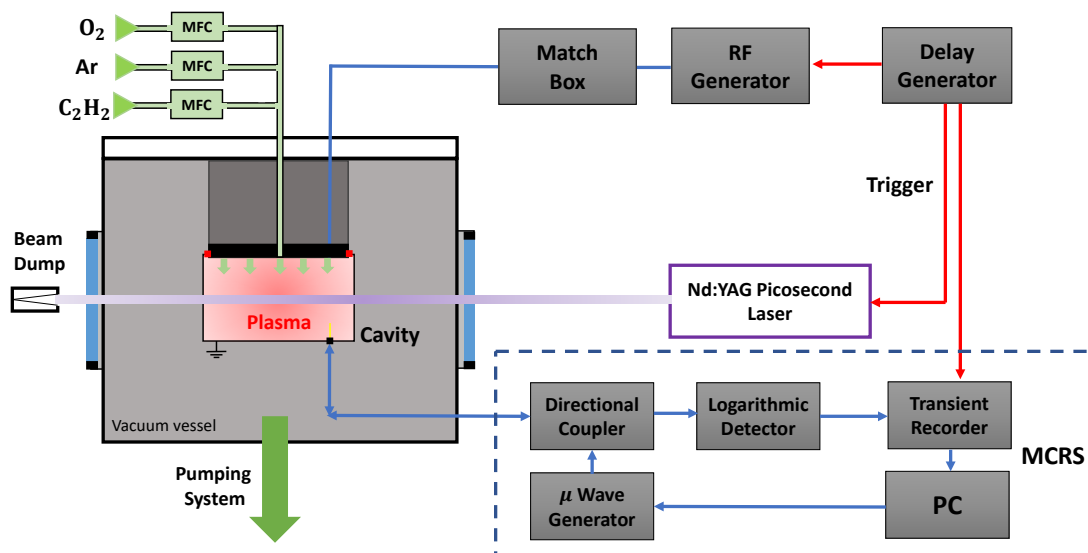
Figure 4.4: Schematic representation of setup II (top) and a 3-D model of the cavity designed for the MCRS measurements (bottom). The plasma is confined inside the cavity to which the microwave radiation to conduct MCRS is transmitted and received by an antenna. The cavity has holes that accommodate the passage of the laser beam.

4.5.2 Laser-induced photodetachment setup

The laser-induced photodetachment (LIP) experiments (in chapter 6 and 7) were performed using a pulsed Nd:YAG laser (Ekspla SL235) operated at its fundamental mode in 1064 nm, second harmonic at 532 nm, and fourth harmonic at 266 nm. The laser generated short (150 ps) pulses with an energy of 490 mJ at 1064 nm, 291 mJ at 532 nm, and 90 mJ at 266 nm at a 5 Hz repetition rate. The laser beam profile was top-hat with a diameter of 11.5 mm. In order to trigger the laser, two trigger signals were fed to the laser. One signal marks the pumping and Q-switch, and the other marks the onset of the laser beam, which was used as a reference signal for the synchronization of the other equipment. The laser, transient recorder, and RF generation were accurately synchronized by a delay generator. Three pulses with an adjustable delay were fed to the instruments. For instance, for measurements in the plasma afterglow phase (i.e. after the plasma power was terminated) at the time t_A, the RF generator was triggered for the plasma to be switched off. The transient recorder was triggered at t_B to record the cavity's response during the afterglow and temporally around the photodetachment incident. t_R indicates the total amount of time the MRCS signal was recorded. The laser was set to illuminate the plasma at t_C with a delay of Δt compared to the beginning of the afterglow phase (i.e. compared to the moment at which the plasma was switched off). With this delay pattern, illustrated in Figure 4.5, an arbitrary time interval during the afterglow of the plasma could be investigated.

The LIP technique was used to detect and measure the density of negatively charged species (i.e. anions and dust particles) in the plasma. As explained earlier in section 3.3, the photodetachment incidents result in the release of (photodetached) electrons that can be subsequently detected by the MCRS technique. The necessary condition for a photodetachment incident is that the photon energy of the laser beam exceeds the electron affinity of the negative ion(s) that are to be detected. Therefore, one can differentiate between the contributions of different species of anions by adjusting the photon energy. For instance, in the experiments of chapter 6, the fundamental mode of the Nd:YAG laser was used to probe the density of O_2^- anions. Using the second harmonic of the same laser system enables the detection of all anions O^-, O_2^-, and O_3^-. Table 4.2 provides information about the electron affinities of O^-, O_2^- and O_3^-, the photon energies of the different laser modes, and the photodetachment cross section for each species at the respective laser wavelengths. By cleverly taking the difference between the photodetachment signals at 532 nm and at 1064 nm - including the scaling of the laser pulse power, photodetachment cross sections, etc.- the individual contribution of
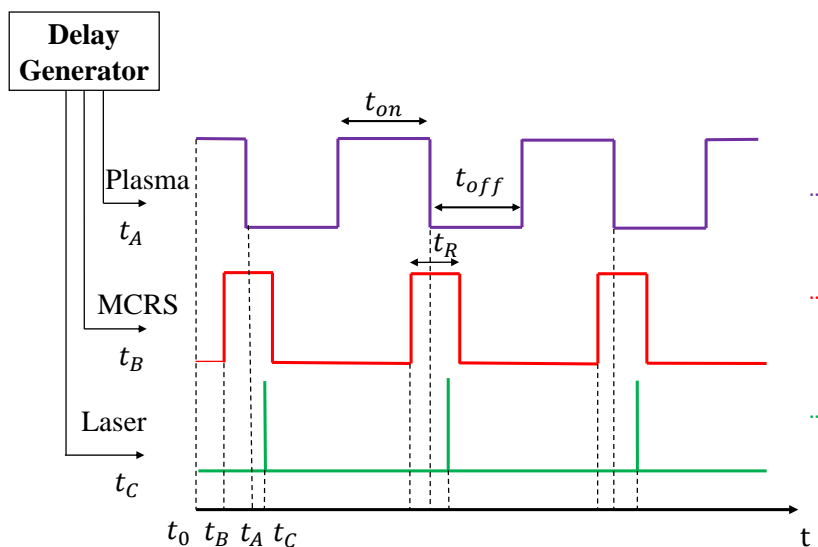
Figure 4.5: Delay pattern of the photodetachment experiments: $t_C - t_A = \Delta t$.

at least O_2^- to the total anion density can be pinpointed.

First, by setting the laser wavelength to 532 nm, all involved negative ions - O^-, O_2^- and O_3^- - contribute to the overall photodetachment signal which can be probed by MCRS and provides information regarding the total negative ion density. The contribution of O^- to the overall photodetachment signal is significant since, firstly, in such oxygen plasmas, O^- is by far the most dominant negative ion [61] and, secondly, the photodetachment cross section of O^- is about three to six times higher than the other negative ions' cross sections at the respective 532 nm. Due to the relatively lower concentration of the other involved negative ions (with O_2^- roughly constituting 10% and O_3^- roughly constituting 1% of the total negative ions), their contributions to total photodetachment signal is considered marginal. Subsequently, after setting the laser wavelength to 1064 nm, only O_2^- is vulnerable to LIP and, hence, when probing the photodetachment signal with MCRS, information can be obtained with respect to the density of O_2^- alone.

In the experiments of chapter 7, the laser operated at its fourth harmonic corresponding with the 266 nm wavelength of the beam. Therefore, the maximum photon energy of the laser (4.66 eV) was deployed to ensure the photodetachment of all the negatively charged species present in the reactive plasma. The same delay pattern shown in figure 4.4 was used to measure the densities of electrons and negatively charged species at a specific time in the afterglow of the plasma.

Table 4.2: Electron affinities of negative ion species in oxygen plasma and their photodetachment cross section [62–66].

Anion	Electron affinity (eV)	Cross-section (m^2)	Photon energy (eV)	Wavelength (nm)
O_2^-	0.45	0.5×10^{-22}	1.16	1064
O_2^-	0.45	2×10^{-22}	2.3	532
O^-	1.46	6.5×10^{-22}	2.3	532
O_3^-	2.10	1×10^{-22}	2.3	532

Chapter 5

Quantum dot photoluminescence as charge probe for plasma exposed surfaces

Abstract

Quantum dots (QDs) are used as nanometer-sized *in-situ* charge probes for surfaces exposed to plasma. Excess charges residing on an electrically floating surface immersed in a low-pressure argon plasma are detected and investigated by analysis of variations in the photoluminescence (PL) spectrum of laser-excited QDs that were deposited on that surface. The experimentally demonstrated redshift of the PL spectrum peak is linked to electric fields associated with charges near the QDs' surfaces, a phenomenon entitled the quantum-confined Stark effect. Variations in the surface charge as a function of plasma input power result in different values of the redshift of the peak position of the PL spectrum. The values of redshift are detected to be 0.022 nm and 0.073 nm for 10 W and 90 W input powers, respectively, therefore indicating an increasing trend. From that, a higher microscopic electric field, 9.29×10^6 V/m for 90 W compared to 3.29×10^6 V/m for 10 W input power, which is coupled to an increased electric field in the plasma sheath, is sensed by the QDs when plasma input power is increased.

5.1 Introduction

Plasmas containing nano- to micrometer-sized dust particulates, designated as complex or dusty plasmas, are of immense importance due to the nanoparticles' either potential threat or advantageous role in multitudinous sciences and technologies. Dust particles are, for instance, advantageous for the creation of self-organized plasma crystals [67] and plasma-assisted fabrication of nanostructures and polymers [34, 68]. Recently, detrimental effects of dust particulates for contamination control purposes in high-tech [69] and semiconductor [70] industries have been observed and studied. Plasma charging of particles, either levitated or adhered to surfaces, is the process that determines the dynamics of contaminating particulates in complex ionized media such as those in lithography scanners [71] or those with respect to spacecraft charging during the atmosphere re-entry [72]. Connected to that, electrically floating surfaces are known to accumulate negative charge, i.e. an excess of electrons, when exposed to, for instance, radiofrequency (RF) [23, 73] or EUV-induced [74] plasmas since the electrons possess higher mobility compared to ions. Charge accumulation on these surfaces is studied to account for various phenomena such as particle lofting [75]. Crucial in these applications is the fundamental understanding of charging of particle-laden surfaces immersed in plasmas for which so far a comprehensive model predicting the charging dynamics does not exist. Also, experimental data on electric fields surrounding the surfaces as well as accurate surface charge measurements are scarce.

The amount of (negative) charge on a surface in contact with plasma is determined by the balance of incoming and outgoing ion and electron fluxes; those can be measured experimentally [76] and modeled numerically [77]. Furthermore, particle charge on a surface can be calculated using the "shared charge model" [13]. According to this model, the charge density depends on the plasma sheath electric field around the surface. This sheath electric field was modeled by Sheridan *et al.*, assuming a planar, collisionless and dc sheath in a plasma where the electrons are described by a bi-Maxwellian distribution [13]. Simulations of Kim *et al.* illustrate a two-dimensional sheath profile at an interface between an insulator-conductor floating surface exposed to a high-density plasma [78].

The sheath electric field was measured spatially resolved in radio-frequently (RF) driven argon plasmas by using either microparticle probes under hypergravity conditions [79] or by deploying laser-induced fluorescence-dip spectroscopy by Barnat *et al.* [80]. In the latter technique, laser-excited Argon Rydberg levels are Stark-shifted due to the electric field around the probe. Since those argon atoms were excited externally by a laser, an active spectroscopy scheme was pro-

posed using laser excitation of well-defined energy levels of an atom and as a diagnostic method for measuring electric fields. Similarly, Stark-shifted energy states of an "artificial atom", i.e. of a quantum dot, can in principle be used for electric field measurements near a surface since their discrete energy level structure is also subject to electric-field-induced shifts and alterations [81].

Although the electric field profiles around an electrically floating and biased object were measured [82], an *in-situ* measurement of the plasma sheath electric fields on a particle-laden surface facing a plasma has not been performed yet. Experimentally investigating the plasma sheath electric fields with surface-deposited quantum dots would provide unique insights into the charging mechanisms of nanoparticles. Experimental data regarding the charging of nanoparticles are scarce in the literature, partly because a particle's charge decreases with its size, which necessitates high-resolution diagnostic methods [17]. The problem of charging of particles residing on plasma-facing surfaces was considered both theoretically [83] and experimentally [84] only for micrometer-sized particles and not for nanometer-sized particles which pose an increasing challenge in future contamination control applications.

Pioneered recently by Marvi *et al.* [85], photoluminescent nanoparticles have been used to visualize interactions between plasma and a particle-laden surface. In that work, the idea of using the photoluminescence of semiconductor quantum dots (QDs) as a diagnostic method for surface charging of nanoparticles due to plasma interaction was proposed. Furthermore, Pustylnik *et al.* [86, 87] have theoretically shown that a layer of QDs deposited on the surface of a microparticle could provide the possibility of measuring the surface charge of microparticles in plasmas.

In this chapter, we further develop the diagnostic tool that visualizes the charging of a plasma-exposed surface using photoluminescence (PL) spectra of nanometer-sized QDs. For this purpose, PL spectra of QDs deposited on an electrically floating substrate have been recorded before, during, and after plasma exposure. Distinctly in this study, reproducible measurements are performed to quantify the values of the electric-field-induced redshift of the peak of the PL spectrum of the QDs, previously characterized as Stark shift [85]. These values of Stark shift are measured at various plasma conditions (i.e. at different input powers). Moreover, the measured values of Stark shift are interpreted using a surface charge model. A Langmuir probe is used to extract plasma parameters (e.g. electron temperature) at the conditions of the Stark shift measurements. These plasma parameters are then used for estimations of the sheath electric field using traditional RF sheath theory.

The current chapter is organized as follows: First, an overview of the exper-

imental methodology is presented in section 5.2. A detailed description of the
measurements of the photoluminescence spectra of the QDs is provided in that
section. Next, in section 5.3, the experimental results and observations of QD PL
spectra from these nanocrystals as exposed to low-pressure RF plasma in various
conditions are provided. Finally, section 5.4 contains the interpretation of the
experimentally investigated phenomena. Section 5.5 concludes this chapter.

5.2 Methods

A detailed description of the experimental methodology applied to explore the
charging of a plasma-exposed surface with QDs deposited on it is provided in the
following subsections. QD photoluminescence employed as a diagnostic tool is
introduced in section 5.2.1. The experimental setup designed for investigating the
effect of plasma on the PL emission spectrum of the QDs was already presented
and explained in section 4.4 of chapter 4. Finally, data acquisition and analysis
procedures are explained in section 5.2.2.

5.2.1 Quantum dot photoluminescence

QDs are nanometer-sized crystalline semiconductors characterized inherently as
zero-dimensional quantum wells for charge carriers. The optical characteristics
of these QDs are dependent, among other parameters, on their size. QDs typi-
cally have a core-shell structure. The main semiconductor in the core determines
the properties, whereas the shell stabilizes those. A QD nanocrystal is optically
excited upon receiving a photon whose energy exceeds the energy gap between
the valence and conduction bands, followed by the generation and confinement of
an electron-hole pair. In the next stage, the electron-hole pair relaxes back to the
bound states of the QD's corresponding quantum well; finally, the recombination
of the electron and hole leads to the emission of a photon with a well-defined
energy. As a consequence of charge carrier relaxation, the energy of an emitted
photon is lower than that of an excitation photon. Since in this work the emis-
sion from an ensemble of QDs with a certain size distribution is observed, the
associated photoluminescence peak is broadened corresponding to the size dis-
tribution. A PL emission peak of an ensemble of QDs can be characterized by
three values: the central wavelength, the integrated intensity, and the Full-Width
at Half-Maximum (FWHM).

Measurements of the QD photoluminescence spectrum and analysis of the
above-mentioned values allow using QDs as *in-situ* charging probes. In this work,

the QDs are deposited on a substrate and exposed to a low-pressure RF Argon plasma. Optical excitation is performed by a laser. The charges on the surface of an electrically floating substrate create the electric field. This electric field affects the PL of the QDs due to the quantum-confined Stark effect [50], which allows obtaining the information on charging from the PL spectra.

The QDs used in this work were commercially available (NanoOpticalMaterials) colloidal CdSSe-ZnS gradient-alloyed shell QDs. In this specific type of QDs, blinking effects were nearly suppressed and the quantum yield was enhanced by constructing a band structure that confines the exciton within the core [88, 89]. Therefore, the Auger effect, as a non-radiative process responsible for blinking, was suppressed. The peak of the PL of the QDs was at $\lambda_p = 540\pm10$ nm and FWHM = 34 nm; their core radius and shell thickness were 2.2 nm and 0.9 nm, respectively. For each QD sample, 10 μl of the original colloidal solution with 4 mg/ml concentration were drop-cast on a reflective silicon substrate, therefore resulting in a surface density of about 3.8×10^{-11} mol/mm^2 and layer thickness of 7.5 μm, assuming the QDs were homogeneously dispersed. The relative dielectric constant of the QDs was approximately [90] $\varepsilon_r = 6.19$. After total evaporation of the solvent, the QDs stayed on the substrate. The QD-deposited silicon substrate was clamped to a stainless-steel substrate holder which was electrically insulated from the grounded walls of the vacuum vessel. Therefore, with this configuration, a floating potential with respect to the surrounding plasma was ascribed to the QD sample since the whole sample was immersed in the plasma volume. The photoluminescence of the drop-cast QDs on the sample stimulated by laser excitation was continuously recorded before, during, and after plasma exposure. The photoluminescence was temporally and spectrally resolved with 0.075 s and 1.5 pm maximal temporal and spectral resolution, respectively, using the experimental setup described in chapter 4.

5.2.2 Measurement and fitting procedure

Fig. 5.1 represents a typical measurement of a PL spectrum before any plasma exposure together with the fit. The fitting procedure will be described below. Measurements were performed in a consecutive fashion as time series synchronized with the laser pulses. The internal clock of the ICCD camera served as the reference clock, according to which plasma and laser pulses were synchronized via the delay generator. In order to acquire a sufficient amount of PL light and to ensure optimal signal-to-noise ratio, each acquisition consisted of 100 accumulated individual spectra, repeated consecutively for background (without laser excitation) and PL (with laser excitation) measurements. Each PL measurement
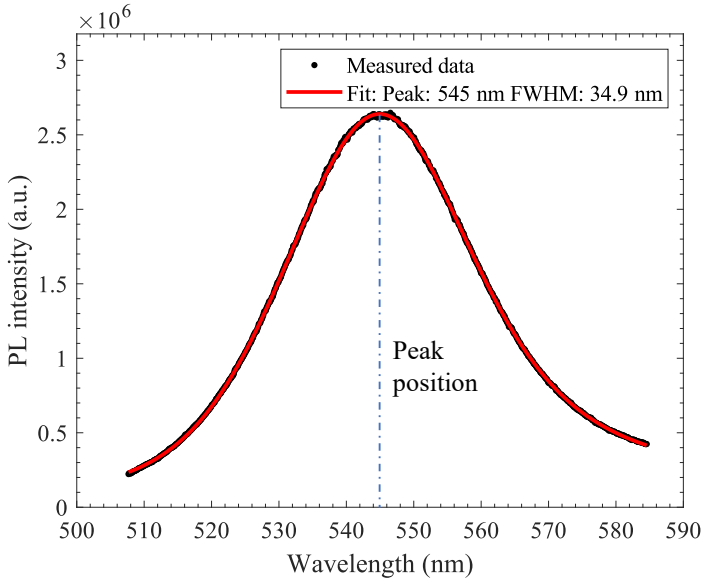
Figure 5.1: PL emission spectrum of the QDs: The recorded data (black dots) and the modified Voigt fitting (red curve). The wavelength at which the PL intensity reaches maximum indicates the PL peak position.

was subtracted from the average of its previous and next background measurement to reconstruct the PL spectra (black dots in Fig. 5.1).

The position of the PL peak was determined using the following fitting procedure. After averaging the data over 100 repeated measurements, the PL peak was fitted using a double skewed Voigt function developed specifically for this procedure (see Appendix 5.A). This double skewed Voigt distribution (ϕ_V) consisted of a weighted distribution of a Gaussian and a Lorentzian probability density function (ϕ_G and ϕ_L) multiplied by their respective cumulative distribution functions (Φ_g and Φ_L) as indicated in the following expression:

$$\phi_V(x) = 2(1-\eta)\phi_G(x)\Phi_G(a_G x) + 2\eta\phi_L(x)\Phi_L(a_L x). \tag{5.1}$$

Here, η is the Voigt weight factor and a_G and a_L are the skew parameters of the Gaussian and Lorentzian probability density functions, respectively. This double-skewed Voigt distribution approximated the data with R^2 of 0.9998. The primary reason for developing this specific set of fitting functions was asymmetry in the measured data caused by non-linearities of the image intensifier of the ICCD camera, skewing the spectrum of the PL emission. The PL peak position
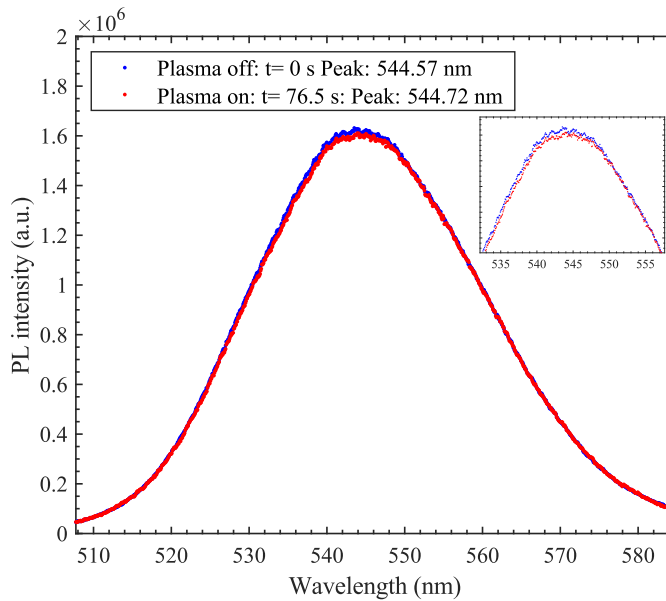
Figure 5.2: PL emission spectrum of the QDs before (blue dots) and after 76.5 s (red dots) of plasma exposure: The peak has experienced a 0.15 nm shift. The peak intensity has slightly declined.

was assigned to the peak and the PL intensity to the integral of the skewed Voigt function resulting from the fit.

Next, variations of the PL peak position and peak intensity were determined during each experiment. Fig. 5.2 exemplary shows two respective PL peaks: One at the beginning of a typical experiment, and the other the QDs' PL emission after 76.5 s of plasma exposure (red dots). It is visible that the peak slightly shifts towards a longer wavelength, indicating a "*redshift*", while the peak intensity slightly decreased.

Multiple trials of exposing the QDs to plasma were performed, during which the PL peak positions were measured in several plasma pulses of equal duration and subsequently averaged over these pulses. This averaging scheme was designed to track the PL peak position and intensities precisely, enabling further quantitative analysis when the input power of the plasma was subject to change. With this procedure, the PL peak position was determined with a 0.002 nm error.

5.3 Results

PL spectra from the QD sample in contact with the low-pressure, low-temperature RF plasma have been recorded and analyzed. First, the general effect of the plasma on the PL spectra of the QDs is discussed in Section 5.3.1. Time-resolved spectra are measured and the time evolution of the PL peak position and intensity are subsequently determined. As will be explained later in this section, both temperature-induced and electric-field-induced redshifts are revealed throughout the long plasma exposure trial. Section 5.3.2 contains the results on measurements of a fast, electric-field-induced, shift, associated with the quantum-confined Stark effect. It also shows how this fast shift can be distinguished from substantially longer temperature-induced effects. Section 5.3.3 proceeds to the quantification of the Stark shift using enhanced measurement techniques (e.g. averaging scheme) to minimize the error margin in the peak position determination. Finally, section 5.3.4 establishes the dependence of the Stark shift on the plasma input power.

5.3.1 Time-resolved PL spectra: The "*slow shift*" and the "*fast shift*"

As illustrated in Fig. 5.3, the two main features of the PL spectrum, the peak position, and the peak intensity are subject to change due to exposure of the QDs to plasma. At the beginning of the experiments, before any plasma exposure, both the peak position and the peak intensity are constant. At the moment when the plasma is switched on, a sharp, instant, and fast shift of about 0.04 nm in the peak position towards longer wavelengths is observed (see Fig. 5.3 (a)). Afterward, a gradual, ramp-like, and slow shift of 0.11 nm in total proceeds as the plasma affects the QDs on an extended time scale of 76.5 s. Marking the switching off of the plasma, a fast shift of the peak position is observed, which is symmetrical - equal in magnitude but reverse in direction - to the initial fast shift. Finally, a gradual slow shift towards the initial values appears. However, the peak position reaches a stable value slightly higher than that for the pristine QD sample before plasma exposure. Similarly, the trend in the integrated intensity of the PL peak appears to show a gradual decline as the QDs are exposed to the plasma on the same time scale. Similarly to the PL peak position, the PL intensity also does not recover to its value for the pristine QD sample (see Fig. 5.3 (b)).

We term the sudden increase of the PL peak position "*fast shift*". The gradual and ramp-like shift occurring on the longer time scale, we term the "*slow shift*". Obviously, the trend in the slow shift follows the trend in the substrate temper-
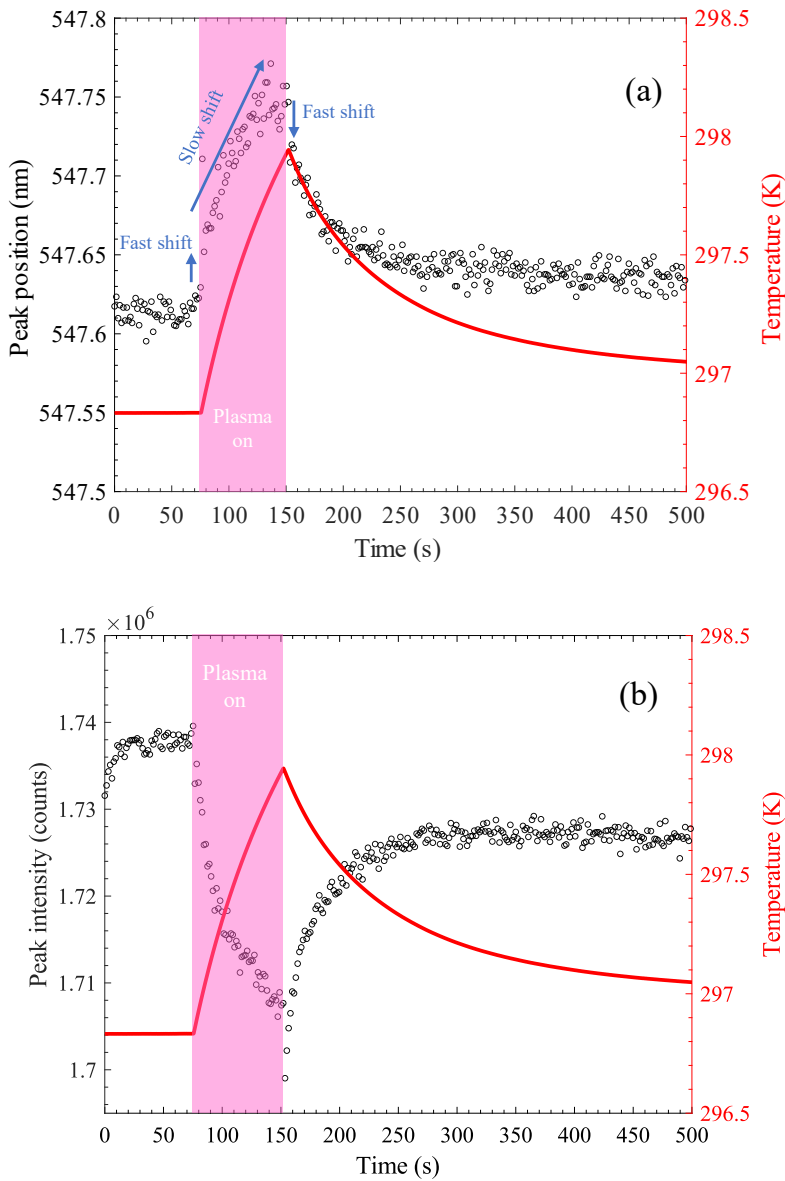
Figure 5.3: Temporal evolution of (a) the peak position (left axis, black dots) together with the substrate temperature (right axis, red curve) and (b) the integrated intensity (left axis, black dots) together with the substrate temperature (right axis, red curve). The experiment included 76.5 s of plasma exposure (pink region).

ature (see Fig. 5.3 (a)), which rises during plasma exposure and exponentially declines after the exposure is stopped. Therefore, we attribute the slow shift to temperature-induced effects caused by the thermal plasma load on the substrate surface. The fast shift occurs much faster than the temperature evolution of the substrate does, and therefore, we attribute this shift to the quantum-confined Stark effect caused by plasma-induced surface charges and their associated electric fields.

The substrate temperature is measured to rise 1.1 K during 76.5 s of plasma exposure. The rate of the temperature-induced redshift is approximately 0.1 nm/K according to this measurement. This value was cross-checked by externally heating the QDs substrate without any plasma exposure, where the trend of the slow shift corresponded exactly to that of the temperature [85] while the fast shift, observed in the plasma exposure experiments, did not occur. Recently, a detailed evaluation of the thermal balance of surface-deposited QDs was published [87]. The results of this evaluation practically rule out any transient thermal effect that could obscure the quantum-confined Stark effect.

According to the observations described above, the fast shift and the (temperature-induced) slow shift occur on different timescales which allows to undoubtedly distinguish between them. The following section presents a different set of experiments in which we could reduce the slow shift to negligibly small magnitudes in order to better investigate the fast shift.

5.3.2 Stark shift

Upon plasma exposure of the QDs, two specific effects in the temporal evolution of the PL peak position and the PL emission intensity are observed. While the temperature-related effects [91, 92] on the PL of the QDs are of marginal importance for this work, the charge-related effects are the focus of this chapter. A series of experiments, thereby, was designed to reduce the temperature-related effects.

To isolate the Stark shift, the time during which the QD sample was exposed to the plasma was shortened step by step. As the exposure time was decreased, the QDs had lesser time to attain any significant temperature rise, which would induce observable redshifts. The QDs, and the substrate on which they were deposited, were exposed to the plasma for 76.5 s (see Figs. 5.2 and 5.3). In further experiments, the exposure time was set to 30, 18, and 4.5 s, as can be seen in Fig. 5.4 (b) to Fig. 5.5 (d), respectively. As demonstrated in Fig. 5.4 and Fig. 5.5, the effect is clearly visible at the plasma durations of 76.5 s, 30 s, and 18 s. The temperature of the substrate and, therefore, of the QDs was measured to rise 1.1

K, 0.6 K, and 0.3 K during 76.5 s, 30 s, and 18 s of plasma exposure, respectively (see Fig. 5.4 (a), (b) and Fig. 5.5(c)). For the last experiment (Fig. 5.5 (d)), the exposure time was set to 4.5 s only, which was sufficient to gather enough data and, at the same time, to produce only a negligibly small temperature effect. Also, at 4.5 s plasma duration, the PL peak position recovered to its value before the plasma exposure. Hence, for a sufficiently short plasma exposure time (here 4.5 s and shorter), the temperature effects become negligible, and a pure Stark shift can be observed. The PL peak intensity, nevertheless, has a longer (about 20 s) recovery time and relaxes to a value that is slightly below the initial one (Fig.5.5 (d), red dots). This effect was already reported by Marvi et al. [85] and can be attributed to the damage of the QDs by impinging plasma ions.

So far, this chapter has focused on proof-of-principle evidence and a clear demonstration of the appearance of the Stark effect, both accompanied by a qualitative explanation. In the following section, we present the procedure we used for the measurement of the dependence of the Stark shift on the plasma input power.

5.3.3 Quantifying Stark shift

The peak position of the PL emission of the QDs spectrally shifts as excess charges (in our case, electrons) and their associated electric fields appear on the substrate surface. This phenomenon, identified as the Stark shift, was observed, distinguishable from temperature-related effects, in the previous subsection. As the next step in the Stark shift characterization, the value of this electric-field-induced fast shift was measured reproducibly. The accuracy of the measurements is sufficient to perform a comparative study for different plasma input powers.

To quantify the Stark shift of the PL peak position, a more enhanced set of experiments involving averaging over multiple cycles of measurements was conducted. The QDs were then exposed to 100 short plasma pulses each lasting 0.76 s. Temperature increase over multiple plasma pulses was prevented by separating the exposure periods by $\approx$15 s, allowing the temperature of the substrate to decrease. As a result of this averaging scheme, the PL peak position was determined within a maximum standard error of the mean (SDM) of just 0.002 nm. The value of Stark shift was, afterward, calculated by subtracting the average peak positions during plasma exposure from those during non-exposure time intervals. As illustrated in Fig. 5.6, the value of Stark shift for specific plasma parameters of 50 W input power and 4 Pa gas pressure is measured to be 0.046 nm. In Fig. 5.6, the PL peak positions for each measurement are represented with pink (plasma exposure time interval) and yellow (non-exposure time interval) dots, besides that, the

Figure 5.4: Temporal evolution of the peak position (left axis, black dots) and the integrated intensity (right axis, red dots) of the spectrum of the PL of the QDs at different plasma exposure times (pink regions): (a) 76.5 s and (b) 30 s.
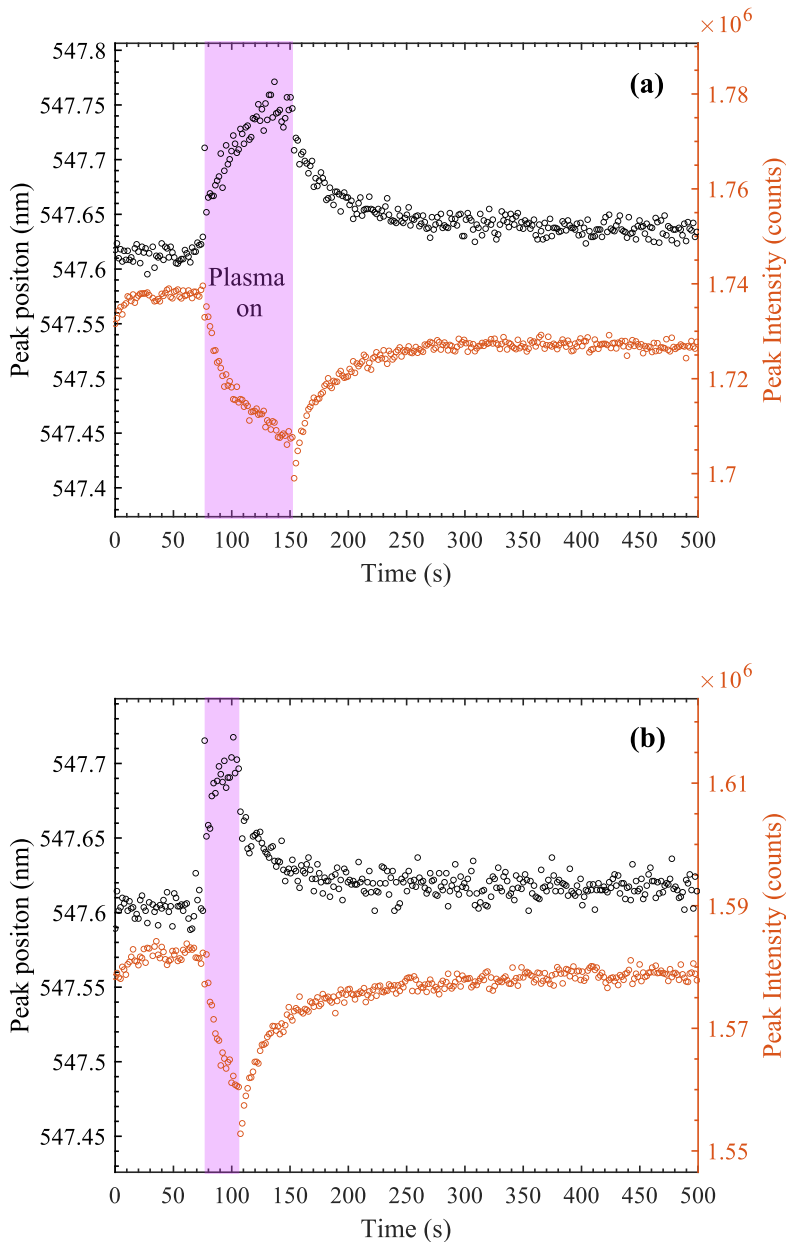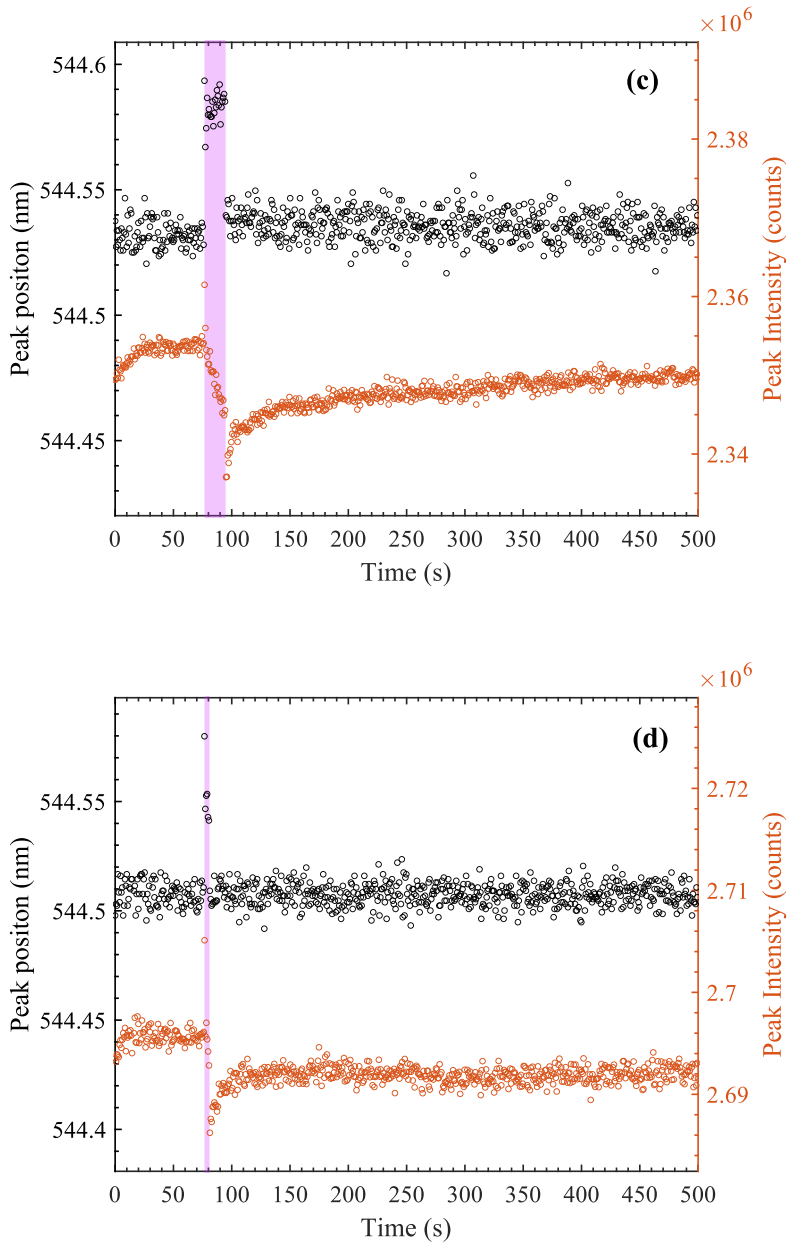
Figure 5.5: Temporal evolution of the peak position (left axis, black dots) and the integrated intensity (right axis, red dots) of the spectrum of the PL of the QDs at different plasma exposure times (pink regions): (c) 18 s and (d) 4.5 s.
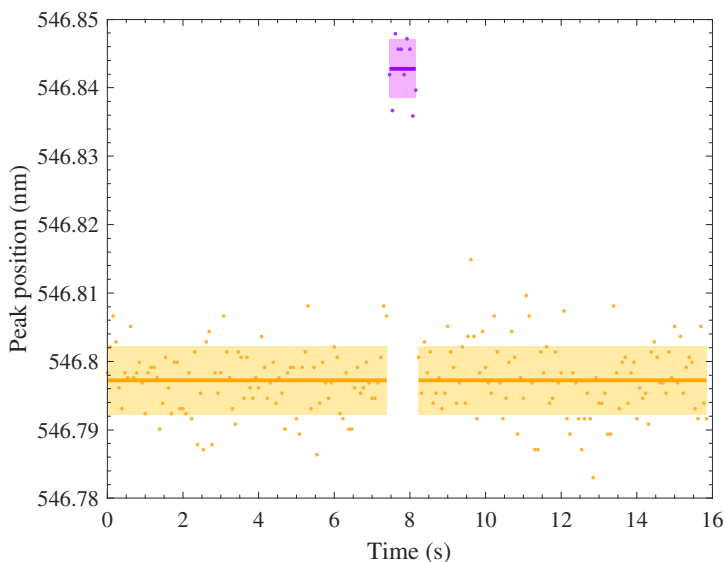
Figure 5.6: Stark shift measured for a short plasma exposure. The QDs' PL peak position during plasma exposure (0.76 s, pink dots) and non-exposure (yellow dots) time intervals. The pink and yellow areas and lines indicate the standard deviation and the average of the data points, respectively. For the specific plasma parameters of 50 W and 4 Pa, the Stark shift is measured to be 0.046 nm.

heights of the colored areas correspond to the standard deviations for respective measurement intervals and the solid lines indicate the average of the respective measurement intervals.

5.3.4 Stark shift depending on the plasma input power

We applied the procedure described in the previous subsection to systematically measure the dependence of the Stark shift on the plasma input power. The input power of the plasma ranging from 10 W to 90 W was increased in steps of 10 W and the value of the Stark shift was measured for each input power. In this set of experiments, the gas pressure was maintained constant at 4 Pa.

As Fig. 5.7 shows, the shift of the PL peak position of the QDs (on the sample) exposed to plasma with varying input powers represented by black circles. An increasing trend is observed in the value of the Stark shift as a function of input power. For the first point in the figure, the power was set to 10 W and the Stark shift of the PL peak position was measured to be 0.022 ± 0.002 nm. This value of the Stark shift gradually rises to the value of 0.073 ± 0.001 nm for a plasma
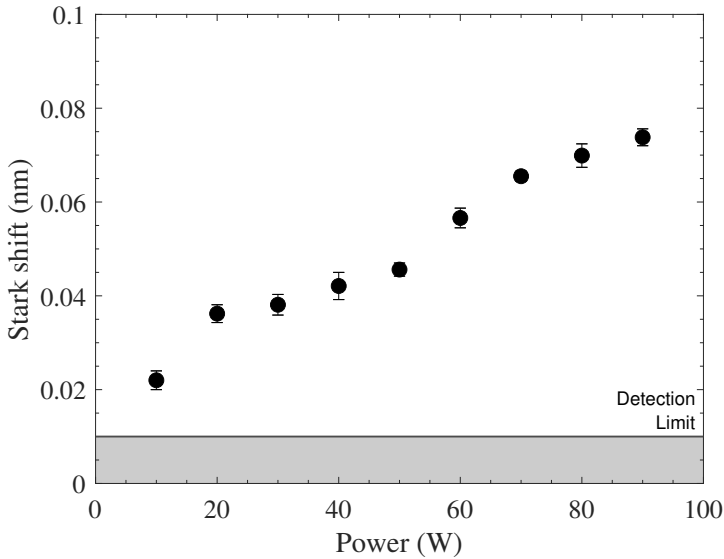
Figure 5.7: The amounts of Stark shift of the QDs' PL peak position measured as a function of plasma input power (black circles) at a constant pressure of 4 Pa. The detection limit of the current experimental scheme is 0.01 nm (shaded area).

input power of 90 W.

For further interpretation of the aforementioned results (i.e. the correlation between Stark shift values and input plasma powers), plasma parameters are measured for the respective conditions. The electron temperature and the floating potential are the two specific parameters illustrative for these plasma conditions. These results are shown in Appendix 5.B.

In the following section, the observed Stark shift in the PL peak position of the QDs will be interpreted using established theories.

5.4 Discussions

Multiple effects and phenomena were observed in the response of the QD PL spectra upon plasma exposure: I) a slow redshift of the PL peak position observed throughout long plasma exposure experiments, II) a fast shift during short plasma exposure experiments, and III) a dependence of the value of the fast redshift on the plasma input power.

First, the slow shift is attributed to the temperature effects of the plasma on the substrate and the QDs. As depicted in section 5.3.1, a monotonous redshift on

long timescales of tens of seconds is observed when the QD sample is immersed in the low-pressure plasma environment. Lattice dilation, i.e. thermal expansion of the crystal structure in the QDs lattice, is the contributing factor to the slow shift in PL peak position [52]. In literature, it has also been established that the energy band-gap of the bulk semiconductor is dependent on the temperature, which results in a shrinkage of the band-gap as the temperature rises [53]. Therefore, the PL peak position that represents the average energy gap of the QDs is subject to a shift towards longer wavelengths, i.e. lower photon energies. The sensitivity of the PL emission from the QDs on the temperature has been characterized as reversible and linear, a property which can - for instance - be utilized for optical-based temperature measurement sensors [92].

Concomitant with a monotonous redshift of the PL peak position, the integrated intensity of the PL peak is observed to decline with a similar linear trend on long-time scales. This decline in PL peak intensity is comprised of a recoverable and a non-recoverable part. The recoverable part is ascribed to temperature effects, whereas ion-induced effects play the main role in the non-recovery part of the PL peak intensity after plasma exposure. Accounting for the recoverable and reversible decline in the emission intensity, it has been documented that non-radiative processes are thermally activated as the QDs' temperature becomes elevated. This results in limited quantum efficiency in the QDs and therefore leads to a decreased PL intensity [53]. Carrier trapping in surface states and phonon-assisted thermal escape of photo-excited carriers from the QDs are the two non-radiative relaxation processes involved in the temperature-dependent decline of the PL intensity. There is, however, a rate of decline in the PL emission intensity, in addition to the one ascribed to thermal effects. This additional decline rate, characterized as nonrecoverable, is attributed to ion-induced effects. Plasma-exposed QDs are continuously bombarded by ions. Since in this case the QD material is damaged by ion bombardment, the decreased portion of PL intensity is non-reversible [85].

Additional to the slow shift of the PL peak position due to plasma heating, a fast shift of the PL peak position is observed and distinguished specifically for short plasma exposures. This fast shift is attributed to charging effects, i.e. to the electric fields generated by charged species, in this case, electrons, residing on the QD-coated substrate. The reason for the accumulation of electrons on the substrate, once it is immersed in plasma, is that the mobility of electrons is much higher compared to that of ions. At steady state surface charge density, the electron and ion fluxes towards the surface are balanced and this can only be achieved when the floating potential, V_f, is negative with respect to the surrounding plasma [25]. The electric field, induced by the surface electrons, will cause

the quantum-confined Stark effect (QCSE) [93–95] on the discrete quantum states of the QDs.

The electric-field-induced fast redshift ($\Delta\lambda$) is expressed as [51]:

$$\Delta\lambda = 0.03\lambda^2(hc)^{-1}\left(m_e{}^* + m_h{}^*\right)a^4\left(\frac{2\pi eE}{h}\right)^2, \qquad (5.2)$$

where e, h, a, $m_e{}^*$ and $m_h{}^*$ indicate the elementary charge, Planck's constant, the QD core radius, the electron's effective mass, and the hole's effective mass, respectively. Essentially, the QCSE is caused by modification of the electron and hole energies such that the resulting recombination energy becomes lower. This modification is induced by electric fields generated by excess charges near the QDs' surfaces. In this way, the electric field "pulls" the electron and hole to the opposite sides inside the QDs, leading to a reduction of the band gap and therefore to a redshift in the overall PL spectrum [18]. This redshift, called Stark shift, can be used for sensing surface charges in plasma.

Marvi *et al.* [85] proposed a model explaining quantitatively how the experimentally observed Stark shift is correlated to plasma charging of the floating surface. Using this *'discrete charge model'*, it was confirmed that the observed Stark shift of the PL peak position occurs mainly due to microscopic electric fields associated with electrons on the surface.

As the electrically floating substrate, with QDs, deposited on it, is immersed in the plasma, a sheath containing the electric field is formed around it. The average normal component of the plasma sheath electric field on the substrate surface is σ/ε_0, where σ is surface charge density. The local electric field is, however, subject to fluctuations. Therefore the actual value of the electric field sensed by the QDs is larger. The fluctuations are mainly due to the redistribution of electron configurations on the sample and the inherently discrete nature of the charge process [83, 96].

For further analysis and interpretation, we calculate statistics of the local electric field resulting from the surface charge by taking into account multiple random configurations of electrons on the surface at constant σ and evaluating the electric field at the position of a single point-like QD. The resulting Stark shift of the PL peak position caused by the microscopic electric field of each randomly dispersed configuration of electrons is then calculated using Equation 5.2. Typically, a few million random electron configurations are evaluated to calculate the statistics of the local electric field - with each configuration consisting of thousands of quasi-static electrons. The observed fast shift is measured over long (typically 0.76 s) measurement time and is therefore averaged over all electron configurations and radiation acts. It was shown [85, 86] that in this case the measured Stark shift -

δ_{mean} - would correspond to the average of the Stark shifts of all electron configurations. In other words, $\delta_{mean} = \Delta\lambda(E_{rms})$, where E_{rms} is the root-mean-square electric field averaged over all the electron configurations.

The discrete charge model allows the calculation of values of both the macroscopic electric field (E_{mac}) and the microscopic electric field (E_{mic}) caused by the electrons near the QD for a given σ. The microscopic electric field is typical, under our conditions, one order of magnitude larger than the macroscopic electric field. As an input to the model, first, the surface charge density σ is required to be calculated. For this purpose, the plasma sheath electric field (E_{sheath}) is estimated.

The sheath electric field is calculated assuming a quadratic potential drop profile across the sheath thickness, leading to a linearly increasing electric field [97] in the sheath from the bulk plasma towards the surface. Plasma parameters measured by the Langmuir probe are used to determine the potential drop and roughly estimate the sheath thickness using Child-Langmuir law for RF plasmas [98]. The sheath thickness estimations are cross-checked with camera images taken from the plasma sheath close to the substrate. The potential drop across the floating sheath of an RF plasma, also known as the floating potential under RF bias, is expressed as [23]:

$$V_{f_{RF}} = \frac{kT_e}{e}\left[\frac{1}{2}\ln\left(\frac{2\pi m_e}{M}\right) - \ln I_0\left(\frac{eV_1}{kT_e}\right)\right],\qquad(5.3)$$

where T_e, m_e, M, and V_1 are the electron temperature, electron mass, ion mass (in this case, argon), and the amplitude of the RF voltage across the sheath, respectively. Here, I_0 is the zero-order modified Bessel function. The first term on the right-hand-side of equation 5.3 represents the floating potential under DC conditions while the second term represents the RF self-bias. T_e is measured by the Langmuir probe. V_1, however, cannot be reliably measured for a floating electrode. Therefore, to obtain an absolute upper limit estimation of $V_{f_{RF}}$ (and corresponding E_{sheath}), we used the amplitude of the RF signal (U_{RF}) measured by an oscilloscope on the RF electrode. The actual value of $V_{f_{RF}}$ lies therefore between the DC floating potential measured by the Langmuir probe and the voltage obtained from equation 5.3 with $V_1 = U_{RF}$.

From the Langmuir probe measurements, the electron temperature is $T_e = 1.5$ eV $\pm$ 0.1 eV and the amplitude of the RF signal (measured by an oscilloscope) is $U_{RF} = 178$ V for 50 W plasma input power. Together with a sheath thickness of $d_s \approx 0.6$ *mm*, the plasma sheath electric field at the location of the substrate is approximated to be $E_{sheath} = 5.8 \times 10^5$ V/m, for the conditions explained in detail in section 5.3.3. Illustrated in Fig. 5.8 is a statistical evaluation of the

microscopic electric field that is yielded by the discrete charge model for the above-mentioned values and conditions of the plasma. In Fig. 5.8 (a), a histogram of the electric fields associated with 10^6 configurations of 3000 electrons on the surface, randomly distributed on a 10^{-10} m^{-2} square sample in the center of which a QD resides. A microscopic electric field of $E_{mic} = 6.8 \times 10^6$ V/m would consequently induce a Stark shift of the PL peak position of $\delta_{mean} = 0.05$ nm (Fig. 5.8 (b)). Also, as the corresponding Stark shift values in Fig. 5.8 (b) indicate, the macroscopic electric field would induce only a non-observable Stark shift of $\delta_{mac} = 3.4 \times 10^{-4}$ nm. Therefore, it is necessary to take into account the electric field fluctuations and the resulting microscopic electric field that is responsible for inducing the observed Stark shift.

Hence, the assumption that only the microscopic electric fields emanating from electrons in the proximity of QDs surfaces are responsible for inducing the observed Stark shift is founded.

The measured value of Stark shift of the PL peak position was 0.046 nm (see Fig. 5.6) for the conditions mentioned in section 5.3.3, whereas the calculated Stark shift according to the discrete charge model is $\delta_{mean} = 0.05$ nm (with Langmuir probe data as input). The calculated and measured values of Stark shift in this case are close to one another. However, their slight discrepancy may stem from the simplifications and estimations with respect to the measurements and calculations leading to E_{mac}.

The calculated Stark shift value of 0.05 nm is, however, the maximum value since the upper limit estimated $V_{f_{RF}}$ is used for calculating surface charge density used as the input for the discrete charge model results shown in Fig. 5.8. The same statistical calculations are performed assuming the absolute minimum for the floating potential (i.e. DC floating potential). In this case, the minimum δ_{mean} = 0.0034 nm would be one order of magnitude lower than in the case assuming the upper limit $V_{f_{RF}}$, resulting in the calculated Stark shift value to fall below the experimental detection limit of 0.01 nm. Hence, incorporating RF self-bias in $V_{f_{RF}}$ for estimation of the surface charge density is necessary.

As the Stark shift values are measured at different plasma input powers, the effect of the plasma conditions on the detected value of Stark shift is demonstrated (see section 5.3.4). It has been observed that the value of the Stark shift increases with the plasma input power (see Fig. 5.7). In order to study the effect of these plasma parameters on the charge of the surface, Langmuir probe measurements were performed for each respective measurement shown in Fig. 5.7. Subsequently, the plasma sheath electric field and the microscopic electric field are calculated using the discrete charge model for both upper and lower limits of $V_{f_{RF}}$. Finally, the minimum and maximum Stark shifts corresponding to those
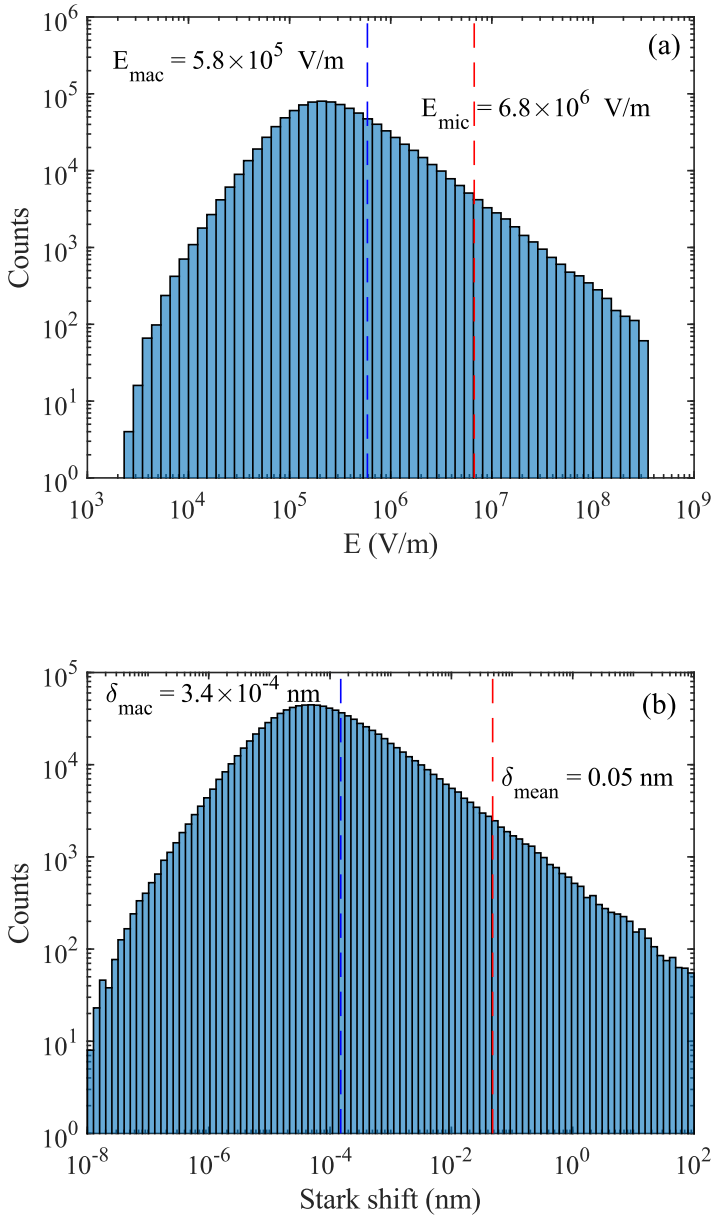
Figure 5.8: Statistical evaluation of the microscopic electric field E_{mic} at the location of a QD associated with quasi-stationary electrons on the substrate surface (a) and the corresponding histogram of QD photoluminescence Stark shifts (b). Over 10^6 different electron configurations are integrated for these evaluations.
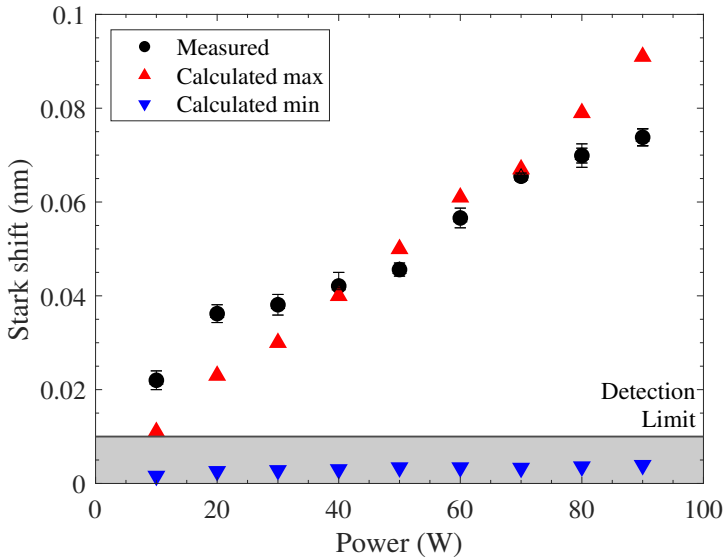
Figure 5.9: Maximum (red upward triangles) and minimum (blue downward triangles) calculated values of Stark shift based on the discrete charge model as a function of plasma input power at a constant pressure of 4 Pa together with the measured values of Stark shift (black circles). The minimum calculated values all fall under the experimental detection limit.

under each input power of the plasma are calculated. As illustrated in Fig. 5.9, the maxima and minima of the calculated values of Stark shifts are compared with the measured values as a function of plasma input power. The calculated minimal values of Stark shift, all falling below the detection limit, differ in one order of magnitude from the corresponding measured values. The experimental Stark shift values are close to the maximal calculated values suggesting that, in this particular case, the amplitude of the RF voltage between the floating substrate and surrounding plasma is close to U_{RF}.

The increasing trend in the value of Stark shift with increasing plasma input power of the plasma is confirmed by the calculations. As the input power is increased from 10 W to 90 W, the plasma sheath electric field is enhanced. This enhancement is mainly due to the increase in the amplitude of the RF voltage oscillations accelerating the electrons in the plasma. Consequently, more charge is induced on the surface and a larger number of electrons resides on the same surface area (i.e. more surface charge density). This trend as a function of plasma power is confirmed by the measurements of the floating potential by the Langmuir probe as can be seen in Fig. 5.10. The higher surface charge density leads to a

stronger microscopic electric field, which is increased from 3.29×10^6 V/m to 9.29×10^6 V/m when the plasma power is increased from 10 W to 90 W. This increase causes the calculated value of Stark shift to increase from 0.011 nm to 0.091 nm, a trend which is also clearly corresponding to the same upward trend in the measured values of Stark shift (see Fig. 5.9).

5.5 Conclusions

QDs, deposited on the surface of an electrically floating substrate, immersed in a low-pressure RF plasma, were used as nanometer-sized surface charge probes. In conclusion, the experiments have shown that:

- The fast (Stark) redshift of the PL peak position of the laser-excited QDs was caused by electric fields originating from electrons residing on the surface of the substrate.

- The previously designed discrete charged model [85] correctly calculated the electric field, typically 6.8×10^6 V/m, formed by the surface electrons and the associated Stark shift of 0.05 nm.

- Increased plasma input power led to an increased value of Stark shift, 0.073 nm, which was associated with increased surface charge density as a result of higher plasma input power of 90 W.

- The Stark shift of the PL of the QDs deposited on a plasma-facing surface was therefore capable of tracking the variations in the surface charge density.

The plasma parameters were measured by a commercial Langmuir probe and used to estimate plasma sheath electric fields and the values of Stark shifts by the discrete charge model. The uncertainty in the RF self-bias measurements led to calculating only the maximal and minimal possible values of Stark shifts. The experimentally measured values of the Stark shift were found to lie close to the maximal calculated values.

Appendices

5.A   Double skewed Voigt fitting

In this appendix, the derivation of the double skewed Voigt distribution function is explained in detail. A Voigt distribution function, or a Voigt profile, is a convolution of a Gaussian and a Lorentzian distribution.

Since the acquired data had an asymmetrical component, the Voigt profile was modified, accordingly, to be a combination of a skewed Gaussian distribution and a skewed Lorentzian distribution, resulting in a double skewed Voigt distribution as used to analyze the data in this chapter. This double skewed Voigt distribution had the form:

$$\phi_V(x) = 2(1-\eta)\phi_G(x)\Phi_G(a_G x) + 2\eta\,\phi_L(x)\Phi_L(a_L x). \tag{5.4}$$

The Gaussian probability density function around the mean μ with variance σ^2 is expressed as:

$$\phi_G(x) = \frac{1}{\sigma\sqrt{2\pi}} e^{-\frac{1}{2}(\frac{x-\mu}{\sigma})^2}, \tag{5.5}$$

and the cumulative distribution function belonging to this Gaussian probability density function is:

$$\Phi_G(x) = \frac{1}{2}\left[1 + erf\left(\frac{x-\mu}{\sigma\sqrt{2}}\right)\right]. \tag{5.6}$$

Here, $erf\left(\frac{x-\mu}{\sigma\sqrt{2}}\right)$ is the Gauss error function defined as:

$$erf(z) = \frac{2}{\sqrt{\pi}}\int_0^z e^{-t^2}\,dt. \tag{5.7}$$

The probability density function of a skewed Gaussian distribution with skew parameter a_G is then given by:

$$f_G(x) = 2\phi_G(x)\Phi_G(a_g x). \tag{5.8}$$

When $a_G = 0$, the function is equal to a regular Gaussian distribution, whereas for $a_G > 0$ and $a_G < 0$ the distribution is skewed towards the right and left, respectively.
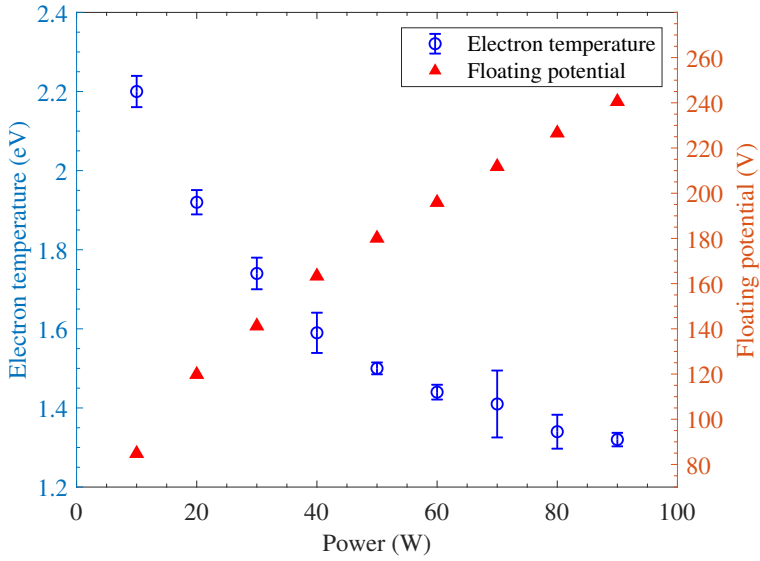
Figure 5.10: Electron temperature (T_e, blue circles, left axis) and the floating potential ($V_{f_{RF}}$, red triangles, right axis) as a function of input power. The gas pressure is set at 4 Pa.

The same procedure is used for a Lorentzian distribution with a probability density function:

$$\phi_L(x) = \frac{1}{\pi\gamma\left[1 + \left(\frac{x-\mu}{\gamma}\right)^2\right]}, \qquad (5.9)$$

where μ is the location parameter, specifying the location of the peak, and γ is the scale parameter equal to the FWHM of the Lorentzian distribution function.

The cumulative distribution function of the Lorentzian distribution function is:

$$\Phi_L(x) = \frac{1}{\pi}\arctan\left(\frac{x-\mu}{\gamma}\right) + \frac{1}{2}. \qquad (5.10)$$

Multiplying the probability density function with the cumulative distribution function results in the skewed Lorentzian distribution function with skew parameter a_L:

$$f_L(x) = 2\phi_L(x)\Phi_L(\alpha_L x). \qquad (5.11)$$

These skewed Gaussian and Lorentzian distributions can be combined with weight factor η to find the double skewed Voigt distribution of equation 5.1 or in abbreviated form:

$$\phi_V(x) = (1 - \eta)f_G(x) + \eta f_L(x). \tag{5.12}$$

5.B The Electron temperature and the floating potential

The electron temperature (T_e) and the floating potential under RF bias ($V_{f_{RF}}$) are measured and calculated using the data from the Langmuir probe and equation 5.3 for the same values of plasma parameters (i.e. input power and gas pressure) discussed in this chapter. As illustrated in Figure 5.10, the electron temperature follows a downward trend, starting from T_e = 2.2 eV for input power of 10 W and descending to T_e = 1.32 eV for 90 W; whereas the floating potential almost linearly increases from $V_{f_{RF}}$ = 84 V for 10 W to $V_{f_{RF}}$ = 240 V for 90 W of input power. The gas pressure is kept constant at 4 Pa throughout these measurements.

These values and their respective trends as a function of input power and gas pressure of the plasma are essential for the estimation of the plasma sheath electric field (E_{sheath}) and interpretation of the results regarding Stark shift values in the same plasma conditions.

Chapter 6

Laser-induced photodetachment to probe negative ions in oxygen plasma afterglow

Abstract

Time-resolved laser-induced photodetachment in concert with microwave cavity resonance spectroscopy is further developed and improved. The method is applied to measure – with microsecond time resolution – the decaying density of negative oxygen ions (O^-, O_2^- and O_3^-) and that of free electrons in the afterglow of a pulsed capacitively coupled radiofrequency driven oxygen plasma. The afterglow behavior of electrons shows a significant dependence on the gas pressure between 3 Pa and 6 Pa. For a pressure of 3 Pa, at which the plasma is in the so-called γ-mode, the decay of the negative ion density is slower than that of the electron density, eventually leading to the occurrence of a negative-ion-positive-ion plasma. At a slightly elevated pressure of 6 Pa (and higher), the plasma has transited into the so-called α-mode, in which a short period of increased electron density is detected just after switching off the plasma. In the α-mode, the negative ion and electron densities decay on similar time scales, leading to the trapping of negative ions. In this pressure range, the decay of the additional electron density released by the photodetachment of negative ions occurs following two distinct time scales. However, for increasingly elevated pressures above 10 Pa, the photodetachment signal is characterized to decay with an undershoot which may indicate a temporary local disturbance of the plasma's quasi-neutrality in the volume irradiated by the laser beam.

6.1 Introduction

Dynamics of electronegative plasmas have been the subject of interest during the recent decades [99–102]. In such electronegative plasmas, negative ions (often called anions) reside beside the positive ions, electrons, and different neutral species like metastables and reactive radicals. Such negative ions may be formed due to a significant electron affinity of some specific gaseous species. For instance, in the case of an oxygen plasma - as is under investigation in this chapter - oxygen atoms (O) and oxygen-based molecules (O_2, O_3) can turn into negative ions such as O^-, O_2^- and O_3^- upon attachment of a free electron from the plasma. Dependent on the experimental configuration and the discharge parameters, the number of free electrons might become suppressed significantly by these attachment processes. This, of course, strongly impacts the overall plasma dynamics.

Oxygen-containing plasmas have been of particular technological importance for decades, mainly due to the presence of negative ions, ozone, and a multitude of exciting species. Applications of oxygen plasmas include oxidation of silicon in the semiconductor industry [103], surface cleaning [104], etching of organic polymers [105, 106] and amorphous carbon films [107] as well as treatment of polymers and polymer composites [108] on industrial scales. The role of oxygen negative ions, particularly, in plasma chemistry and plasma-surface processing has been studied extensively for such potential applications [27, 109]; highlighting negative ion formation in near-surface and sheath regions.

These potential applications and the compounded complexity of electronegative plasmas [110–112] require diagnostic tools to investigate the formation and destruction mechanisms of negative ions in order to comprehend and model their dynamics under various conditions. An array of diagnostic techniques has so far been proposed and developed to detect, measure the density and investigate the dynamics of electrons and negative ions in plasmas [113]. Besides the role of free electrons on the overall dynamics of negative ions, diagnostic methods of negative ions are in some cases dependent on the determination of the electron density.

Langmuir probes have been used as diagnostic tools for negative ions [114]. Nonetheless, the probes' intrusiveness and their contamination create additional obstacles when operated in chemically reactive discharges. Mass spectrometry [115] is another diagnostic that has been used to probe negative ions. However, in this method, the trapping of negative ions in the positive plasma glow complexifies their extraction and subsequent detection. In addition, laser-induced photodetachment (LIP) has been developed and implemented as a diagnostic tool for various cases of electronegative plasmas [116]. To obtain absolute values

for negative ion densities, several different probes have been combined with the LIP technique, including Langmuir probes [117, 118], resonance hairpin probes [119], microwave interferometry [120] and microwave resonant cavities [99].

The dynamics of negative ions have been investigated in various plasma configurations and conditions. For instance, spatial profiles of negative ions in low-pressure oxygen discharges have been provided by Stoffels *et al.* [99]. In that work, the densities of oxygen negative ions at different gas pressures, input gas flows, and plasma powers were measured and compared to a kinetic model. In addition, (axial) negative ions (profiles) in oxygen [121] as well as in CCl_2F_2, C_2H_2 [60] and aniline argon radiofrequency (RF) discharges [8] were provided, while temporally resolved negative ion and electron densities during the afterglow of a CF_4 RF plasma were determined by Kono *et al.* [122]. Moreover, negative ion and electron densities have been probed in a time-resolved fashion in the afterglow of oxygen and hydrogen containing RF plasmas driven in both a capacitively coupled (CC) [123] and an inductively coupled (IC) [124] manner. For instance, LIP in concert with microwave interferometry was used in a pulsed CC-RF [125] and in the afterglow of an IC-RF [126] plasma by Küllig *et al.*. In that work, it was shown that the electronegativity $\alpha = n_-/n_e$ (with n_- and n_e being the negative ion density and the electron density respectively) of the plasma was a function of the gas pressure and the plasma input power. Also, a significant momentary release of electrons during the afterglow in a highly electronegative mode was observed. For all of the aforementioned measurements which were based on the microwave interferometry technique, the lowest electron density detection limit was in the order of 10^{14} (m^{-3}), rendering a lower detection limit for the negative ion densities in the order of 10^{15} (m^{-3}).

In this chapter, an experimental investigation of the temporal evolution of the densities of different oxygen anions and electrons in the afterglow of a capacitively coupled pulsed RF oxygen plasma is presented. For this purpose, laser-induced photodetachment in concert with microwave cavity resonance spectroscopy has been further developed and employed with 50 ns time resolution. Essential in the currently presented work is that the detection limit for negative ions has been improved by three orders of magnitude - i.e. to the order of 10^{12} (m^{-3}) - compared to previously published works. This is achieved by increasing the stability of the laser beam energy, optimizing the microwave cavity resonant method, and averaging many LIP events. As a result of the enhanced detection accuracy, negative ions could be detected on prolonged time scales up to 5.5 ms in the afterglow. This enabled us to distinguish between two distinct behaviors of the afterglow phase predicted only numerically in literature [30, 32]; the occur-

rence of a negative-ion-positive-ion plasma afterglow in the low electronegative
mode, and the sudden release of secondary electrons by the afterglow in the high
electronegative mode which results in self-trapping of negative ions.

The current chapter is organized as follows. First, the experimental meth-
ods, the setup, and the data-acquisition hardware are explained in detail in sec-
tion 6.2.In the following section 6.3, structured time-resolved measurements of
the electron density and the relevant negative ion densities in steady-state plasma
operation as well as in the afterglow plasma phase are presented. Especially the
variation in the gas pressure enabled us to distinguish between a low electroneg-
ative mode and a high electronegative mode. Finally, section 6.4 summarizes and
concludes the presented work.

6.2 Experimental methods

The experiments in this chapter are performed using MCRS and LIP diagnostic
techniques. The principles and theories of these techniques are explained thor-
oughly in chapter 3. The experimental setup used for the experiments of this
chapter is described in detail in chapter 4. The overall experimental conditions
used throughout this chapter are briefly mentioned below.

Regarding the measurements performed using MCRS, the time resolution
with which changes in the electron density can be detected using MCRS is lim-
ited by the fundamental response time τ_{fund} of the used cavity which depends on
the resonance frequency f_0 and the quality factor Q of the used resonant mode
($\tau_{fund} \propto Q/f_0$). The quality factor of a resonance peak is determined with the:

$$Q \equiv \frac{f_0}{\Gamma}.$$
(6.1)

Where Γ is the Full-Width-at-Half-Maximum (FWHM) of the resonance peak.
For the experiments presented in this work, $f_0 = 1.3665$ GHz and $\Gamma \approx 5.91$ MHz
which amounts to $Q = 231$, and hence, the time resolution was ≈ 50 ns.

While the subsequent experiments have been performed with the gas pressure
as a variable, all other plasma and process parameters were kept constant. The
pulse frequency of the plasma was set to 5 Hz, corresponding to the repetition
rate of the used laser system, with a duty cycle of 50%. The plasma input power
was set to 15 W for all experiments and the oxygen input flow was kept constant
at 4 SCCM.
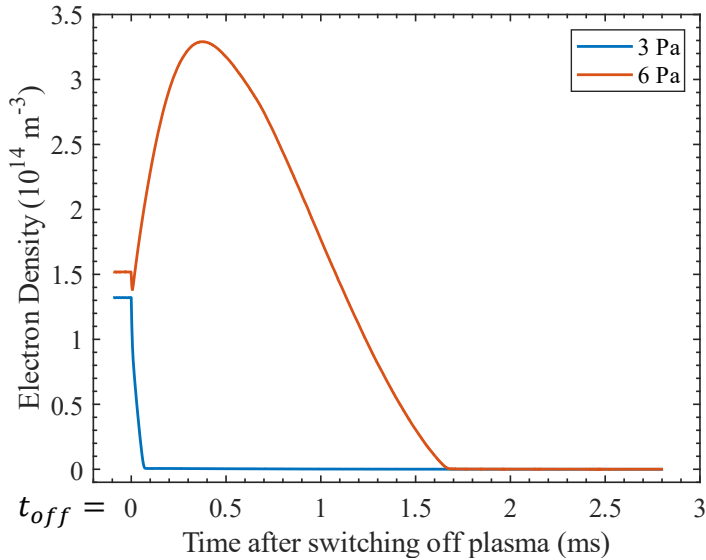
Figure 6.1: Temporal behavior of the electron density during the afterglow phase at a pressure of 3 Pa (blue curve) and 6 Pa (red curve).

6.3 Results and Discussions

In order to get maximum insight into the behavior of anions in the afterglow of the investigated low-pressure oxygen pulsed RF discharge, the following experiments have been conducted. In the first set of experiments, presented in section 6.3.1, the electron density has been measured with a high temporal resolution during the full afterglow phase and at two different gas pressures, i.e. at 3 Pa and at 6 Pa, chosen such that the difference between the low electronegative mode and the high electronegative mode is clearly demonstrated experimentally. In the second set of experiments, presented in section 6.3.2, overall photodetachment signals (at 532 nm) are measured during steady-state operation and during the afterglow phase of the same discharge at 6 Pa and at an elevated pressure of 25 Pa. In the third set of experiments, presented in section 6.3.3, the densities of distinct anion species during the afterglow phase have been portrayed. In this section, these measurements are subsequently linked to the presented electron density measurements in section 6.3.1.

6.3.1   Electron density measurements

First, the temporal behavior of the electron density during the afterglow phase is measured using MCRS (in TM_{010} mode) only. The used microwave mode is most sensitive in the central regions (see Figure 3.3) in the cylindrical cavity whereas the plasma sheath is mainly near the circumferential walls of the cavity; therefore, the effect of the sheath and sheath variations due to a change of pressure on the electron density measurements are considered marginal. Figure 6.1 (blue curve) shows the afterglow decay at a pressure of 3 Pa. In this situation, the decay of the electron density begins at the moment the RF pulse falls ($t = t_{off}$) and is dominated by plasma diffusion to and recombination at the plasma-containing walls, i.e. the resonant cavity walls. At these low pressures, the influence of volume recombination is negligible. Clearly, at a pressure of 3 Pa, the afterglow is comprised of one single stage during which the electron density decays rapidly. Negative ions densities decrease relatively slower as will be observed from experiments presented later in this chapter (Figures 6.6 and 6.8).

However, as illustrated in Figure 6.1 (red curve), the afterglow at a slightly increased pressure of 6 Pa (and higher) behaves significantly differently, featuring a rampant release of electrons. Initially, right after switching off the plasma, the electron density shows a minor and brief drop, which is normally due to a decrease in the electron temperature as the main result termination of ionization events. Afterward, a rapid release of electrons in the cavity volume causes the electron density to even exceed its value during steady-state plasma operation ($t < t_{off}$) for a short period of time. Finally, an exponential decay similar to the former case - but much slower - is observed.

The appearance of this temporal rise of the electron density in the afterglow phase is attributed to the detachment of - mainly - negative atomic oxygen ions O^-. As models by Brockhaus et $al.$ [28] and Küllig et $al.$ [125] suggest, the most important production channel for electrons in this phase is the detachment of electrons from negative ions by collisions with atomic oxygen O, with ground state molecular oxygen $O_2(X^3\Sigma_g^-)$ or with metastable oxygen molecules $O_2(a^1\Delta_g)$.

Under steady-state plasma operation, there is a balance between the production and the loss channels of electrons. Besides the traditional loss channels such as those at the plasma-confining walls, electron losses are mainly due to the formation of negative ions through dissociative electron attachment, while electron production mainly occurs - besides ionization events - via associative electron detachment of negative ions. As will be observed later in this chapter, the densities of the negative ions begin to fall simultaneously with the start of electron detachment (Figures 6.7 and 6.9).

Upon switching off the plasma, in the case of the measurements in Figure 6.1 (red curve), this balance is countered towards the side of electron production since a lower temperature of the electrons leads to suppression of the electron loss reactions (electron attachment forming negative ions) while maintaining the production of them through detachment processes. This consequently culminates in a net electron release at the beginning of the afterglow phase.

Upon switching off the plasma, dependent on the pressure, two distinct situations can be observed as becomes obvious from Figure 6.1.

At relatively low pressures, i.e. at 3 Pa in the case of the measurement in Figure 6.1 (blue curve), the electron loss mechanisms (i.e. electron attachment forming negative ions in combination with traditional diffusive plasma decay) in the plasma afterglow dominate over the electron production mechanism (i.e. electron detachment from negative ions). This situation is represented in Figure 6.1 by one distinct phase of electron depletion during the full afterglow phase. This "mode" is often called the low electronegative mode or the γ-mode.

At slightly higher pressures, i.e. at 6 Pa in the case of the measurement in Figure 6.1, in the first part of the afterglow phase, the electron production mechanism (i.e. electron detachment from negative ions) dominates over the electron loss mechanisms (i.e. electron attachment forming negative ions in combination with traditional diffusive plasma decay). This situation is represented in Figure 6.1 (red curve) - after an initial brief and minor decrease of the electron density - by a period of electron density increase after which the electron density depletes eventually. This "mode" is often called the high electronegative mode or the α-mode.

Under the current plasma and process conditions, the transition from γ-mode to α-mode was found to occur at a gas pressure of 4 Pa in the direction of increasing pressure. With this we report the experimental verification of this transition which was already predicted before by numerical simulations [30, 32]. Investigation of the role of sheath parameters or positive and negative ion Bohm velocities in the decay of the electron density would require extensive modeling to retrieve accurate results. Therefore, this effect has been omitted in the analyses since this chapter was mainly focused on the experimental measurement of the densities of electrons and negative ions.

6.3.2 Photodetachment signals from steady-state plasma and its afterglow

In this section, we present 'bare' MCRS measurements displaying the effect of LIP on the overall electron density and the response of the plasma to that. Section

B.1 reports on the results for steady-state plasma operation conditions while section B.2 reports on similar results in the plasma afterglow phase. All experiments have been performed under the same plasma and process conditions as mentioned in the previous sections with - again - the value of the gas pressure as a variable.

Photodetachment signal during steady state plasma operation

The LIP incident and the subsequent plasma response to that during steady-state plasma operation are monitored using MCRS. The electron density before, during, and after the laser was shot through the cavity is displayed in Figure 6.2 for two different values (6 Pa and 25 Pa) of the gas pressure.

In these graphs, several distinct stages can be identified. For both pressures, the first stage represents a steep rise in the electron density corresponding to the (almost) instantaneous photodetachment of electrons from the negative oxygen ions. Since the photon energy corresponding to the used laser wavelength of 532 nm exceeds the threshold energy for photodetachment of O^-, O_2^- and O_3^- ions, photodetachment of all three ions contribute to the measured value of the additional electron density Δn_e, which is determined via Equation 3.16.

Following the sudden rise in electron density there is a subsequent decay of Δn_e, eventually reaching the same electron density value as just before the LIP incident took place. This decay, for the case of the relatively low pressure of 6 Pa, appears to occur through two distinct decay time scales (τ_1 and τ_2) (see Figure 6.2-a). The first time scale, τ_1, can be attributed to the photodetached electrons swiftly diffusing out to the adjacent electronegative plasma as a reaction to the sudden local increase in electron density in the volume irradiated by the laser. In other words, the photodetached electrons redistribute over the cavity volume. From a macroscopic point of view, the photodetached electrons redistribute to regions where they are probed to a lesser extent by MCRS since the electric fields of the resonant TM_{010} mode are lower in the outer regions of the cavity. Hence, this leads to a net decrease in the detected signal. The second time scale, τ_2, can be attributed to the (re)formation of negative ions in the laser-irradiated volume. Steady-state plasma conditions demand a certain level of negative ion density which has been disturbed by the LIP incident. Recovering this balance by (re)attachment consumes electrons. After both time scales (τ_1 and τ_2) the plasma has been restored to its original steady state. The different threshold energies for photodetachment of O^-, O_2^- and O_3^- ions lead to different temperatures of photodetached electrons gained from the same photon energy. However, this temperature difference could not cause the observed two distinct decay times of τ_1 and τ_2 since the photodetachment signal obtained with 1064 nm of laser
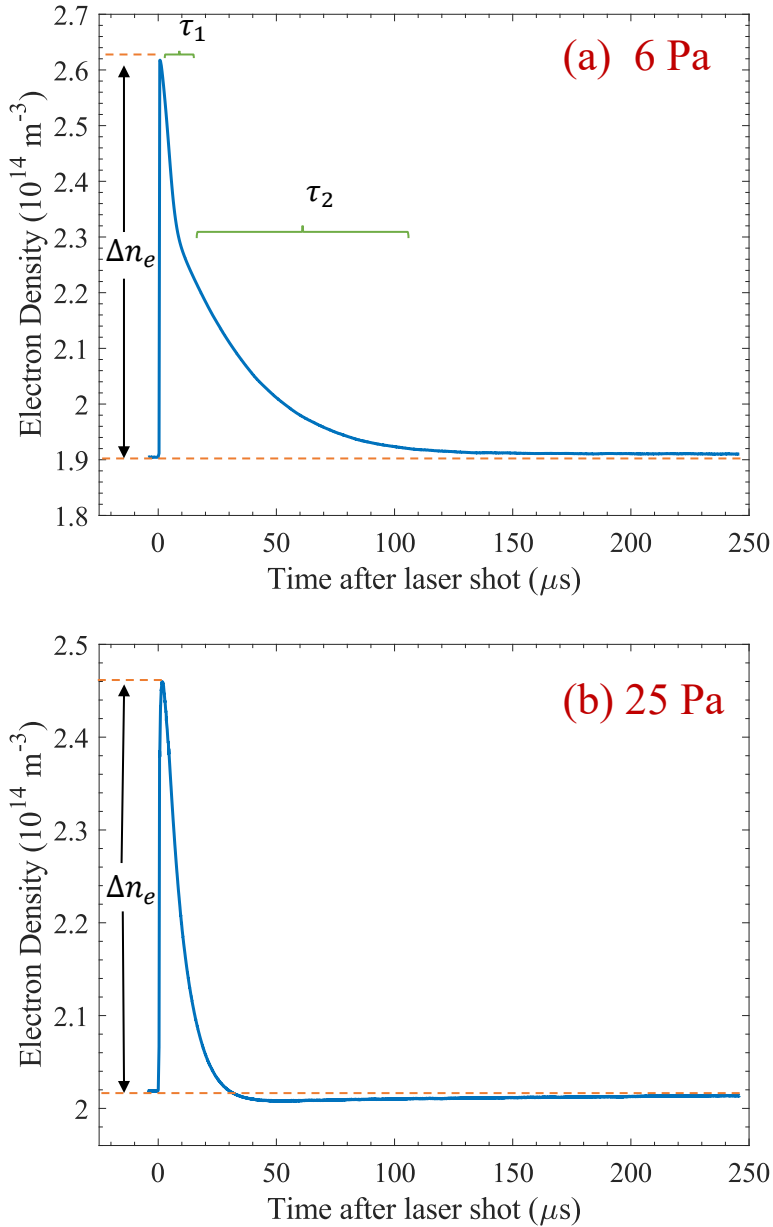
Figure 6.2: Photodetachment signals: responses of the steady-state plasma operating at (a) 6 Pa and (b) 25 Pa to a LIP incident. Each signal is comprised of several distinct stages.

wavelength (i.e. exceeding the threshold energy of only O_2^-) contains the same two distinct decay times.

For the case of a higher gas pressure, i.e. 25 Pa (see Figure 6.2-b), especially the second time scale, τ_2, becomes shorter and - at most - comparable to τ_1. The decrease of τ_2 can be explained by the increased reaction rate k_{att} for electron attachment scaling linearly with the background gas density $n_{neutral}$ (and thus - at a constant temperature - also with the background gas pressure):

$$k_{att} = \sigma_{att} n_e n_{neutral}. \tag{6.2}$$

Here, σ_{att} is the electron attachment cross-section. Hence, at elevated pressures, the plasma restores quicker to its initial steady state as can be concluded when comparing Figures 6.2-a and 6.2-b. The density of neutral O_2 is reported to be 10^{20} (m^{-3}) and 6×10^{20} (m^{-3}) in 6 Pa and 25 Pa gas pressure respectively [99]. Assuming that dissociative attachment reactions to O_2 are dominant, this would lead to 6 times higher electron attachment rate in 25 Pa plasma operation (compared to the situation in 6 Pa), therefore resulting in the decrease of the second time scale τ_2.

Additionally, for the case of 25 Pa, a slight undershoot of the electron density is observed before it finally reaches its initial steady state value before the LIP event. This undershoot can most likely be ascribed to a local disturbance of the plasma's quasi-neutrality due to the initiation of a potential barrier in the laser irradiated volume [127, 128].

The photodetachment signals obtained using a laser wavelength of 1064 nm, i.e. only O_2^- contributes to the additional electron density Δn_e, verifiably agrees with measurements illustrated at Figure 6.2. The decay of the photodetached electrons also occurs through two distinct decay time scales for the case of a relatively lower pressure of 6 Pa, as well as the shorter decay time of the photodetached electrons associated with the case of a higher gas pressure of 25 Pa.

Photodetachment signal during the plasma afterglow

Whereas the measurements presented in the previous section were performed under steady-state plasma conditions, the upcoming measurements in this subsection are conducted during the afterglow phase of the same plasma. As illustrated in Figure 6.3, in this case, the laser pulse was triggered to irradiate the afterglow at specific moments in time. This is to enable the detection of negative ions throughout the decaying afterglow phase. In Figure 6.3, these LIP events are conveyed as electron density peaks. For reference, $t = t_{off}$ indicates the moment
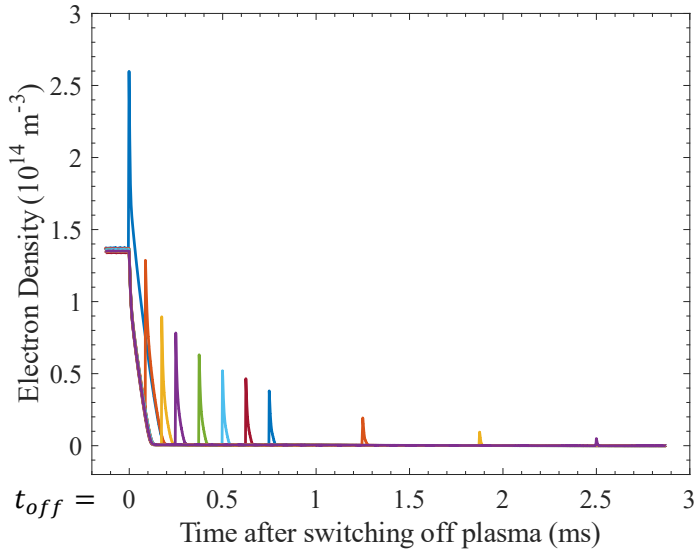
Figure 6.3: Photodetachment signals during the afterglow phase with each peak representing one averaged set of LIP incidents at a specific time delay after the plasma was switched off.

in time at which the RF power was switched off, marking the beginning of the afterglow phase.

The gradual decrease of the photodetached electron density as a function of time through the afterglow phase was already apparent, implying the afterglow behavior of the negative ions. However, remarkably, photodetached electrons ($\approx$1-5$\times 10^{13}$ m^{-3}) are detected even though the electron density (for reference plotted in the same graph) has already depleted for a considerable amount of time. This indicates much longer decay constants associated with negative ions than those associated with electrons.

6.3.3 Negative ion density measurements during the plasma afterglow

In the previous sections, we measured the electron density using MCRS and the change thereof upon LIP events. This section presents a structured set of measurements in which the absolute values of negative ions are probed during the afterglow of the oxygen plasma under investigation. Application of two wavelengths for laser irradiation - i.e. 532 nm and 1064 nm - enabled to distinguish
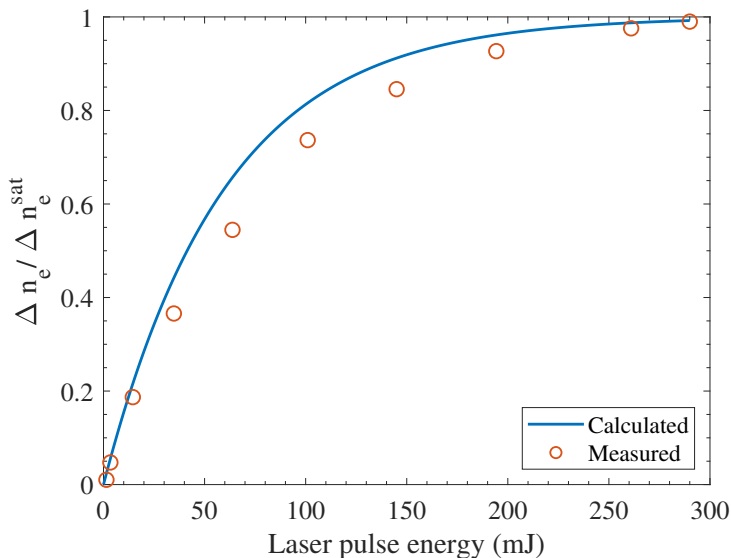
Figure 6.4: The fraction between the photodetached electron density (Δn_e) at each applied laser pulse energy and the photodetached electron density in the saturation regime (Δn_e^{sat}) when the laser operates at 532 nm, including the measured (red circles) and calculated values (blue curve) used for fitting. The error in the measurements is less than 1.5%, smaller than the red circles in the figure. Photodetachment cross sections for O^- are used for this calculation.

the individual contribution of O_2^- to the total negative ion density. It should be recalled (see section 3.3) that O^- is expected to be the dominant ion while the contribution of O_3^- to the total negative ion density is less than 1%.

In the presented measurements, the first 532 nm laser light is applied in order to convert all the negative ions residing in the laser beam volume. Initially, it has been examined whether the saturation regime - that means conversion of all negative ions in laser beam volume - is achieved. For this purpose, α - i.e. the fraction between the photodetached electron density (Δn_e) at each laser pulse energy and the photodeached electron density in the saturation regime (Δn_e^{sat}) - is determined using equation 3.17. Figure 6.4 illustrates the calculated and measured values of α as a function of laser pulse energy, with the laser operating at 532 nm wavelength. As can be seen from Figure 6.4, near-saturation can be reached when the laser pulse is set to $E_{laser} = 291$ mJ, meaning that in this case nearly all ($\alpha = 0.99$) of the negative ions within the laser beam are converted into pairs of neutrals and free electrons. The determined values, as observed in Figure 6.4, follow an exponential trend towards saturation regardless of the fact that only
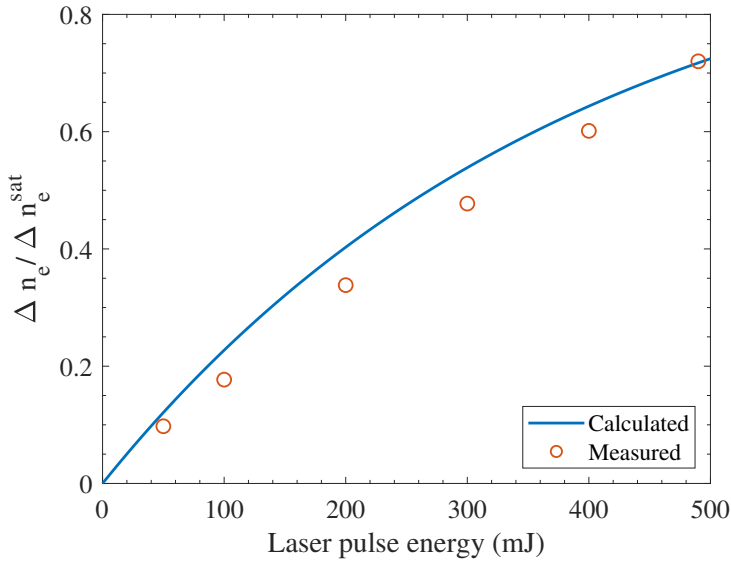
Figure 6.5: The fraction between the photodetached electron density (Δn_e) at each applied laser pulse energy and the photodetached electron density in the saturation regime (Δn_e^{sat}) when the laser operates at 1064 nm, including the measured (red circles) and calculated values (blue curve). Photodetachment cross sections for O_2^- are used for this calculation.

the O^- cross section is used for calculation (blue line), indicating the fact that the majority of the negative ions consists of O^- ions. Therefore, in this case, to derive absolute values of negative ions density one primarily has to correct for the ratio between cavity volume and the laser beam volume, weighted with the electric field of the used microwave mode (see equation 3.16).

The individual contribution of O_2^- ions to the total negative ion density is determined when the 1064 nm laser light is applied. In this case, the maximum laser pulse energy that the laser yields is 490 mJ, which is not capable of saturating the photodetachment signal. This incapability is due to the significantly smaller photodetachment cross section of O_2^- at 1064 nm. According to equation 3.17 - filling in the photodetachment cross section and the electron binding energy of O_2^- - the fraction α for the maximum laser pulse energy is $\alpha = 0.72$. Figure 6.5 demonstrates measured values of α as a function of laser pulse energy when the laser operates at 1064 nm. In conclusion, applying 490 mJ laser pulse energy at 1064 nm enabled photodetach 72% of the total O_2^- in the laser beam volume. Therefore, the measured photodetachment signal is corrected with α besides the correction for the laser beam volume.

The error associated with the measurements of the negative ions' densities stems from both the instability of the laser pulse energy through successive irradiation of the plasma and the error in the determination of the electron density using MCRS. In order to enhance the accuracy of the negative ion density measurements, first the laser pulse energy is stabilized during the time required for each set of LIP measurements. The laser pulse energies used for each LIP trial are accurate within a standard deviation of $\sigma_{SD} < 1.5\%$. A technique of averaging through successive MCRS measurements and strict control of plasma parameters (e.g. gas pressure) is used for obtaining accurate electron density values. The lower detection limit for the electron density, with this technique, is 10^{10} m^{-3}. This detection limit in the electron density measurement translates to a limit of 10^{12} m^{-3} in negative ion density detection.

O^- plus O_3^- negative ion density

Absolute values of the total negative ion density excluding O_2^- - i.e. O^- plus O_3^- - are measured temporally resolved during the afterglow phase of the oxygen plasma. To compare the afterglow behaviors of the two previously elaborated modes of plasma operation, electron, and negative ion densities are illustrated in Figure 6.6 (γ-mode) and Figure 6.7 (α-mode). A one-term exponential decay fit (shown in the figures with a red line) assists in calculating the time (τ) required for the negative ion density to reach $\frac{1}{e}$ of its initial value - i.e. the decay time - besides illustrating its decay behavior.

Figure 6.6 conveys obtained negative ions (O^- plus O_3^-) and electron densities during the afterglow phase at a pressure of 3 Pa, hence operation in γ-mode. In this case, the electron density decays to zero within approximately 75 μs, as already discussed in section 6.3.1. Negative ion densities are measured with initially 10 μs time steps which are gradually prolonged up to 500 μs. This provided sufficient time resolution since during the first 200 μs of the afterglow phase the negative ion density decreased rapidly, followed by a decrease at a slower rate. The enhanced detection accuracy has enabled negative ion density measurements during extended times scales in the afterglow. At the moment of the first LIP incident, the negative ion (O^- plus O_3^-) density is measured to be $n_- = 6.05 \times 10^{15}$ m^{-3}. Eventually it falls three orders of magnitude to $n_- = 2.36 \times 10^{12}$ m^{-3} after 5.5 ms. According to the exponential fit, the negative ion density decay time is calculated to be $\tau \approx 504$ μs, a value remarkably longer than the electron density decay time.

The same set of measurements is performed at a pressure of 6 Pa (Figure 6.7), i.e. operation in α-mode. In this case, the electron density during the afterglow

Figure 6.6: Time-resolved electron density (blue curve) together with the combined O^- plus O_3^- negative ions density (circles) during the afterglow phase operating at a pressure of 3 Pa (γ-mode). The negative ion density decay is fitted with a one-term exponential fit (red curve).
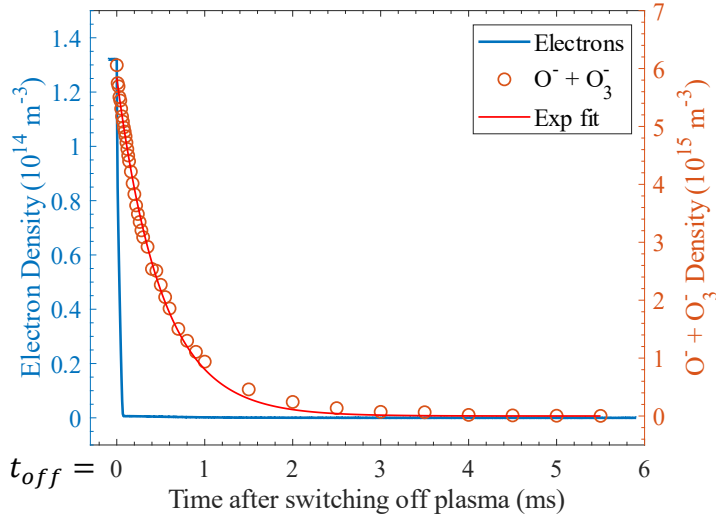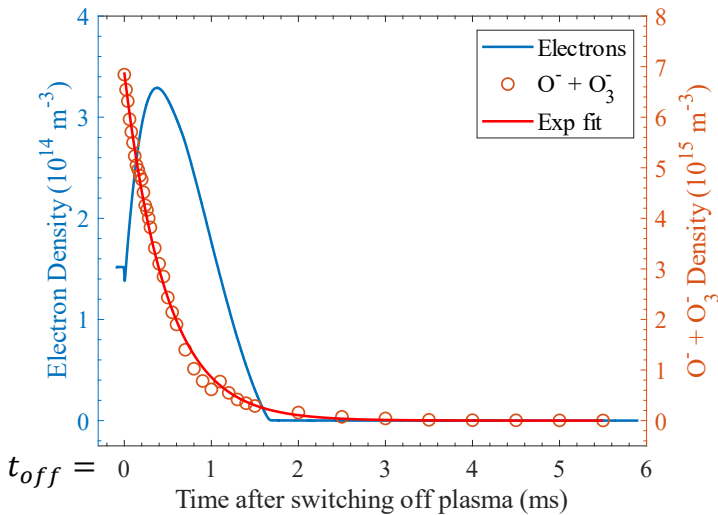

Figure 6.7: Time-resolved electron density (blue curve) together with the combined O^- plus O_3^- negative ions density (circles) during the afterglow phase operating at a pressure of 6 Pa (α-mode). The negative ion density decay is fitted with a one-term exponential fit (red curve).

behaves differently, featuring a rampant release of electrons (as already discussed and explained in section 6.3.1). The overall decay time associated with electrons in this mode (about 1.65 ms) is much longer due to the net release of electrons at the beginning of the afterglow phase. The decay behavior of the (O^- plus O_3^-) negative ions density, nevertheless, is almost identical to the γ-mode situation except for a slightly shorter decay time of $\tau \approx 480~\mu$s compared to the previous case.

An oxygen plasma (due to its electronegativity) is stratified into a core, where almost all negative ions are trapped, surrounded by an electropositive region consisting of positive ions and electrons [129–131] during the plasma-on phase. During the afterglow phase, however, two distinct scenarios based on the operation mode of the plasma may occur:

- In the γ-mode, when the electron density decays almost instantly after the RF power is cut, negative ions reside for a much longer period of time in the former discharge region. Initially, the electrons at the edge of the plasma rapidly diffuse toward the plasma-containing walls due to their higher mobility. With the electron density having decayed entirely after the first 75 μs of the afterglow phase, the plasma is depleted of electrons. The paucity of free electrons and residence of negative ions in the later afterglow means a transition to a negative-ion-positive-ion plasma has occurred. Moreover, the sheath voltage as well as the ambipolar electrostatic fields, trapping negative ions in the core of the cavity, collapse due to loss of electrons [132]. This behavior is predicted only numerically in models laid out by Kaganovich *et al.* [30, 32]. In such a case of negative-ion-positive-ion plasma, according to the models, the negative-ion flux to the plasma-containing walls increases phenomenally, consequently raising the possibility of negative ion extraction in the afterglow.

- In the latter case of the α-mode, however, electrons reside in the afterglow phase for an extended period of time as well. As a result, the occurrence of a negative-ion-positive-ion plasma is prevented by the release of secondary electrons. Besides, the temporal rise of the electron density causes the electrostatic fields to build up in the core as well as in the electropositive edge of the plasma; as a result, negative ions stay trapped due to the extended presence of electrons. This is a phenomenon leading to obstruction of negative ion fluxes towards the plasma-containing walls. This behavior is known as negative-ion self-trapping in the afterglow [30].

O_2^- negative ion density

Absolute values of the O_2^- negative ion density are measured subsequently. O_2^- densities are measured to be one order of magnitude smaller (10^{14} m^{-3}) than the total negative ions density of O^- plus O_3^-, underlying the fact that O_2^- ions constitute about 10 % of the total negative ions in the plasma as was earlier explained. The O_2^- density is measured for both the γ-mode at 3 Pa (Figure 6.8) and the α-mode at 6 Pa (Figure 6.9) accordingly. Noteworthy is the fact that due to both the much smaller photodetachment cross section of O_2^- at 1064 nm and the relatively lower concentrations, the O_2^- density falls under the detection limit (10^{12} m^{-3}) at shorter time scales than the densities in the previous section do. As a result, the O_2^- density could be tracked for only 3 ms into the afterglow phase.

First, the O_2^- density is measured time-resolved with 100 μs time steps in the γ-mode of the afterglow phase (see Figure 6.8). Just as in the previous case with O^- and O_3^-, the decay time associated with the negative ions is longer than that associated with the electrons, and the observed electron density decay behavior is similar to previous cases. The decay time of the O_2^- density is calculated τ = 756 μs according to the exponential fit in the same Figure 6.8. Moreover, the longer decay time associated with O_2^- (Figure 6.8) when compared to that of O^- plus O_3^- (Figure 6.6) illustratively indicates that O^- constitutes the majority of the negative ions in the plasma.

Subsequently, the same set of measurements is repeated at an elevated pressure of 6 Pa - i.e. in the α-mode (see Figure 6.9). Here, the O_2^- negative ion density decay occurs on a time scale comparable to the decay time scale for electron density. The decay time for the O_2^- density τ = 376 μs is calculated according to the exponential fit in the same Figure 6.9.

Figure 6.8: Time-resolved electron density (blue curve) together with O_2^- negative ion density (circles) during the afterglow phase operating at a pressure of 3 Pa (γ-mode). The negative ion density decay is fitted with a one-term exponential fit (red curve).
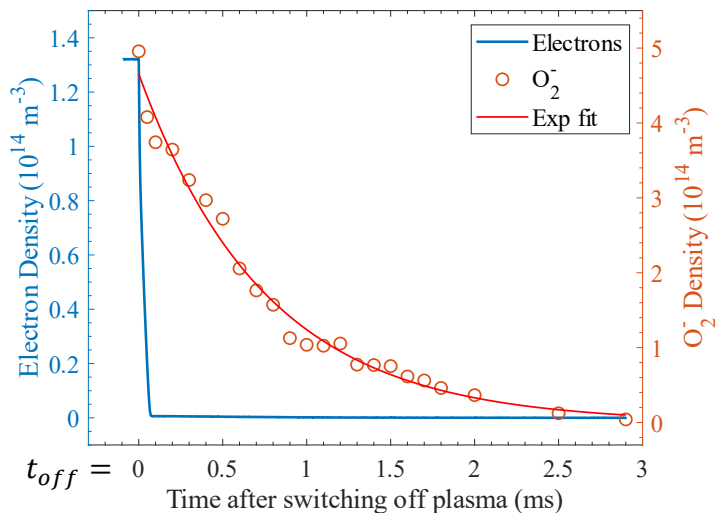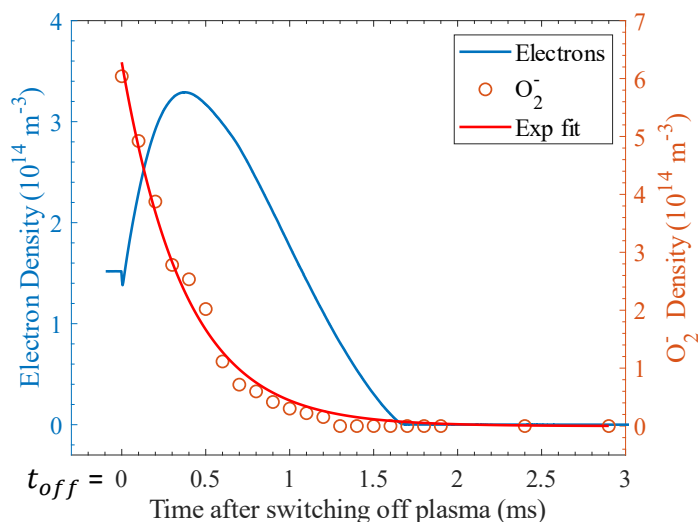

Figure 6.9: Time-resolved electron density (blue curve) together with O_2^- negative ion density (circles) during the afterglow phase operating at a pressure of 6 Pa (α-mode). The negative ion density decay is fitted with a one-term exponential fit (red curve).

6.4 Conclusions

The Afterglow phase of a capacitively coupled pulsed RF oxygen plasma is investigated using MCRS and LIP. While electrons decay on significantly different time scales depending on the gas pressure, the decay time scales associated with oxygen anions are similar.

At a pressure of 3 Pa, namely γ-mode operation, electrons decay rapidly upon the moment the RF pulse falls. In this case, the decay is dominated by plasma diffusion to and recombination at the plasma-containing walls. At a slightly elevated pressure of 6 Pa (and higher), the electron density decay features a rampant release of electrons caused by the detachment of electrons from mainly O^-.

The photodetachment signal - i.e. the total amount of electrons photodetached from their parent negative ions - is shown to be comprised of different stages depending on the gas pressure.

The decay of the oxygen negative ions densities in two cases of, first, O^- plus O_3^- and, subsequently, O_2^- behave similarly during the afterglow phase in both γ-mode and α-mode. Negative ions decay, however, on time scales significantly longer than those associated with electrons when operating in γ-mode. A transition to negative-ion-positive-ion plasma occurs in the case of total decay of electrons. In α-mode operation, the overall decay of the electrons is extended. This leads to obstruction of negative ion fluxes towards the plasma-containing walls, characterized as negative-ion self-trapping in the afterglow.

Chapter 7

Laser-induced photodetachment to probe argon-acetylene plasma afterglow

Abstract

The temporal afterglow of a radio-frequency driven low-pressure argon-acetylene plasma is experimentally explored using laser-induced photodetachment combined with microwave cavity resonance spectroscopy. The densities of electrons and negatively charged species, i.e., anions and dust particles, are measured temporally resolved until 1.9 s in the temporal plasma afterglow. Two different plasma-on times are adjusted to investigate the dynamics of anions and dust particles in the afterglow phase. The measurements show that while electrons decay rapidly within the first few milliseconds of the afterglow phase, the negatively charged species reside much longer in the plasma after the plasma is switched off. The electron density decay is measured to be faster for a longer plasma-on time. This effect is attributed to an enhanced recombination rate due to a higher dust particle density and/or size. The density of negatively charged species decays within two different timescales. The first 20 milliseconds of the afterglow is marked with a rapid decay in the negatively charged species density, in contrast with their slow density decay in the second time scale. Moreover, a residual of the negatively charged species densities is detected as long as 1.9 s after extinguishing the plasma.

7.1 Introduction

Dusty or complex plasmas (i.e. low-pressure plasmas containing nano- to micrometer-sized particulates) have become of considerable importance due to their prevalence in various research areas and applications. From a fundamental viewpoint, dusty plasmas are abundantly present in outer space, e.g. in comet tails [133] and in the rings of Saturn [134]. In laboratories on earth, complex plasmas are used as model systems for studying generic phenomena of condensed matter physics and, in that regard, exhibit phenomena such as crystallization [67], melting [135] and turbulence [136].

On the practical side, applications range from the synthesis of polymers [33], nanostructures [34], and functionalized nanoparticles [137] to contamination control in photolithography [69, 138] and plasma diagnostics [79].

Dust particles are often externally injected into plasma environments, but can also be spontaneously formed when plasmas are ignited in reactive gases such as silane [139], hexamethyldisiloxane [140], methane, and acetylene [141]. In general, the spontaneous formation of dust particles inside an (often radiofrequency (RF) driven) low-pressure plasma can be described by several stages and begins with the polymerization stage [35]. Upon ignition of the plasma in a reactive gas mixture - such as in Ar/C_2H_2 as is the case in this work - negative ions (anions) are formed by the reaction of an electron with a monomer acetylene molecule in a process called dissociative electron attachment [36]:

$$C_2H_2 + e^- \rightarrow C_2H^- + H. \tag{7.1}$$
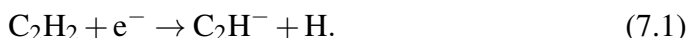
The primary C_2H^- anions, electrostatically trapped in the central region of the plasma by virtue of the positive potential of the plasma bulk, can trigger a consecutive chain of polymerization reactions when reacting with other monomer molecules to form larger molecules [37]:

$$C_{2n}H^- + C_2H_2 \rightarrow C_{2n+2}H^- + H_2. \tag{7.2}$$
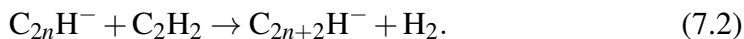
Here, the initial polymerization of C_2H^- corresponds to n = 1. Subsequently, the particle nucleation stage leads to the formation of small clusters with a size of several nanometers. This process is often dominated by reactions between electrically trapped anions in the plasma and neutral molecules or radicals that contribute to cluster growth [11]. In the next step of particle formation, namely coagulation, the growth of larger dust particles results in gaining an increasing and permanent negative charge. Finally, the particle growth culminates in the accretion step whereby the dust particles grow linearly over time [142]; before the particles fall outside the plasma due to domination of ion drag force.

Experimental diagnostic and numerical modelling studies have been conducted to measure the densities of electrons, ions, neutrals, and dust particles, as well as determine the evolution of the charge of dust particles during steady-state and afterglow plasma conditions. Jiménez-Redondo *et al.* [143] studied the first stages of polymerization in Ar/C_2H_2 RF plasmas by mass spectroscopy measurements and with a volume-averaged model. In their measurements, the negative ions distributions showed a clear dominance of ethynyl (C_2H^-) and vinylidene (H_2CC^-) anions while anions with higher molecular weights were found to be present with relatively lower densities. Recently, increasing attention has been devoted to a special case of dusty plasma [144]: a dusty afterglow plasma. In general, afterglow plasmas can be divided into temporal plasma afterglow plasmas (i.e. plasmas extinguishing over time) [145], spatial afterglow plasmas [146] (i.e. plasma residues spatially away from the active (powered) plasma region) or combination of the two [147]. The focus of the current work is on the temporal afterglow of a particle forming plasma. In such type of plasma afterglow, the charge of small nanoparticles was already found to vary slowly in the late afterglow, compared to a rapid decrease of particle charge in the initial stages of afterglow, and eventually to become "frozen" due to very small positive ion and electron densities and currents in the late afterglow [148, 149]. These results are in agreement with the findings of Couëdel *et al.* [150], detecting similar particle charge residuals in the late plasma afterglow. The temporal evolution of the electron density in Ar/C_2H_2 RF plasmas has been experimentally explored by microwave interferometry [151] and microwave cavity resonance spectroscopy [41]. Specifically, an initial release of secondary electrons in the very beginning of the afterglow phase was observed [151, 152] and attributed to the detachment of electrons from the dust particles due to the collision of dust particles with ions [152] or metastables and/or to electron generation by metastable-metastable collisions [153].

The afterglow phase becomes of intrinsic importance when a (dusty) plasma is being pulsed and has a dominant impact on the dynamics of the particles once the plasma is extinguishing. From an application point of view, nanoparticle collection [154, 155] and nanoparticle contamination control [156] applications can directly benefit from experimental data aiming at grasping this particular phase. Although temporal afterglows of dusty plasmas have been extensively studied using numerical methods [157–159], experimental data showing the temporal evolution of negatively charged species (i.e. anions and dust particles) are scarce. So far, available experiments have been mainly dedicated to studying de-charging and residual charge measurements of injected microparticles [12, 160, 161] and very few on in-situ chemically formed nanoparticles.

In this work, the temporal evolution of the densities of electrons and neg-

atively charged species in the afterglow of a dust-forming capacitively coupled pulsed RF argon-acetylene plasma is experimentally investigated. For this purpose, the previously developed [162] method of laser-induced photodetachment combined with microwave cavity resonance spectroscopy is applied. Investigated specifically are the plasma afterglow decays of primary anions and small clusters that are formed during different plasma-on times prior to the plasma afterglow phase, i.e., 14 ms and 100 ms.

The current chapter is structured as follows. In section 7.2, the experimental methods are briefly explained. Section 7.3 presents structured time-resolved measurements of the electron and the negatively charged species densities during the afterglow phase of argon-acetylene plasma. Specifically, the effect of the plasma-on time on the electron and negatively charged species decays are discussed. Finally, section 7.4 outlines the conclusions and summarizes the study.

7.2 Methods

The experimental setup used for particle growth within the plasma and the methods applied for studying the densities of electrons and negatively charged species have been previously implemented and discussed in chapter 6. Here, a description is provided that only briefly explains the experimental methods (i.e. laser-induced photodetachment and microwave cavity resonance spectroscopy) and indicates the experimental parameters used throughout the this chapter.

7.2.1 Microwave cavity resonance spectroscopy and laser-induced photodetachment

Microwave cavity resonance spectroscopy (MCRS) is the method that enables the detection of free electrons within a cylindrical cavity with metallic walls. Initially, microwave resonant modes are excited within this cavity, with each mode having its own electric field distribution and resonance frequency. For the used cavity geometries, this resonance frequency is typically in the GHz frequency range. Upon the emergence of free electrons originating from the plasma, the permittivity ε of the medium inside the cavity changes. Consequently, the resonance frequency of the excited resonant mode is subject to a shift. The temporal evolution of the electron density inside the cavity volume is determined by tracking the resonance frequency ($f(t)$) of the excited mode and subtracting it from the resonance frequency (f_0) of the empty cavity (i.e. without plasma). Any presence and transient change in the electron density in the plasma, $\overline{n}_e(t)$, is measured

time-resolved by

$$\bar{n}_e(t) = \frac{8\pi^2 m_e \varepsilon_0 f^2(t)}{e^2} \frac{f(t) - f_0}{f_0}, \tag{7.3}$$

where m_e and e are the electron mass and electron charge, respectively, and ε_0 is the permittivity of free space. Noteworthy is the fact that the obtained electron densities are electric field (of the applied resonant mode) weighted and (cavity) volume averaged. The spatial distribution of the microwave electric field of the used resonant mode, TM_{010}, indicates the regions in which the resonant mode is most sensitive to the presence of free electrons. A 3D simulation of TM_{010} microwave mode is provided previously 3 and is illustrated in figure 3.3, showing that the central region of the cylindrical cavity is maximally sensitive and decreases radially. As for the cavity used in this research, the internal diameter and height were 170 mm and 67 mm, respectively. The fundamental resonance frequency was $f_0 = 1.3678$ GHz, and the quality factor was $Q = 397$. Therefore the time resolution of the MCRS system limited by the cavity's response time was $\tau = \frac{2Q}{2\pi f_0} = 92$ ns.

While MCRS is an approach for electron density measurement, laser-induced photodetachment (LIP), combined with MCRS, is an indirect method of detecting negatively charged species. Upon the incidence of laser photons, the electrons may be detached from the negatively charged species (i.e. anions or dust particles) that are subsequently converted to electron-neutral pairs. The necessary condition for photodetachment occurrence is that the photon energy ($h\nu$) exceeds the electron affinity of the negatively charged species. Generally, in the first few milliseconds of the particle formation process, anions first begin to emerge due to the dissociative attachment of electrons to monomer molecules [36, 60]. A list of five species of anions with the most abundance [39], together with their photodetachment threshold energies, is presented in Table 7.1.

The fourth harmonic of an Nd:YAG laser was chosen to detect the anions and particle charge density for all the photodetachment experiments presented here. The laser light wavelength, therefore, was 266 nm equivalent to a photon energy of 4.66 eV. Consequently, the laser was capable of inducing photodetachment events from all of the anion species mentioned in Table 7.1. Upon the photodetachment incident, a sudden local surge of electron density is detected, using MCRS, as an additional temporal shift in resonance frequency. As illustrated in figure 7.1, the photodetachment incident appears as a momentary electron release resolved via equation 7.3.

Ideally, the laser pulse is capable of converting all of the negatively charged species into electron-neutral pairs. In that case, the diagnostic is operated in its
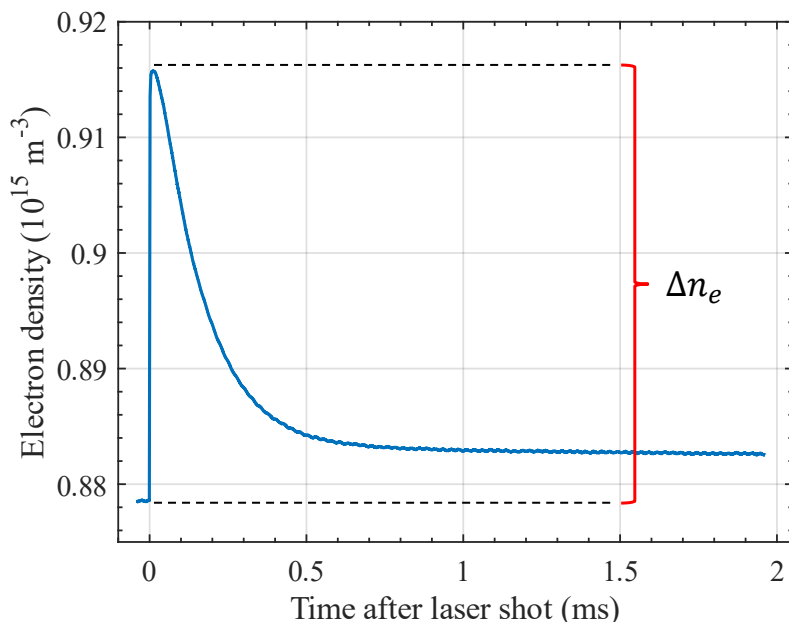
Figure 7.1: Typical measurement of electron release upon photodetachment incident ($t = 0$): an additional electron density (Δn_e) is detected with MCRS. Here the plasma operates at steady-state conditions of 10 Pa pressure of argon-acetylene gas and 10 W deposited power.

Table 7.1: Electron affinities of negatively charged species [163, 164].

Negative ion	Electron affinity (eV)
$H_2CC^- + h\nu \rightarrow C_2H_2 + e^-$	0.490
$C_2H^- + h\nu \rightarrow C_2H\cdot + e^-$	2.956
$C_4H^- + h\nu \rightarrow C_4H\cdot + e^-$	3.558
$C_6H^- + h\nu \rightarrow C_6H\cdot + e^-$	3.809
$C_8H^- + h\nu \rightarrow C_8H\cdot + e^-$	3.966

saturation regime. Photodetachment in the saturation regime often demands a high laser pulse energy. In our case, however, the laser pulse only partially converted the negatively charged species along its path. The photodetached electron density, in this case, scales exponentially with the laser pulse energy and photodetachment cross-section of the negatively charged species. The fraction (α) between the photodetached electron density using a specific laser pulse energy (Δn_e) and the photodetached electron density in the saturation regime (Δn_e^{sat}) is given [165] by:

$$\alpha = \frac{\Delta n_e}{\Delta n_e^{sat}} = 1 - \exp\left(-\frac{\sigma_{det}}{h\nu}\frac{E_{laser}}{S}\right), \tag{7.4}$$

where σ_{det}, $h\nu$, E_{laser}, and S indicate the photodetachment cross section of a specific species, the energy of the photons used for irradiation, the laser pulse energy, and the laser beam's cross-sectional surface area, respectively. In the following experiments, multiple negatively charged species contributed to the overall photodetachment trials. Hence, before performing photodetachment experiments to determine densities of negatively charged species, a preliminary set of experiments is necessary to establish the total cross-section (σ_{det}) and, next, the photodetachment fraction (α).

7.2.2   Experimental setup

The experimental setup is described in detail in chapter 4 where a schematic representation is also included (see figure 4.4).

For the experiments performed in this chapter, steady flows of 9.1 SCCM and 1.9 SCCM of argon and acetylene gases, respectively, were fed to the vacuum chamber, and the gas pressure was set to 10 Pa by controlling the butterfly valve. The RF generator delivered a pulsed 13.56 MHz RF signal of 10 W during the plasma-on phase. The plasma pulse frequency was set by the delay generator to 5 Hz for 14 ms and 0.5 Hz for 100 ms plasma-on durations, resulting in 7%, and 5% duty cycles, respectively.

The detection limit of the current diagnostic method for measuring the density of negatively charged species was 10^{12} (m^{-3}). This was determined by the stability of the laser beam energy and the reproducibility of plasma pulses. The measurement error stems mainly from a slight instability in the laser beam energy; therefore, the laser beam energy per pulse was measured throughout the experimental campaign. This instability caused a maximum error of 4% in negatively charged species density measurements. Moreover, the error in the electron density measurements was typically 0.1% [162].

7.3 Results and Discussions

The decays of the densities of electrons and negatively charged species (i.e. anions and/or dust particles) during the plasma afterglow were studied by conducting the following experiments. Generally, two sets of experiments were conducted, with each set having had a specific plasma-on time prior to the start of the afterglow phase. The differentiation in plasma-on time was introduced in order to investigate the impact on the afterglow dynamics of anions and/or dust particles. In section 7.3.1, the decay of the electron density during the afterglow when the plasma was switched on for two different plasma-on times is discussed. Subsequently, in section 7.3.2, negatively charged species densities measurements and their decays - also for different plasma-on times - are discussed.

7.3.1 Electron density

The electron density during the afterglow phase was measured time-resolved using MCRS in the TM_{010} mode, probing electrons especially in the central region of the cavity. Figure 7.2 demonstrates the afterglow behaviour of the electron density when the plasma-on time is subject to change. For a prior plasma-on time of 14 ms, the electron density decayed exponentially with a decay time of $\tau_{loss}=$ 447 μs during the afterglow phase. The decay time for the 100 ms plasma-on time case was $\tau'_{loss}=$ 352 μs, i.e. a 20% shorter decay time compared to the 14 ms plasma-on time case. The decay times mentioned above were obtained by fitting an exponential decay function to the experimentally obtained electron density evolution.

The trend of a faster electron density decay observed for a longer plasma-on time prior to the afterglow phase can be explained by the growth of (more and/or larger) dust particles due to the extended particle formation period. As the particle formation period extends, the initially formed anions may form primary clusters. This effect can - likewise - also be observed from the lower initial electron density just before the afterglow phase for longer plasma-on times (see figure 7.2); during longer plasma-on times, more electrons are lost by electron attachment [166], to form anions and/or to (growing) dust particles.

Although the lower initial electron density just before the afterglow phase can be explained by an increase in density (and/or size in the case of dust particles) of both anions and dust particles, the fact that for longer plasma-on times the electron density decays faster points to the appearance and/or growth of dust particles in the 100 ms plasma-on time case compared to the situation for the experiments with 14 ms plasma-on time. If the appearance or growth of dust particles had

not played a role, longer electron density decay times in the afterglow for longer plasma-on times prior to that afterglow phase would have been expected as, during the afterglow, detachment of electrons from anions would have delayed the overall electron density decay. This hypothetical case is opposite to what is observed.

Overall, from the above, two intermediate conclusions can be drawn. I) It can be concluded that there are dust particles present in - at least - the afterglows with a prior plasma-on time of 100 ms. Although this could be the case for the 14 ms plasma-on time case as well, it cannot be directly concluded from the available data. II) It can be concluded that the decay of the electron density in the experiments with 100 ms plasma-on time is dominated by electron loss coupled to the presence of dust particles.

In general, the electron density decay in the afterglow of a dusty plasma is governed by diffusion of plasma species towards plasma-containing walls and recombination onto the dust particles' surfaces [148, 167]:

$$\tau_{loss}^{-1} = \tau_{diff}^{-1} + \tau_{recomb}^{-1}. \tag{7.5}$$

Here τ_{loss}, τ_{diff}, and τ_{recomb} are decay time scales for the electron density loss, electron diffusion, and recombination losses of electrons due to absorption by dust particles. According to Couëdel *et al.* [148], the latter is inversely proportional to the dust density ($\tau_{recomb}^{-1} \propto n_d$) when the dust density is low. For the case of high dust density, τ_{recomb} still decreases with dust density. However, the decrease is no longer linear, and the effect of dust particles on the electron loss becomes relatively attenuated. Therefore, an increase in dust particle density enhances surface recombination losses of electrons. As a longer plasma-on time leads to an increased density of dust particles, the electron density can be expected to decay faster due to enhanced recombination rates. Moreover, also larger dust particles formed in extended plasma-on times can contribute to a faster decay rate as $\tau_{loss}^{-1} \propto r_d^2$ [148].

In order to further support the conclusions drawn above, a third set of measurements is included in Appendix 7.A. This data set shows the electron density decay in the afterglow phase for a plasma-on time of 1 s. These measurements - in which even larger dust particles were (visibly) present - demonstrate an even further shortened electron density decay time of 147 μs, as is in line with the trend found from the 14 ms and 100 ms plasma-on time cases in this section. Those data are shown in the Appendix 7.A and not in the main document, as a one-on-one comparison between them and the data presented in this section is questionable as using the 5 Hz laser repetition rate meant that also laser pulses irradiated through the cavity volume during the plasma-on time. Nevertheless, the electron density
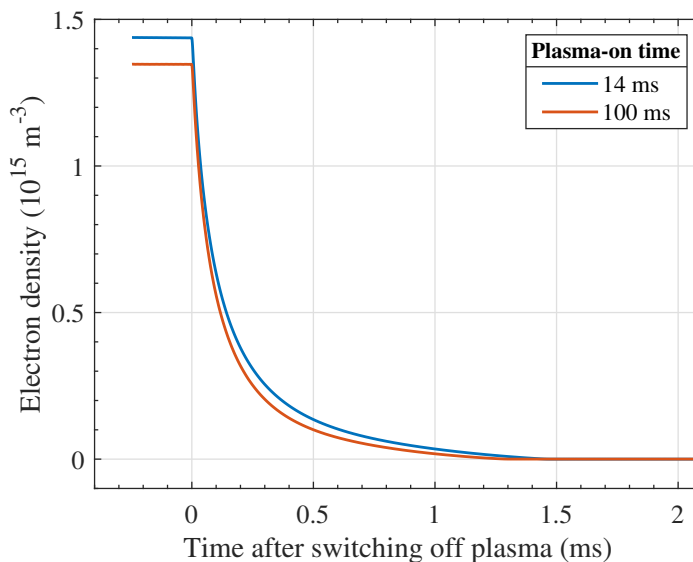
Figure 7.2: Time-resolved electron densities during the afterglows of 14 ms and
100 ms growth periods.

evolution during the plasma-on time appears reasonably consistent between the
three measurements indicating the limited effect of laser irradiation during the
plasma-on phase.

7.3.2 Negatively charged species density

To detect and measure the density of negatively charged species, photodetach-
ment using laser light with a photon energy of 4.66 eV (266 nm wavelength) was
applied to the plasma. Here, we define the negatively charged species density
as a value connected to the density of the total release of electrons upon a pho-
todetachment experiment. In other words: The total negatively charged species
density consists of a contribution from anions and a contribution from electrons
released from dust particles. In the latter case, by removing x electrons from
each negatively charged dust particle while having a density of n_d, the total con-
tribution from negatively charged dust particles equals xn_d. Upon irradiation of
the (former) plasma volume with the laser pulse, the negatively charged species,
which had a lower electron affinity than the laser photon energy, yielded an elec-
tron release that could be detected using the MCRS technique. Subsequently,
equation 7.4 was used to translate the measured additional electron density (Δn_e),
caused by the photodetachment events, to an absolute value of the negatively

charged species density (n_-). Initially, it was examined whether the conversion of all the negatively charged species within the laser beam volume (i.e. saturation regime) was achieved. Figure 7.3 shows the measured values of the photodetached electron density as a function of laser pulse energy. Here, the photodetachment experiments were performed at the end of both plasma-on times of 14 ms and 100 ms, yielding similar results. According to figure 7.3, the saturation regime could not be fully reached with the laser operating at its maximum energy (E_{laser} = 90 mJ) since the photodetached electron density did not reach a saturated value for that energy yet. Therefore, it was determined what fraction α of the negatively charged species were photodetached by fitting equation 7.4 to the measured values presented in figure 7.3, which led to the indirect calculation of the negatively charged species density ($n_- = \frac{\Delta n_e}{\alpha}$) from Δn_e. Just like in basically all preceding laser-induced photodetachment experiments [60, 131, 168, 169], the value of α was obtained for each prior plasma-on time case once at the beginning of the afterglow phase and was then assumed fixed for the rest of the afterglow. Although this approach appears reasonable during most of the afterglow phase – as the majority of the negative ions is C_2H^- - the value of α might be subject to change towards the end of the afterglow phase when most C_2H^- ions might have decayed and the relative contribution of C_2H^- photodetachment to the overall photodetachment signal could become less dominant. Especially in the very late afterglow phase, future experiments would benefit from a saturation curve measurement (as in figure 7.3) for each individual measurement point. Although improving the measurement accuracy via the value of α, such an undertaking would increase the overall measurement time – already being significantly long - by an order of magnitude. The photodetachment cross-section value, also obtained by the fits for both data sets of 14 ms and 100 ms plasma-on times, was $\sigma_{det} = (6.0 \pm 0.1) \times 10^{-22} \ m^{-2}$, accounting for all the negatively charged species within the laser volume. This value of the photodetachment cross-section is approximately equal to the cross-section value for C_2H^- anion [170, 171]. This implies that a majority of the negatively charged species within the plasma are ethynyl (C_2H^-) anions for both prior plasma-on times, as the other negative ions have different cross-sections. In principle, the same study for the determination of the photodetachment cross-section (σ_{det}) and photodetachment fraction (α) can be performed for longer plasma-on times with larger anions and dust particles.

Referring back to the previous section, it can be concluded that on the one hand, the majority of the species responsible for Δn_e due to photodetachment is C_2H^-, while the decay of the electron density is governed (at least for the 100 ms plasma-on time case) by dust particles.

Subsequently, the total absolute values of the densities of all negatively charged
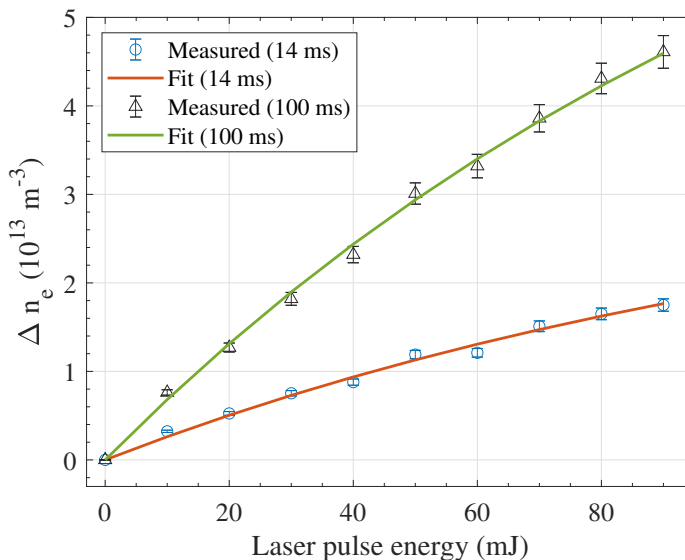
Figure 7.3: The measured values of photo-detached electron density (Δn_e) as a function of laser pulse energy at the end of 14 ms plasma-on time (blue circles) and 100 ms plasma-on time (black triangles). Equation 7.4 is fitted with the measured values of 14 ms (red curve) and 100 ms (green curve) plasma-on times.

species, including anions mentioned in table 7.1 and dust particles, were measured time-resolved during the temporal afterglow of the plasma. For this purpose, LIP measurements were performed at a specific and progressing delay time after the plasma was switched off. Figure 7.4 illustrates the densities of the negatively charged species together with those of the free electrons in the afterglow phase - again - for two different prior plasma-on times of 14 ms and 100 ms (figure 7.4 (a) and (b), respectively). First, in figure 7.4 (a), the argon-acetylene plasma was operated for 14 ms before it was switched off at $t = 0$. As illustrated, the negatively charged species density decayed rapidly by 75% from its initial density of $n_- = (1.94 \pm 0.07) \times 10^{15} \ m^{-3}$ to a density of $n_- = (0.47 \pm 0.01) \times 10^{15} \ m^{-3}$ during the first 15 ms of the afterglow phase. Afterwards, it remained relatively stable during the next 85 ms of the afterglow, as it had decreased to $n_- = (0.35 \pm 0.01) \times 10^{15} \ m^{-3}$ at the final measurement time (100 ms). Subsequently, the plasma-on time was increased to 100 ms. As a consequence of the longer plasma-on time, the negatively charged species density was measured to be relatively higher ($n_- = (2.4 \pm 0.1) \times 10^{15} \ m^{-3}$) at the beginning of the afterglow phase, when compared to that for the experiment with 14 ms plasma-on time. As mentioned earlier, this trend is also indicated by a

lower value (for longer plasma-on times) of the electron density prior to the start of the afterglow phase. As seen in figure 7.4 (b), the negatively charged species density decreased by 75% of its initial value to $n_- = (0.58 \pm 0.02) \times 10^{15}$ m^{-3} during the first 20 ms of the afterglow phase. Later during the afterglow, the negatively charged species density was measured to slowly decrease to $n_- = (0.15 \pm 0.01) \times 10^{15}$ m^{-3} right before the initiation of the next plasma-on phase.

From measurements of the electron and the negatively charged species densities, illustrated in figure 7.4, it was observed that the negatively charged species decayed following two different timescales while the electrons decayed abruptly at the very early afterglow phase (within the first milliseconds). The initial fast decay of negatively charged species can be explained by, first, the drop in electron temperature (T_e) and, second, the loss of electrons due to diffusion and recombination and, therefore, the ceasing of the quasi-neutrality condition in the plasma.

In general, the beginning of the afterglow is characterized by a sharp decrease in electron temperature [29, 172] resulting in the termination of anion production as well as suppression of the electron current to the dust particles' surfaces. Anions are mainly produced via dissociative attachment of electrons [36]; therefore, when the electron temperature drops from its initial value of typically a few eV to 0.025 eV (room temperature), electrons are no longer capable of producing negative ions. Moreover, as most of the electrons have diffused (mainly by means of ambipolar diffusion, followed by free diffusion) towards the plasma-containing walls or to dust particles' surfaces, the electrostatic confinement of the negatively charged species, i.e. based on the determined photodetachment cross section in figure 7.3 dominantly anions, ceases. Therefore an immediate decrease in the density of the negatively charged species is observed in the first 20 milliseconds of the afterglow. Also, suppression of the electron current to the dust particles contributed to the explanation of the swift drop in the density of the negatively charged species. Generally, the charge of dust particles is determined by an equilibrium between the electron and ion currents towards the particles' surfaces [173]. As a result of the electron temperature drop to room temperature and electron losses due to diffusion, the electron current towards the particles is inhibited. In contrast, the ion current stays relatively constant. Therefore, the particle charge becomes less negative due to a relatively higher flux of positive ions towards their surface [149].

In the late afterglow, however, the density of negatively charged species decreased at a much slower rate compared to the early afterglow phase during the first 20 milliseconds. Furthermore, a residual density of negatively charged species was measured in experiments for both plasma-on times. For the case when the plasma-on time was set to 14 ms, negatively charged species residing in
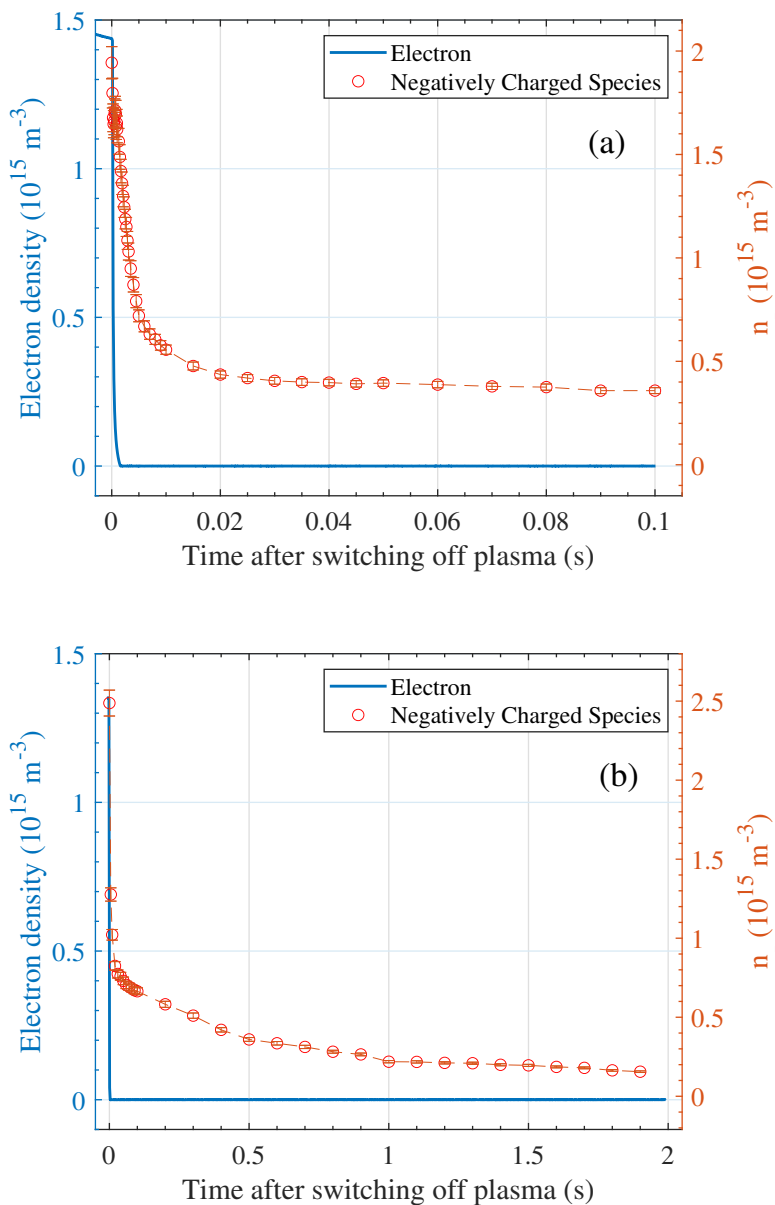
Figure 7.4: Temporal evolution of electron density (blue curve) together with the density of negatively charged species (red circles) for growth periods of 14 ms (a) and 100 ms (b).

the plasma during the entire afterglow is mainly due to a relatively higher plasma pulse repetition frequency (5 Hz). This results in a relatively shorter plasma afterglow time. The observed decay in the afterglow phase can be described by a two-stage mechanism [174]. During the first stage, the electrons diffuse towards chamber walls (and in this case towards dust particles' surfaces) while negative ions are trapped within the plasma, forming a positive-ion-negative-ion plasma, possibly including small dust particles. The second stage in the afterglow begins with diffusing anions and positive ions slowly towards the walls by ion-ion ambipolar diffusion. As simulated previously by Berndt *et al.* [175], for sufficiently high repetition frequencies, the anion density only partially decays, and a residual density of anions influences the subsequent plasma pulse in a pulsed RF plasma. In this case, similar to the 14 ms plasma-on time case in figure 7.4 (a), the afterglow time is not long enough for all the anions to diffuse out and the negatively charged species density to decay completely. For the 100 ms plasma-on time (and 0.5 Hz plasma pulse frequency), the slower decreasing trend in the density of negatively charged species can be due to the fact that as nearly all electrons and most negative ions have diffused out, a substantial drop in plasma density prevents any significant change in the charge of dust particles [150]. Therefore, a residual density of negatively charged species (consisting of anions and/or negatively charged dust particles) was observed in both instances of plasma-on times.

7.4 Conclusions

This article presented experimentally obtained results on the temporal afterglows of Ar/C_2H_2 plasmas. Electron and negatively charged species densities were measured time-resolved within prolonged afterglows of the plasma up to 1.9 s, using microwave cavity resonance spectroscopy combined with laser-induced photodetachment. Two different plasma-on times of 14 ms and 100 ms prior to the start of the afterglow phase were applied to study the contribution of anions and dust particles to the afterglow dynamics. Based on the electron density measurements, it was found that electrons decay faster after longer plasma-on times since the electrons were dominantly lost due to an increased recombination rate as the small (and growing in density and/or size) dust particles acted as additional recombination surfaces. Based on negatively charged species density measurements, it was observed that these densities decay in two stages with different timescales. First, the negatively charged species densities dropped rapidly within the first 20 milliseconds of the afterglow phase. This rapid density drop could be attributed to electron cooling and (ambipolar) diffusion at the very beginning

of the afterglow; as the electron temperature and electron density dropped, an-
ions could no longer be formed while they diffuse outwards. Also, the electron
current to dust particles may be inhibited by this effect, reducing the number of
electrons on dust particles. Second, a much slower decreasing trend was observed
in the densities of negatively charged species, resulting from depleted positive-
ion-negative-ion plasma density in the late afterglow. Also, for both instances of
plasma-on times, a residual density of negatively charged species was detected in
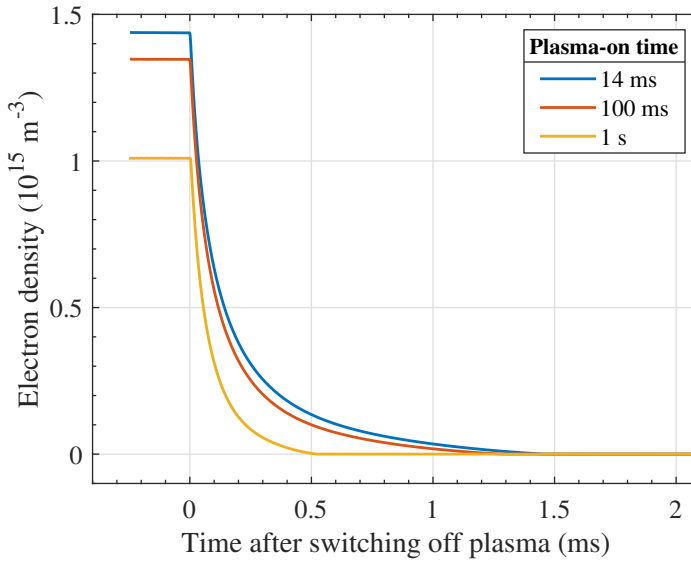the late afterglow.

Figure 7.5: Time-resolved electron densities during the afterglows of 14 ms, 100 ms, and 1 s plasma-on times.

Appendices

7.A   The afterglow of 1 s plasma-on time

The electron density decay during the plasma afterglow is shown in figure 7.5. Before extinguishing the plasma, three different plasma-on times, 14 ms, 100 ms, and 1 s, were adjusted to study the effect of plasma-on time on the decay of electron density. As discussed earlier, the plasma-on time of 1 s constitutes a unique case due to the laser irradiation of the plasma during this prolonged plasma-on time. Nonetheless, it can be observed in figure 7.5 that the electron density decays faster for 1 s plasma-on time (τ_{loss} = 147 μs), compared to 14 ms and 100 ms plasma-on time cases. Also, a lower initial electron density just before the onset of the afterglow phase is observed for the 1 s plasma-on time.

Chapter 8

Conclusions and outlooks

This chapter reflects on the main conclusions obtained from the research conducted in this thesis. Furthermore, the outlooks beyond the framework of the thesis are drawn as the research paves the way for an even more in-depth understanding of plasma charging phenomena.

In the following sections, the conclusions are stated as direct answers to the research questions defined in the introduction (chapter 1). Next, the outlooks for each research line are drawn. Finally, the general findings and implications of the research from a broader perspective are elaborated.

8.1   Conclusions

As stated in the introduction (chapter 1), this thesis focuses on:

"developing diagnostic methods for and gaining a fundamental understanding of the charging and decharging processes of negative ions, nanoparticles, and surfaces in low-pressure radiofrequency plasmas and the afterglow thereof".

Two underlying research lines were defined to answer the two research questions at the beginning of this thesis. The first research line provides answers to:

Research question 1: Can photoluminescent quantum dots be used to detect and measure the electrical charge on surfaces and nanoparticles in plasma?

According to the experiments presented in chapter 5, indeed a spectral redshift of the photoluminescence spectrum peak from quantum dots (QDs)

was observed and measured upon exposure to a low-pressure radiofrequency plasma. The total redshift consisted of a slow shift (of 1.1 nm) and a fast shift (of 0.05 nm); temperature effects induced the former, while the surface charge obtained from the plasma caused the latter. The fast shift, caused by the surface charge, was isolated and studied with a structured set of experiments.

The fast (Stark) redshift of the photoluminescence spectrum peak position was caused by electric fields originating from electrons residing on the surface. These electric fields were calculated, using the *discrete charge model*, to be typically 6.8×10^6 V/m, which would induce a Stark shift of 0.05 nm. This value corresponded to the observed Stark shift value.

To change the surface charge the quantum dots were exposed to, the plasma input power was increased from 10 W to 90 W. It was observed that the Stark shift value increased from 0.022 nm to 0.073 nm. Therefore, it can be concluded that the Stark shift could be used to quantitatively track the variations in the surface charge density besides merely detecting the presence of surface charge.

Overall, yes, photoluminescent quantum dots can detect and relatively measure the charge of plasma-exposed surfaces and, potentially, of particles.

Research question 2: How do electrons and negatively-charged species behave during the afterglow of electronegative and reactive plasmas?

For the electronegative plasma afterglow, studied in chapter 6:

The behaviour of electrons and the conditions of the electronegative oxygen-based plasma in the temporal afterglow were found to depend on the gas pressure. As the power of the plasma was cut, two different timescales and density decays were associated with the electron density.

At a pressure of 3 Pa (plasma operating in γ-mode), the electron density decay was dominated by plasma diffusion to and recombination at the plasma-containing walls. In this mode, the negative ions decayed on a much longer timescale and resided for a more extended period in the former discharge region. The lack of electrons and continued residence of negative ions in the late afterglow led to a transition to a negative-ion-positive-ion plasma.

At a pressure of 6 pa (and more) (plasma operating in the α-mode), the electron density decay featured a rampant release of electrons caused by

associative detachment of electrons from negative ions (mainly O^-). As a result, the electrons resided in the former discharge volume for an extended period during the afterglow. This situation led to the building up of electrostatic fields in the core and the electropositive edge of the plasma. Consequently, the negative ions remained trapped due to the extended presence of electrons. This phenomenon led to the obstruction of negative ion fluxes towards the plasma-containing walls, a behaviour known as negative-ion self-trapping in the afterglow.

For the reactive plasma afterglow, studied in chapter 7:

It was observed that a higher density and/or larger size of dust particles led to a faster electron density decay during the temporal afterglow of an Ar/C_2H_2 plasma. Based on electron density measurements, it was found that electrons decay faster for longer plasma-on times prior to the afterglow phase since the electrons were dominantly lost due to an increased recombination rate at the surface of the formed dust particles. Two different plasma-on times (i.e. 14 ms, and 100 ms) were adjusted before the afterglow phase to study the contributions of anions and dust particles to the afterglow. As the plasma-on time was extended, the dust particles' density increased, and possibly larger dust particles could be formed in the plasma.

The decay of negatively charged species occurs in two stages with different timescales. Based on the measurements, it was observed that, first, the negatively charged species density dropped rapidly within the first 20 milliseconds of the afterglow phase. This rapid decay of negatively charged species could be attributed to electron cooling and (ambipolar) diffusion at the very beginning of the afterglow, as well as to suppression of the electron current to the dust particles. Subsequently, after this swift density drop, a much slower decreasing trend was observed in the densities of negatively charged species. This could be attributed to a depleted positive-ion-negative-ion plasma density in the late afterglow.

Particularly, a residual of negatively charged species was detected in the former plasma volume as long as 1.9 s after the plasma was extinguished.

8.2 Outlooks

Each research line can be individually extended beyond the frameworks of this thesis. The first research line, about charge visualization using quantum dots, has paved the way for charge visualization and measurement of micro to nanometer-sized particles in plasmas. The second research line, about electronegative and reactive plasma afterglows, has developed diagnostic techniques which can be further developed or combined with complementary techniques to gain a more comprehensive understanding of these systems.

8.2.1 Charge visualization using quantum dots

The outlook of the quantum dot charge visualization research line is two-fold:

- Microparticle charge measurement upon plasma immersion using a surface deposited layer of quantum dots.

Based on calculations of Pustylnik *et al.* [176], the microparticle charge can be optically measured when a layer of quantum dots is deposited on its surface. Their calculations show that a measurable Stark shift of the quantum dots' photo-luminescence spectrum peak occurs upon the microparticle's immersion in the plasma. The accumulated surplus electrons on the microparticle surface and their fluctuating electric field are proven to cause the Stark shift. Optical measurements can therefore determine the accumulated charge on the microparticle surface, which suggests the possible design of the charge microsensor. These microsensors can be used as *in-situ* floating probes injected and levitated in, for instance, the plasma sheath region. This research outlook is schematically illustrated in figure 8.1.

- Nanoparticle charge visualization by injecting quantum dots directly into the plasma.

Another outlook regarding charge visualization is the direct use of quantum dots injected into the plasma. The necessary condition for implementing this idea is quantum dot levitation inside the plasma, which has - in the framework of this thesis - been proven technically challenging. However, photoluminescence spectroscopy of laser-excited quantum dots in individual or cloud form will be possible if one succeeds in injecting and levitating quantum dots directly in the plasma. Nanoparticle charging can, in this case, be investigated as the photoluminescence
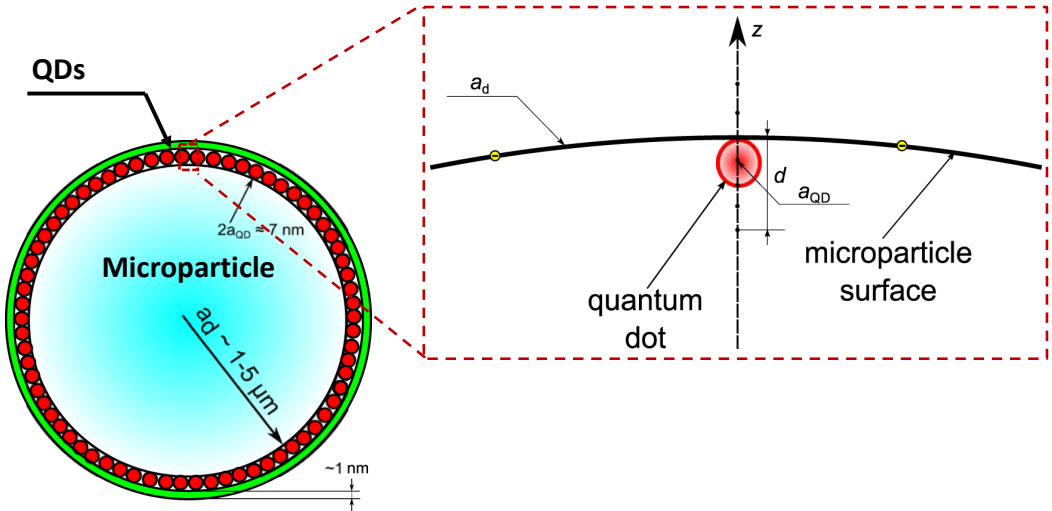
Figure 8.1: Schematic illustration of optical microsensor: a thin layer of quantum dots is deposited on the microparticle with a radius of 1-5 μm. After plasma immersion, the surplus electrons accumulated on the microparticle's surface cause a potentially measurable Stark shift.

spectrum of levitated quantum dots will be subject to a remarkable shift, as predicted by Marvi *et al.* [85], which is a much more significant when compared to typical 0.05 nm measured in our experiments. However, fewer quantum dots will be in the focal point of the optical system, rendering the spectrum recording and analysis much more difficult. In summary, this research idea is promising for the charge measurement of particles on a nanometer scale, although many practical challenges must first be overcome.

8.2.2 Electronegative and reactive plasma afterglows

For the outlook of the second research line, in which negatively charged species are the centerpiece, one could measure the dust particles' population density using laser light extinction [177] (given the fact the particles are a few 100 nm in size) and use these values, in combination with the measurements presented in this thesis, to calculate the average charge number of the dust particles in the plasma. Therefore, a more comprehensive understanding of plasma afterglows can be gained if the behavior of other plasma species (such as dust particles in reactive plasmas) is investigated.

8.3 Overall conclusions

This thesis explores the possibility of using various phenomena as diagnostic methods to visualize and probe the charging and decharging processes in plasma. To this end, the quantum-confined Stark effect phenomenon associated with the electrical charging of quantum dots is first proved to be capable of visualizing the complex process of surface charging in plasma. This thesis also provides additional insights into the temporal afterglows of electronegative and reactive plasmas. The decay of electrons and negative ions measured by the enhanced diagnostic methods can be interpreted in ways that can be used in particle synthesis and contamination control applications.

In conclusion, this thesis lays the foundation for quantum charge visualization of surfaces and nanoparticles and enhances the previously established diagnostic methods. These methods are applied to gain a better understanding of the fundamental charging processes in complex ionized media.

Bibliography

[1] G. S. Selwyn, J. Singh, and R. Bennett, "In situ laser diagnostic studies of plasma-generated particulate contamination", Journal of Vacuum Science & Technology A: Vacuum, Surfaces, and Films **7**, 2758–2765 (1989).

[2] C. Cui and J. Goree, "Fluctuations of the charge on a dust grain in a plasma", IEEE Transactions on plasma science **22**, 151–158 (1994).

[3] S. Khrapak, A. Nefedov, O. Petrov, and O. Vaulina, "Dynamical properties of random charge fluctuations in a dusty plasma with different charging mechanisms", Physical Review E **59**, 6017 (1999).

[4] R. M. van der Horst, J. Beckers, S. Nijdam, and G. M. W. Kroesen, "Exploring the temporally resolved electron density evolution in extreme ultra-violet induced plasmas", Journal of Physics D: Applied Physics **47**, 302001 (2014).

[5] J. Beckers, F. M. J. H. van de Wetering, B. Platier, M. A. W. van Ninhuijs, G. J. H. Brussaard, V. Y. Banine, and O. J. Luiten, "Mapping electron dynamics in highly transient EUV photon-induced plasmas: a novel diagnostic approach using multi-mode microwave cavity resonance spectroscopy", Journal of Physics D: Applied Physics **52**, 034004 (2018).

[6] K. I. Hunter, J. T. Held, K. A. Mkhoyan, and U. R. Kortshagen, "Nonthermal plasma synthesis of core/shell quantum dots: strained ge/si nanocrystals", ACS Applied Materials & Interfaces **9**, PMID: 28169525, 8263–8270 (2017).

[7] L. Boufendi, M. C. Jouanny, E. Kovacevic, J. Berndt, and M. Mikikian, "Dusty plasma for nanotechnology", Journal of Physics D: Applied Physics **44**, 174035 (2011).

[8] C. Pattyn, E. Kovacevic, T. Strunskus, T. Lecas, and J. Berndt, "Formation and behavior of negative ions in low pressure aniline-containing rf plasmas", Scientific reports **9**, 1–9 (2019).

[9]M. Cavarroc, M. Mikikian, Y. Tessier, and L. Boufendi, "Nanostructured silicon thin films deposited under dusty plasma conditions", IEEE Transactions on Plasma Science **36**, 1016–1017 (2008).

[10]Z. Xiong, S. Lanham, E. Husmann, G. Nelson, M. A. Eslamisaray, J. Polito, Y. Liu, J. Goree, E. Thimsen, M. J. Kushner, and U. R. Kortshagen, "Particle trapping, size-filtering, and focusing in the nonthermal plasma synthesis of sub-10 nanometer particles", Journal of Physics D: Applied Physics **55**, 235202 (2022).

[11]S. L. Girshick, "Particle nucleation and growth in dusty plasmas: on the importance of charged-neutral interactions", Journal of Vacuum Science & Technology A: Vacuum, Surfaces, and Films **38**, 011001 (2020).

[12]B. van Minderhout, J. Van Huijstee, A. Peijnenburg, P. Blom, G. M. Kroesen, and J. Beckers, "Charge neutralisation of microparticles by pulsing a low-pressure shielded spatial plasma afterglow", Plasma Sources Science and Technology **30**, 045016 (2021).

[13]T. Flanagan and J. Goree, "Dust release from surfaces exposed to plasma", Physics of plasmas **13**, 123504 (2006).

[14]B. Tadsen, F. Greiner, S. Groth, and A. Piel, "Self-excited dust-acoustic waves in an electron-depleted nanodusty plasma", Physics of Plasmas **22**, 113701 (2015).

[15]J. Carstensen, H. Jung, F. Greiner, and A. Piel, "Mass changes of microparticles in a plasma observed by a phase-resolved resonance method", Physics of Plasmas **18**, 033701 (2011).

[16]H. Jung, F. Greiner, O. H. Asnaz, J. Carstensen, and A. Piel, "Resonance methods for the characterization of dust particles in plasmas", Journal of Plasma Physics **82** (2016).

[17]H. Krüger, E. Thiessen, F. X. Bronold, H. Fehske, and A. Melzer, "Charge measurement of SiO_2 nanoparticles in an rf plasma by IR absorption", Physical Review E **104**, 045208 (2021).

[18]C. E. Rowland, K. Susumu, M. H. Stewart, E. Oh, A. J. Mäkinen, T. J. O'Shaughnessy, G. Kushto, M. A. Wolak, J. S. Erickson, A. L. Efros, et al., "Electric field modulation of semiconductor quantum dot photoluminescence: insights into the design of robust voltage-sensitive cellular imaging probes", Nano letters **15**, 6848–6854 (2015).

[19] I. L. Medintz, M. H. Stewart, S. A. Trammell, K. Susumu, J. B. Delehanty, B. C. Mei, J. S. Melinger, J. B. Blanco-Canosa, P. E. Dawson, and H. Mattoussi, "Quantum-dot/dopamine bioconjugates function as redox coupled assemblies for in vitro and intracellular ph sensing", Nature materials **9**, 676–684 (2010).

[20] J. Müller, J. M. Lupton, A. L. Rogach, J. Feldmann, D. V. Talapin, and H. Weller, "Monitoring surface charge migration in the spectral dynamics of single CdSe/CdS nanodot/nanorod heterostructures", Physical Review B **72**, 205339 (2005).

[21] J. W. Robinson, J. H. Rice, K. H. Lee, J. H. Na, R. A. Taylor, D. G. Hasko, R. A. Oliver, M. J. Kappers, C. J. Humphreys, and G. A. D. Briggs, "Quantum-confined stark effect in a single ingan quantum dot under a lateral electric field", Applied Physics Letters **86**, 213103 (2005).

[22] N. A. Krall and A. W. Trivelpiece, "Principles of plasma physics", American Journal of Physics **41**, 1380–1381 (1973).

[23] P. Chabert and N. Braithwaite, *Physics of radio-frequency plasmas* (Cambridge University Press, 2011).

[24] M. A. Lieberman and A. J. Lichtenberg, *Principles of plasma discharges and materials processing* (John Wiley & Sons, 2005).

[25] P. Chabert, "What is the size of a floating sheath?", Plasma Sources Science and Technology **23**, 065042 (2014).

[26] J. Schulze, A. Derzsi, K. Dittmann, T. Hemke, J. Meichsner, and Z. Donkó, "Ionization by drift and ambipolar electric fields in electronegative capacitive radio frequency plasmas", Phys. Rev. Lett. **107**, 275001 (2011).

[27] E. Stoffels, W. Stoffels, V. Kroutilina, H.-E. Wagner, and J. Meichsner, "Near-surface generation of negative ions in low-pressure discharges", Journal of Vacuum Science & Technology A: Vacuum, Surfaces, and Films **19**, 2109–2115 (2001).

[28] A. Brockhaus, G. F. Leu, V. Selenin, K. Tarnev, and J. Engemann, "Electron release in the afterglow of a pulsed inductively-coupled radiofrequency oxygen plasma", Plasma Sources Science and Technology **15**, 171–177 (2006).

[29] F.-X. Liu, X.-M. Guo, and Y.-K. Pu, "Electron cooling and plasma density decay in early afterglow of low pressure argon plasmas", Plasma Sources Science and Technology **24**, 034013 (2015).

[30] I. D. Kaganovich, B. N. Ramamurthi, and D. J. Economou, "Self-trapping of negative ions due to electron detachment in the afterglow of electronegative gas plasmas", Applied Physics Letters **76**, 2844–2846 (2000).

[31] I. Kaganovich, B. Ramamurthi, and D. J. Economou, "Self-trapping of negative ions due to electron detachment in the afterglow of electronegative gas plasmas", Applied Physics Letters **76**, 2844–2846 (2000).

[32] I. Kaganovich, B. Ramamurthi, and D. J. Economou, "Spatiotemporal dynamics of charged species in the afterglow of plasmas containing negative ions", Physical Review E **64**, 036402 (2001).

[33] D. Sciacqua, E. von Wahl, A. Jagodar, C. Pattyn, T. Lecas, T. Strunskus, E. Kovacevic, J. Berndt, G. Umr, C. K. Team, et al., "Towards a better control of plasma polymerization: a case study of plasma produced polyaniline", in Aps annual gaseous electronics meeting abstracts (2020), YF4–002.

[34] I. Levchenko, M. Keidar, U. Cvelbar, D. Mariotti, A. Mai-Prochnow, J. Fang, and K. K. Ostrikov, "Novel biomaterials: plasma-enabled nanostructures and functions", Journal of Physics D: Applied Physics **49**, 273001 (2016).

[35] A. Bouchoule, *Dusty plasmas: physics, chemistry, and technological impact in plasma processing* (Wiley, 1999).

[36] S. Stoykov, C. Eggs, and U. Kortshagen, "Plasma chemistry and growth of nanosized particles in a C_2H_2 rf discharge", Journal of Physics D: Applied Physics **34**, 2160 (2001).

[37] K. De Bleecker, A. Bogaerts, and W. Goedheer, "Detailed modeling of hydrocarbon nanoparticle nucleation in acetylene discharges", Physical Review E **73**, 026405 (2006).

[38] M. Mao, J. Benedikt, A. Consoli, and A. Bogaerts, "New pathways for nanoparticle formation in acetylene dusty plasmas: a modelling investigation and comparison with experiments", Journal of Physics D: Applied Physics **41**, 225201 (2008).

[39] C. Deschenaux, A. Affolter, D. Magni, C. Hollenstein, and P. Fayet, "Investigations of CH_4, C_2H_2 and C_2H_4 dusty rf plasmas by means of ftir absorption spectroscopy and mass spectrometry", Journal of Physics D: Applied Physics **32**, 1876 (1999).

[40] L. Boufendi and A. Bouchoule, "Particle nucleation and growth in a low-pressure argon-silane discharge", Plasma Sources Science and Technology **3**, 262 (1994).

[41]F. Van de Wetering, R. Brooimans, S. Nijdam, J. Beckers, and G. Kroesen, "Fast and interrupted expansion in cyclic void growth in dusty plasma", Journal of Physics D: Applied Physics **48**, 035204 (2015).

[42]J. E. Allen, "Probe theory - the orbital motion approach", Physica Scripta **45**, 497 (1992).

[43]W. An, Z. Wang, A. Weisenburger, and G. Mueller, "Laser-induced fluorescence-dip spectroscopy of rydberg states of xenon for electric field measurement in plasma", Review of Scientific Instruments **93**, 023503 (2022).

[44]E. Barnat and G. Hebner, "Electric fields in a sheath near a metal–dielectric interface", Applied physics letters **85**, 3393–3395 (2004).

[45]D. J. Griffiths and D. F. Schroeter, *Introduction to quantum mechanics* (Cambridge university press, 2018).

[46]E. A. Riley, C. M. Hess, and P. J. Reid, "Photoluminescence intermittency from single quantum dots to organic molecules: emerging themes", International journal of molecular sciences **13**, 12487–12518 (2012).

[47]P. Y. Yu and M. Cardona, *Fundamentals of Semiconductors* (1999).

[48]R. Anderson, "Germanium-gallium arsenide heterojunctions", IBM Journal of Research and Development **4**, 283–287 (1960).

[49]L. Lappetito, "Quantum dots: a true "particle in a box" system", Physics Open Lab (2015).

[50]S. A. Empedocles and M. G. Bawendi, "Quantum-confined stark effect in single cdse nanocrystallite quantum dots", Science **278**, 2114–2117 (1997).

[51]A. L. Efros, J. B. Delehanty, A. L. Huston, I. L. Medintz, M. Barbic, and T. D. Harris, "Evaluating the potential of using quantum dots for monitoring electrical signals in neurons", Nature nanotechnology **13**, 278–288 (2018).

[52]Y. Varshni, "Temperature dependence of the energy gap in semiconductors", Physica **34**, 149–154 (1967).

[53]D. Valerini, A. Creti, M. Lomascolo, L. Manna, R. Cingolani, and M. Anni, "Temperature dependence of the photoluminescence properties of colloidal CdSe/ZnS core/shell quantum dots embedded in a polystyrene matrix", Physical Review B **71**, 235409 (2005).

[54]H. Fan, "Temperature dependence of the energy gap in monatomic semiconductors", Physical Review **78**, 808 (1950).

[55]H. Vasileff, "Electron self-energy and temperature-dependent effective masses in semiconductors: n-type Ge and Si", Physical Review **105**, 441 (1957).

[56]J. D. Jackson, *Classical electrodynamics*, 1999.

[57]B. Platier, T. Staps, P. Koelman, M. v. d. Schans, J. Beckers, and W. IJzerman, "Probing collisional plasmas with mcrs: opportunities and challenges", Applied Sciences **10**, 4331 (2020).

[58]R. Schmitt, *Electromagnetics explained: a handbook for wireless/rf, emc, and high-speed electronics* (Newnes, 2002).

[59]D. M. Pozar, *Microwave engineering* (John Wiley & sons, 2011).

[60]F. M. J. H. van de Wetering, J. Beckers, and G. M. W. Kroesen, "Anion dynamics in the first 10 milliseconds of an argon–acetylene radio-frequency plasma", Journal of Physics D: Applied Physics **45**, 485205 (2012).

[61]J. Gudmundsson, I. Kouznetsov, K. Patel, and M. Lieberman, "Electronegativity of low-pressure high-density oxygen discharges", Journal of Physics D: Applied Physics **34**, 1100 (2001).

[62]S. J. Smith and L. M. Branscomb, "Atomic negative-ion-photodetachment cross-section and affinity measurements", Journal of Research of the National Bureau of Standards **55**, 165 (1955).

[63]D. S. Burch, S. J. Smith, and L. M. Branscomb, "Photodetachment of O_2^-", Phys. Rev. **112**, 171–175 (1958).

[64]D. M. Neumark, K. R. Lykke, T. Andersen, and W. C. Lineberger, "Laser photodetachment measurement of the electron affinity of atomic oxygen", Phys. Rev. A **32**, 1890–1892 (1985).

[65]D. W. Arnold, C. Xu, E. H. Kim, and D. M. Neumark, "Study of low-lying electronic states of ozone by anion photoelectron spectroscopy of O_3^-", The Journal of chemical physics **101**, 912–922 (1994).

[66]K. M. Ervin, I. Anusiewicz, P. Skurski, J. Simons, and W. C. Lineberger, "The only stable state of O_2^- is the $X^2\Pi_g$ ground state and it (still!) has an adiabatic electron detachment energy of 0.45 eV", The Journal of Physical Chemistry A **107**, 8521–8529 (2003).

[67]H. Thomas, G. E. Morfill, V. Demmel, J. Goree, B. Feuerbacher, and D. Möhlmann, "Plasma crystal: coulomb crystallization in a dusty plasma", Phys. Rev. Lett. **73**, 652–655 (1994).

[68]D. Debarnot, T. Mérian, and F. Poncin-Epaillard, "Film chemistry control and growth kinetics of pulsed plasma-polymerized aniline", Plasma chemistry and plasma Processing **31**, 217–231 (2011).

[69] J. Beckers, B. van Minderhout, P. Blom, G. Kroesen, and T. Peijnenburg, "Particle contamination control by application of plasma", in Extreme ultraviolet (euv) lithography xi, Vol. 11323 (SPIE, 2020), pp. 558–563.

[70] M. van de Kerkhof, E. Galutschek, A. Yakunin, S. Cats, and C. Cloin, "Particulate and molecular contamination control in EUV-induced H_2-plasma in EUV lithographic scanner", in Systems contamination: prediction, control, and performance 2020, Vol. 11489 (SPIE, 2020), pp. 79–95.

[71] J. Beckers, T. van de Ven, R. van der Horst, D. Astakhov, and V. Banine, "EUV-induced plasma: a peculiar phenomenon of a modern lithographic technology", Applied Sciences **9**, 2827 (2019).

[72] D. N. Baker, "Satellite anomalies due to space storms", Space storms and space weather hazards, 285–311 (2001).

[73] X. Tian, R. K. Fu, J. Chen, P. K. Chu, and I. G. Brown, "Charging of dielectric substrate materials during plasma immersion ion implantation", Nuclear Instruments and Methods in Physics Research Section B: Beam Interactions with Materials and Atoms **187**, 485–491 (2002).

[74] M. van de Kerkhof, A. M. Yakunin, V. Kvon, S. Cats, L. Heijmans, M. Chaudhuri, and D. Asthakov, "Plasma-assisted discharges and charging in EUV-induced plasma", Journal of Micro/Nanopatterning, Materials, and Metrology **20**, 013801 (2021).

[75] P. Krainov, V. Ivanov, D. Astakhov, V. Medvedev, V. Kvon, A. Yakunin, and M. van de Kerkhof, "Dielectric particle lofting from dielectric substrate exposed to low-energy electron beam", Plasma Sources Science and Technology **29**, 085013 (2020).

[76] T. Van De Ven, P. Reefman, C. De Meijere, R. Van Der Horst, M. Van Kampen, V. Banine, and J. Beckers, "Ion energy distributions in highly transient EUV induced plasma in hydrogen", Journal of Applied Physics **123**, 063301 (2018).

[77] L. Heijmans and S. Nijdam, "Dust on a surface in a plasma: a charge simulation", Physics of Plasmas **23**, 043703 (2016).

[78] D. Kim and D. J. Economou, "Simulation of a two-dimensional sheath over a flat wall with an insulator/conductor interface exposed to a high density plasma", Journal of applied physics **94**, 2852–2857 (2003).

[79] J. Beckers, T. Ockenga, M. Wolter, W. Stoffels, J. Van Dijk, H. Kersten, and G. Kroesen, "Microparticles in a collisional rf plasma sheath under hypergravity conditions as probes for the electric field strength and the particle charge", Physical review letters **106**, 115002 (2011).

[80] E. Barnat and G. Hebner, "Electric field profiles around an electrical probe immersed in a plasma", Journal of applied physics **101**, 013306 (2007).

[81] G. Bacher, H. Schömig, J. Seufert, M. Rambach, A. Forchel, A. Maksimov, V. Kulakovskii, T. Passow, D. Hommel, C. Becker, et al., "Optical spectroscopy on non-magnetic and semimagnetic single quantum dots in external fields", physica status solidi (b) **229**, 415–422 (2002).

[82] E. Barnat and G. Hebner, "Radiofrequency sheath fields above a metal-dielectric interface", Journal of applied physics **96**, 4762–4770 (2004).

[83] A. V. Zakharov and E. V. Rosenfeld, "Charge density fluctuations on a dielectric surface exposed to plasma or uv radiation", Plasma **4**, 201–213 (2021).

[84] X. Wang, J. Colwell, M. Horanyi, and S. Robertson, "Charge of dust on surfaces in plasma", IEEE transactions on plasma science **35**, 271–279 (2007).

[85] Z. Marvi, T. Donders, M. Hasani, G. Klaassen, and J. Beckers, "Quantum dot photoluminescence as a versatile probe to visualize the interaction between plasma and nanoparticles on a surface", Applied Physics Letters **119**, 254104 (2021).

[86] M. Pustylnik, Z. Marvi, and J. Beckers, "On the optical measurement of microparticle charge using quantum dots", Journal of Physics D: Applied Physics **55**, 095202 (2021).

[87] M. Pustylnik, "Quantum dot on a plasma-facing microparticle surface: requirement on thermal contact for optical charge measurement", Contributions to Plasma Physics, e202200125 (2022).

[88] H. Qin, R. Meng, N. Wang, and X. Peng, "Photoluminescence intermittency and photo-bleaching of single colloidal quantum dot", Advanced Materials **29**, 1606923 (2017).

[89] L. A. Lane, A. M. Smith, T. Lian, and S. Nie, "Compact and blinking-suppressed quantum dots for single-particle tracking in live cells", The Journal of Physical Chemistry B **118**, 14140–14147 (2014).

[90] J. Casas Espiénola and X. Hernández Contreras, "Effect of dielectric constant on emission of cdse quantum dots", Journal of Materials Science: Materials in Electronics **28**, 7132–7138 (2017).

[91] S. M. Albahrani, T. Seoudi, D. Philippon, L. Lafarge, P. Reiss, H. Hajjaji, G. Guillot, M. Querry, J.-M. Bluet, and P. Vergne, "Quantum dots to probe temperature and pressure in highly confined liquids", RSC advances **8**, 22897–22908 (2018).

[92] G. W. Walker, V. C. Sundar, C. M. Rudzinski, A. W. Wun, M. G. Bawendi, and D. G. Nocera, "Quantum-dot optical temperature probes", Applied Physics Letters **83**, 3555–3557 (2003).

[93] A. Ekimov, A. L. Efros, T. Shubina, and A. Skvortsov, "Quantum-size stark effect in semiconductor microcrystals", Journal of Luminescence **46**, 97–100 (1990).

[94] J. Seufert, M. Obert, M. Scheibner, N. Gippius, G. Bacher, A. Forchel, T. Passow, K. Leonardi, and D. Hommel, "Stark effect and polarizability in a single CdSe/ZnSe quantum dot", Applied Physics Letters **79**, 1033–1035 (2001).

[95] K. Early, P. Sudeep, T. Emrick, and M. Barnes, "Polarization-driven stark shifts in quantum dot luminescence from single CdSe/oligo-PPV nanoparticles", Nano letters **10**, 1754–1758 (2010).

[96] T. Sheridan and A. Hayes, "Charge fluctuations for particles on a surface exposed to plasma", Applied physics letters **98**, 091501 (2011).

[97] N. Radić, B. Šantić, and V. Vujnović, "Floating potential and plasma sheath in vacuum arc plasma", Journal of applied physics **73**, 7174–7179 (1993).

[98] M. A. Lieberman, "Analytical solution for capacitive rf sheath", IEEE Transactions on Plasma Science **16**, 638–644 (1988).

[99] E. Stoffels, W. W. Stoffels, D. Vender, M. Haverlag, G. M. W. Kroesen, and F. J. de Hoog, "Negative ions in low pressure discharges", Contributions to Plasma Physics **35**, 331–357 (1995).

[100] R. N. Franklin, "Electronegative plasmas why are they so different?", Plasma Sources Science and Technology **11**, A31–A37 (2002).

[101] A. Agarwal, S. Rauf, and K. Collins, "Extraction of negative ions from pulsed electronegative capacitively coupled plasmas", Journal of Applied Physics **112**, 033303 (2012).

[102] T. Tsutsumi, A. Greb, A. R. Gibson, M. Hori, D. O'Connell, and T. Gans, "Investigation of the radially resolved oxygen dissociation degree and local mean electron energy in oxygen plasmas in contact with different surface materials", Journal of Applied Physics **121**, 143301 (2017).

[103] S. Taylor, J. F. Zhang, and W. Eccleston, "A review of the plasma oxidation of silicon and its applications", Semiconductor Science and Technology **8**, 1426–1433 (1993).

[104] G. S. Oehrlein, G. J. Scilla, and S.-J. Jeng, "Efficiency of oxygen plasma cleaning of reactive ion damaged silicon surfaces", Applied physics letters **52**, 907–909 (1988).

[105] E. Collart, J. Baggerman, and R. Visser, "On the role of atomic oxygen in the etching of organic polymers in a radio-frequency oxygen discharge", Journal of applied physics **78**, 47–54 (1995).

[106] J. K. Kim, S. I. Cho, N. G. Kim, M. S. Jhon, K. S. Min, C. K. Kim, and G. Y. Yeom, "Study on the etching characteristics of amorphous carbon layer in oxygen plasma with carbonyl sulfide", Journal of Vacuum Science & Technology A: Vacuum, Surfaces, and Films **31**, 021301 (2013).

[107] M. M. Hefny, D. Nečas, L. Zajıčková, and J. Benedikt, "The transport and surface reactivity of o atoms during the atmospheric plasma etching of hydrogenated amorphous carbon films", Plasma Sources Science and Technology **28**, 035010 (2019).

[108] A. Vesel, G. Primc, R. Zaplotnik, and M. Mozetič, "Applications of highly non-equilibrium low-pressure oxygen plasma for treatment of polymers and polymer composites on an industrial scale", Plasma Physics and Controlled Fusion **62**, 024008 (2020).

[109] E. Stoffels, W. W. Stoffels, and G. M. W. Kroesen, "Plasma chemistry and surface processes of negative ions", Plasma Sources Science and Technology **10**, 311–317 (2001).

[110] L. Schepers, J. Beckers, and W. IJzerman, "Determination of microparticle characteristics in an etching plasma", Contributions to Plasma Physics **58**, 985–994 (2018).

[111] I. B. Denysenko, K. Ostrikov, S. Xu, M. Y. Yu, and C. H. Diong, "Nanopowder management and control of plasma parameters in electronegative SiH_4 plasmas", Journal of Applied Physics **94**, 6097–6107 (2003).

[112] D. J. Economou, "Pulsed plasma etching for semiconductor manufacturing", Journal of Physics D: Applied Physics **47**, 303001 (2014).

[113] K. Tsumori and M. Wada, "Diagnostics tools and methods for negative ion source plasmas, a review", New Journal of Physics **19**, 045002 (2017).

[114] J. Bredin, P. Chabert, and A. Aanesland, "Langmuir probe analysis in electronegative plasmas", Physics of Plasmas **21**, 123502 (2014).

[115] J. P. J. Dubois, K. Achkasov, D. Kogut, A. Ahmad, J. M. Layet, A. Simonin, and G. Cartry, "Negative-ion surface production in hydrogen plasmas: determination of the negative-ion energy and angle distribution function using mass spectrometry", Journal of Applied Physics **119**, 193301 (2016).

[116] M. Bacal, "Photodetachment diagnostic techniques for measuring negative ion densities and temperatures in plasmas", Review of Scientific Instruments **71**, 3981–4006 (2000).

[117] R. Dodd, S. You, P. M. Bryant, and J. W. Bradley, "Negative ion density measurements in reactive magnetron sputtering", Plasma Processes and Polymers **6**, S615–S619 (2009).

[118] N. Oudini, N. Sirse, F. Taccogna, A. R. Ellingboe, and A. Bendib, "Photodetachment signal analysis to accurately determine electronegativity, electron temperature, and charged species density", Applied Physics Letters **109**, 124101 (2016).

[119] J. Conway, N. Sirse, S. K. Karkari, and M. M. Turner, "Using the resonance hairpin probe and pulsed photodetachment technique as a diagnostic for negative ions in oxygen plasma", Plasma Sources Science and Technology **19**, 065002 (2010).

[120] C. Küllig, K. Dittmann, and J. Meichsner, "A novel approach for negative ion analysis using 160 GHz microwave interferometry and laser photodetachment in oxygen cc-rf plasmas", Plasma Sources Science and Technology **19**, 065011 (2010).

[121] D. Vender, W. W. Stoffels, E. Stoffels, G. M. W. Kroesen, and F. J. de Hoog, "Charged-species profiles in electronegative radio-frequency plasmas", Phys. Rev. E **51**, 2436–2444 (1995).

[122] A. Kono, M. Haverlag, G. M. W. Kroesen, and F. J. de Hoog, "Temporal behavior of the electron and negative ion densities in a pulsed radio-frequency CF_4 plasma", Journal of Applied Physics **70**, 2939–2946 (1991).

[123] J. Meichsner, K. Dittmann, and C. Küllig, "Electron and negative ion analysis in oxygen capacitively coupled radio frequency plasma", Contributions to Plasma Physics **52**, 561–570 (2012).

[124] M. Osiac, T. Schwarz-Selinger, D. O. Connell, B. Heil, Z. L. Petrovic, M. M. Turner, T. Gans, and U. Czarnetzki, "Plasma boundary sheath in the afterglow of a pulsed inductively coupled RF plasma", Plasma Sources Science and Technology **16**, 355–363 (2007).

[125] C. Küllig, K. Dittmann, and J. Meichsner, "Detachment-induced electron production in the early afterglow of pulsed cc-rf oxygen plasmas", Physics of Plasmas **19**, 073517 (2012).

[126] T. Wegner, C. Küllig, and J. Meichsner, "On the EH transition in inductively coupled radio frequency oxygen plasmas: II. electronegativity and the impact on particle kinetics", Plasma Sources Science and Technology **26**, 025007 (2017).

[127] N. Oudini, F. Taccogna, A. Bendib, and A. Aanesland, "Numerical simulations used for a validity check on the laser induced photo-detachment diagnostic method in electronegative plasmas", Physics of Plasmas **21**, 063515 (2014).

[128] N. Sirse, S. K. Karkari, M. A. Mujawar, J. Conway, and M. M. Turner, "The temporal evolution in plasma potential during laser photo-detachment used to diagnose electronegative plasma", Plasma Sources Science and Technology **20**, 055003 (2011).

[129] A. Lichtenberg, V. Vahedi, M. Lieberman, and T. Rognlien, "Modeling electronegative plasma discharges", Journal of applied physics **75**, 2339–2347 (1994).

[130] S. Berezhnoj, C. Shin, U. Buddemeier, and I. Kaganovich, "Charged species profiles in oxygen plasma", Applied Physics Letters **77**, 800–802 (2000).

[131] D. Vender, W. Stoffels, E. Stoffels, G. Kroesen, and F. De Hoog, "Charged-species profiles in electronegative radio-frequency plasmas", Physical Review E **51**, 2436 (1995).

[132] S. Ashida and M. A. Lieberman, "Spatially averaged (global) model of time modulated high density chlorine plasmas", Japanese journal of applied physics **36**, 854 (1997).

[133] A. A. Mamun and P. K. Shukla, "Solitary potentials in cometary dusty plasmas", Geophysical Research Letters **29**, 17-1-17–4 (2002).

[134] J.-E. Wahlund, M. André, A. Eriksson, M. Lundberg, M. Morooka, M. Shafiq, T. Averkamp, D. Gurnett, G. Hospodarsky, W. Kurth, K. Jacobsen, A. Pedersen, W. Farrell, S. Ratynskaia, and N. Piskunov, "Detection of dusty plasma near the e-ring of saturn", Planetary and Space Science **57**, 1795–1806 (2009).

[135] V. Nosenko, S. K. Zhdanov, A. V. Ivlev, C. A. Knapek, and G. E. Morfill, "2D melting of plasma crystals: equilibrium and nonequilibrium regimes", Phys. Rev. Lett. **103**, 015001 (2009).

[136] S. Zhdanov, M. Schwabe, C. Räth, H. M. Thomas, and G. E. Morfill, "Wave turbulence observed in an auto-oscillating complex (dusty) plasma", Europhysics Letters **110**, 35001 (2015).

[137]M. Santos, P. L. Michael, E. C. Filipe, A. H. Chan, J. Hung, R. P. Tan, B. S. Lee, M. Huynh, C. Hawkins, A. Waterhouse, et al., "Plasma synthesis of carbon-based nanocarriers for linker-free immobilization of bioactive cargo", ACS Applied Nano Materials **1**, 580–594 (2018).

[138]M. van de Kerkhof, A. Yakunin, V. Kvon, F. van de Wetering, S. Cats, L. Heijmans, A. Nikipelov, A. Lassise, and V. Banine, "Understanding EUV-induced plasma and application to particle contamination control in EUV scanners", in Extreme ultraviolet (euv) lithography xi, Vol. 11323 (International Society for Optics and Photonics, 2020), 113230Y.

[139]E. Stoffels, W. Stoffels, G. Kroesen, and F. De Hoog, "Dust formation and charging in an Ar/SiH_4 radio-frequency discharge", Journal of Vacuum Science & Technology A: Vacuum, Surfaces, and Films **14**, 556–561 (1996).

[140]T. Donders, T. Staps, and J. Beckers, "Characterization of cyclic dust growth in a low-pressure, radio-frequency driven argon-hexamethyldisiloxane plasma", Journal of Physics D: Applied Physics **55**, 395203 (2022).

[141]J. Winter, J. Berndt, S. H. Hong, E. Kovačević, I. Stefanović, and O. Stepanović, "Dust formation in Ar/CH_4 and Ar/C_2H_2 plasmas", Plasma Sources Science and Technology **18**, 034010 (2009).

[142]L. Boufendi and A. Bouchoule, "Particle nucleation and growth in a low-pressure argon-silane discharge", Plasma Sources Science and Technology **3**, 262 (1994).

[143]M. Jiménez-Redondo, I. Tanarro, and V. J. Herrero, "Time evolution of neutral and charged species in Ar/C_2H_2 capacitively-coupled rf discharges", Plasma Sources Science and Technology **31**, 065003 (2022).

[144]J. Beckers, R. Gopalakrishnan, and J. Goree, "Editorial: particle interaction with afterglow plasma and non-quasi-neutral plasma", Frontiers in Physics **10** (2022).

[145]I. V. Schweigert and A. L. Alexandrov, "Effect of nanoparticles on an rf discharge afterglow", Journal of Physics D: Applied Physics **45**, 325201 (2012).

[146]B. van Minderhout, J. van Huijstee, R. Rompelberg, A. Post, A. Peijnenburg, P. Blom, and J. Beckers, "Charge of clustered microparticles measured in spatial plasma afterglows follows the smallest enclosing sphere model", Nature Communications **12**, 1–7 (2021).

[147]J. C. A. van Huijstee, P. Blom, A. T. A. Peijnenburg, and J. Beckers, "Spatio-temporal plasma afterglow induces additional neutral drag force on microparticles", Frontiers in Physics **10** (2022).

[148] L. Couëdel, A. Samarian, M. Mikikian, and L. Boufendi, "Dust density effect on complex plasma decay", Physics Letters A **372**, 5336–5339 (2008).

[149] A. Ivlev, M. Kretschmer, M. Zuzic, G. Morfill, H. Rothermel, H. Thomas, V. Fortov, V. Molotkov, A. Nefedov, A. Lipaev, et al., "Decharging of complex plasmas: first kinetic observations", Physical review letters **90**, 055003 (2003).

[150] L. Couëdel, M. Mikikian, L. Boufendi, and A. A. Samarian, "Residual dust charges in discharge afterglow", Physical Review E **74**, 026403 (2006).

[151] J. Berndt, E. Kovačević, V. Selenin, I. Stefanović, and J. Winter, "Anomalous behaviour of the electron density in a pulsed complex plasma", Plasma Sources Science and Technology **15**, 18 (2005).

[152] I. Stefanović, J. Berndt, D. Marić, V. Šamara, M. Radmilović-Radjenović, Z. L. Petrović, E. Kovačević, and J. Winter, "Secondary electron emission of carbonaceous dust particles", Physical Review E **74**, 026406 (2006).

[153] I. Denysenko, I. Stefanović, B. Sikimić, J. Winter, N. Azarenkov, and N. Sadeghi, "A global model for the afterglow of pure argon and of argon with negatively charged dust particles", Journal of Physics D: Applied Physics **44**, 205204 (2011).

[154] C. Larriba-Andaluz and S. L. Girshick, "Controlled fluxes of silicon nanoparticles to a substrate in pulsed radio-frequency argon–silane plasmas", Plasma Chemistry and Plasma Processing **37**, 43–58 (2017).

[155] M. Gueye, T. Gries, C. Noël, S. Migot-Choux, S. Bulou, E. Lecoq, P. Choquet, K. Kutasi, and T. Belmonte, "Interaction of (3-aminopropyl) triethoxysilane with pulsed ar–o2 afterglow: application to nanoparticles synthesis", Plasma Chemistry and Plasma Processing **36**, 1031–1050 (2016).

[156] M. van de Kerkhof, T. van Empel, M. Lercel, C. Smeets, F. van de Wetering, A. Nikipelov, C. Cloin, A. Yakunin, and V. Banine, "Advanced particle contamination control in EUV scanners", in Extreme ultraviolet (euv) lithography x, Vol. 10957, edited by K. A. Goldberg (International Society for Optics and Photonics, 2019), 109570U.

[157] I. Denysenko, E. von Wahl, S. Labidi, M. Mikikian, H. Kersten, T. Gibert, E. Kovačević, and N. Azarenkov, "Modeling of argon–acetylene dusty plasma", Plasma Physics and Controlled Fusion **61**, 014014 (2018).

[158] I. Denysenko, I. Stefanović, B. Sikimić, J. Winter, and N. Azarenkov, "Discharging of dust particles in the afterglow of plasma with large dust density", Physical Review E **88**, 023104 (2013).

[159]I. Denysenko, I. Stefanović, N. Azarenkov, and G. Burmaka, "Effect of secondary emission on the argon plasma afterglow with large dust density", Physics of Plasmas **22**, 023702 (2015).

[160]I. Filatova, F. Trukhachev, and N. Chubrik, "Study of the process of dust grain discharging in the afterglow of an rf discharge", Plasma physics reports **37**, 1042–1045 (2011).

[161]L. Wörner, A. Ivlev, L. Couëdel, P. Huber, M. Schwabe, T. Hagl, M. Mikikian, L. Boufendi, A. Skvortsov, A. Lipaev, et al., "The effect of a direct current field on the microparticle charge in the plasma afterglow", Physics of Plasmas **20**, 123702 (2013).

[162]M. Hasani, Z. Marvi, and J. Beckers, "Probing negative ions and electrons in the afterglow of a low-pressure oxygen radiofrequency plasma using laser-induced photodetachment", Journal of Physics D: Applied Physics **54**, 495202 (2021).

[163]T. R. Taylor, C. Xu, and D. M. Neumark, "Photoelectron spectra of the $C_{2n}H^-$ (n=1–4) and $C_{2n}D^-$ (n=1–3) anions", The Journal of Chemical Physics **108**, 10018–10026 (1998).

[164]D. R. Lide and W. M. Haynes, *Crc handbook of chemistry and physics*, Vol. 9 (CRC press Boca Raton, FL, 2010).

[165]M. Bacal, G. W. Hamilton, A. M. Bruneteau, H. J. Doucet, and J. Taillet, "Measurement of H^- density in plasma by photodetachment", Review of Scientific Instruments **50**, 719–721 (1979).

[166]W. Stoffels, M. Sorokin, and J. Remy, "Charge and charging of nanoparticles in a SiH_4 rf-plasma", Faraday Discussions **137**, 115–126 (2008).

[167]I. Denysenko, I. Stefanović, M. Mikikian, E. Kovacevic, and J. Berndt, "Argon/dust and pure argon pulsed plasmas explored using a spatially-averaged model", Journal of Physics D: Applied Physics **54**, 065202 (2020).

[168]E. Stoffels, W. W. Stoffels, D. Vender, M. Kando, G. M. W. Kroesen, and F. J. de Hoog, "Negative ions in a radio-frequency oxygen plasma", Phys. Rev. E **51**, 2425–2435 (1995).

[169]M. Haverlag, A. Kono, D. Passchier, G. Kroesen, W. Goedheer, and F. De Hoog, "Measurements of negative ion densities in 13.56-MHz rf plasmas of CF_4, C_2F_6, CHF_3, and C_3F_8 using microwave resonance and the photodetachment effect", Journal of applied physics **70**, 3472–3480 (1991).

[170]T. Best, R. Otto, S. Trippel, P. Hlavenka, A. von Zastrow, S. Eisenbach, S. Jézouin, R. Wester, E. Vigren, M. Hamberg, and W. D. Geppert, "Absolute photodetachment cross-section measurements for hydrocarbon chain anions", The Astrophysical Journal **742**, 63 (2011).

[171]N. Douguet, V. Kokoouline, and A. E. Orel, "Photodetachment cross sections of the $C_{2n}H^-$ ($n = 1-3$) hydrocarbon-chain anions", Phys. Rev. A **90**, 063410 (2014).

[172]A. Alexandrov, I. Schweigert, and D. Ariskin, "Kinetic simulations of argon dusty plasma afterglow including metastable atom kinetics", Journal of Experimental and Theoretical Physics **116**, 663–672 (2013).

[173]P. K. Shukla and A. Mamun, *Introduction to dusty plasma physics* (CRC press, 2015).

[174]I. Kaganovich, B. Ramamurthi, and D. J. Economou, "Spatiotemporal dynamics of charged species in the afterglow of plasmas containing negative ions", Physical Review E **64**, 036402 (2001).

[175]J. Berndt, E. Kovačević, I. Stefanović, and L. Boufendi, "Controlled dust formation in pulsed rf plasmas", Journal of Applied Physics **106**, 063309 (2009).

[176]M. Y. Pustylnik, Z. Marvi, and J. Beckers, "On the optical measurement of microparticle charge using quantum dots", Journal of Physics D: Applied Physics **55**, 095202 (2021).

[177]T. Donders, T. Staps, and J. Beckers, "Time-synchronized microwave cavity resonance spectroscopy and laser light extinction measurements as a diagnostic for dust particle size and dust density in a low-pressure radio-frequency driven nanodusty plasma", Applied Sciences **12**, 12013 (2022).

Acknowledgments

After four years of endeavours, in hindsight, I realize that accomplishment of my PhD project is also owed to the helping hands of my beloved colleagues and friends. In the end, I should acknowledge all the sincere help I was privileged to receive during my research.

The most prominent support was offered by my supervisor, **Job Beckers**. I express my deepest gratitude to you, Job, for believing in me to carry on such a tremendous task right after our first dialogue. There were many ebbs and flows during these four years, from the isolation incurred by COVID-related restrictions to the countless hindrances in the experiments. Despite all the challenges, your support remained unwavering, encouraging me to stay persistent and determined. Of all the lessons I learned from you through our collaborations, friendly gatherings, and informal talks, freedom in research and work was the most prominent. With this freedom in my research and your undivided support, I managed to lead my project and learn practical many valuable lessons by myself.

Next, I thank my closest colleague, **Zahra Marvi**, for all the contributions to the project and the numerous assistance on a friendly and personal level. I came to the Netherlands as an expatriate facing a flurry of challenges on a daily basis: from adaptation to a shockingly different culture to all the minute details to cope with my new life. Through all of these challenges, be they scientific or mundane, you always helped me to stand up and continue the work. There were many turning points throughout the project when you took on the supervisor role and made key decisions. When it comes to helping me as an expatriate, I must stress the part of another Iranian colleague: **Shahriar Mirpour**. You were the first person I approached to help me with relocation from Iran to The Netherlands. Also, during the first years, you provided valuable insights and information I needed to adapt to my new country. I also thank my officemates, who, from the very first day I entered the office, stood next to me on all the happy or challenging days: **Patrick Meijaard**, **Dmitry Shefer**, **Tim Staps**, **Boy van der Minderhout**, **Tim Donders**, **Judith van Huisthee**, **Siebe Dijks**, **Federico Medini**, and **Jovana Petkovic**. In all the lunch break walks and our friendly

gatherings, I learned many detailed and nuanced aspects of Dutch culture; thank you for being patient with me in this process. I appreciate **Ab Schrader**, **Pieter Sanders**, and **Jurgen Kohlhepp** for all the technical support for installation and working with the setups.

During my project, I had the pleasure and privilege of supervising one master's student. I appreciate my collaboration with **Guido Klaassen** as I supervised him on his master's project. Guido contributed substantially to the project by providing insights into the computational and experimental levels of the project. Also, we had numerous fruitful discussions about Dutch politics, culture, and history, as well as many other random and sometimes funny topics.

Upon the starting point of my PhD, I realized that I was exposed to numerous stresses and strains. I admit that I had my fair share of mental pressures throughout these four years. In this regard, I owe so much to my psychologist friends: **Sepideh Rajezi Esfahani** and **Anahita Mehrpour**; thank you for your support and for understanding my vulnerable and sensitive personality. My friends: **Masoud**, **Aref**, **Milad**, **Pouria**, **Elham**, and **Atieh**, I am proud and happy to be your friend. Thank you for all the good times we have had together, from traveling to watching movies and joyful parties.
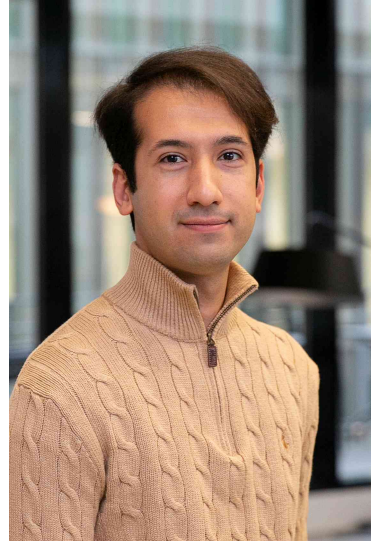
Last but not least, I am always grateful to my dearest mother, **Elaheh**, my only remaining family member. Ever since I lost my father at a young age, you stood as a pillar in my life; without you, my whole existence would fall. Thank you for standing shoulder-to-shoulder with me all these times.

Currriculum Vitae

Mohammad Hasani

July 29, 1993
Born in Tehran, Iran

2011-2015
Bachelor of Science: Atomic and molecular physics

Department of Physics, Iran University of Science and Technology, Tehran, Iran

2015-2018
Master of Science: Plasma physics

Department of Physics, Shahid Beheshti University, Tehran, Iran

- Master's thesis project at Laser and Plasma Research Institute. Subject: Plasma decontamination of persistent chemicals (endocrine disruptors).

2018-2023
Doctoral research in Elementary Processes in Gas Discharges research group. Subject: Towards plasma charging visualization.

Department of Applied Physics, Eindhoven University of Technology, Eindhoven, The Netherlands

Related publications

- Hasani, M., Donders, T.J.M., and Beckers, J. "Temporal afterglow of argon-acetylene plasma: measuring electron and negatively charged species densities." Journal of Physics D: Applied Physics (2023) (submitted)

- Hasani, M., Klaassen, G., Marvi, Z., Pustylnik, M. and Beckers, J. "Quantum dot photoluminescence as charge probe for plasma exposed surfaces." Journal of Physics D: Applied Physics, 56(2): p.025202 (2022).

- Marvi, Z., Donders, T.J.M., Hasani, M., Klaassen, G. and Beckers, J. "Quantum dot photoluminescence as a versatile probe to visualize the interaction between plasma and nanoparticles on a surface." Applied Physics Letters, 119(25), p.254104 (2021).

- Hasani, M., Z. Marvi, and J. Beckers. "Probing negative ions and electrons in the afterglow of a low-pressure oxygen radiofrequency plasma using laser-induced photodetachment." Journal of Physics D: Applied Physics 54.49: 495202 (2021).

Notable conference contributions

- Hasani. M, Marvi. Z, and Beckers. J. "Laser-induced photodetachment to probe negative ions in the afterglow of oxygen plasma." Oral presentation at Physics at Veldhoven, January 2021, Veldhoven, The Netherlands.

- Hasani. M, Klaassen. G, Pustylnik. M, Marvi. Z, and Beckers. J. "Probing Charge of plasma exposed surfaces with quantum dots photoluminescence." Oral presentation at The 48th EPS Conference on Plasma Physics, June 2022, Maastricht, The Netherlands.

- Hasani. M, Klaassen. G, Marvi. Z, and Beckers. J. "Quantum dots as charge probes for plasma exposed surfaces." Oral Presentation at The XXV Europhysics Conference on the Atomic and Molecular Physics of Ionized Gases, July 2022, Paris, France.